Fermilab FERMILAB-THESIS-1998-29

A Study of D^0 Production from 500 GeV π^-–Nucleon Interactions

by

Kevin M. Stenson

A dissertation submitted in partial fulfillment

of the requirements for the degree of

Doctor of Philosophy

(Physics)

at the

University of Wisconsin – Madison

1998

Abstract

Fermilab experiment E791 took data during six months in 1991 using a 500 GeV π^- beam on platinum and diamond targets for the purpose of studying the production and decay of particles containing a charm quark. In this dissertation, results are presented on the production of the D^0 and $\overline{D}^0$ mesons using fully reconstructed $D^0 \rightarrow K\pi$ and $D^0 \rightarrow K\pi\pi\pi$ decays. Specifically, the total forward production cross section is measured as well as differential cross sections as a function of the scaled longitudinal momentum, Feynman-x (x_F), and the transverse momentum squared (p_T^2).

The results are compared to theoretical predictions from a next-to-leading order (NLO) calculation and from a leading order Monte Carlo event generator, PYTHIA/JETSET, which uses parton showers to account for higher-order terms. The comparison is made to both the c quark predictions and the predictions for D mesons using the Peterson fragmentation scheme for the NLO calculation and the Lund string fragmentation for the PYTHIA/JETSET prediction. The data are also compared to previous measurements by other experiments which used a π^- beam.

Assuming an A^1 dependence, the total forward cross section for the sum of D^0 and $\overline{D}^0$ production is measured to be $\sigma(D^0/\overline{D}^0\ ; x_F > 0) = 15.4\ ^{+1.8}_{-2.3}$ μbarns/nucleon, in good agreement with other experiments and the NLO prediction. The differential cross sections agree best with the NLO c quark prediction and the PYTHIA/JETSET D^0 meson prediction. Several functions are fit to the differential cross sections. From the fits to the x_F distribution we find the x_F distribution peaks at $x_F = 0.013 \pm 0.004$, significantly above zero as predicted by the harder pion parton distribution function. Fitting the shape of the x_F distribution to $(1 - x_F)^n$, while not a good fit, gives $n = 4.61 \pm 0.19$ for the range $0.05 < x_F < 0.50$. The p_T^2 shape is acceptably fit with the function $e^{-b' p_T}$ with $b' = 2.41 \pm 0.03$ over the range 1 (GeV/c)$^2 < p_T^2 <$ 18 (GeV/c)^2.

Acknowledgments

I have come to realize that this Ph.D. dissertation is the result of a lot of work on my part. However, none of this work would be possible without the help I have received from numerous sources.

First, of course, is the E791 Collaboration, without whom the data would not be available. They are a good bunch of people to work with and are very adept at keeping one on one's toes. All credit for the quality of this data clearly belong with them; reserving, of course, any blame for me.

I would also like to thank the FOCUS Collaboration. While the data in this dissertation comes from TPL, I have spent much more of my time at "Wildband." It was with the FOCUS group that I got a chance to experience the excitement of putting together and running a high energy physics experiment. In particular, thanks go to Will Johns for his help and his confidence in me (hopefully not misplaced). I also appreciate the friendships developed during all those long shifts with Harry Cheung, Yeon Sei Chung, Irish, Will Johns, Jon Link, Matt Nehring, and Eric Vaandering.

My advisor, Marleigh Sheaff, deserves many thanks for her help. I would not have had such a broad education, in high energy and beyond, were it not for her. Not only did she extend my education, usually by finding more work for me, but she always maintained interest in what I was doing. The trips to Mexico were also appreciated.

During Marleigh's many unavoidable absences, I was very competently looked after by Jeff Appel and Jean Slaughter, my Fermilab advisors. They were my number one resource for information about the E791 experiment. In addition, they were always eager to check out any new result I might have and helped to keep me interested in the field. Thank you both.

I also thank my other advisor, Francis Halzen, for being my advisor.

I would also like to thank the people who, although not required to, gladly proofread my dissertation. These brave souls are Jeff Appel, Harry Cheung, Austin Napier, and Jean Slaughter.

Thanks also to the people who readily acquiesced to being on my committee, Francis Halzen, Marleigh Sheaff, Lee Pondrom, Don Reeder, Martin Olssen, and Deborah Joseph.

During my graduate school career, my funding has come from a variety of sources. I wish to thank Paul Sheldon, Med Webster, and John Cumalat who arranged to keep me paid by the National Science Foundation, and to my parents, Gary and Rita Stenson, who willingly filled the monetary gaps, giving me some peace of mind.

While my parents always readily supplied the funds to keep my education going, that is only the tip of the iceberg. Their help is really beyond measure. Without their continuing encouragement and love over the last 28 years this dissertation would not be possible. They have my eternal gratitude for the support they have given me and the faith they have had in me.

I wish to thank my grandparents, Elmer and Elsie Stenson, who continue to love me even though I never write. Thanks also to my late grandmother, Florence Elefson, who once told me, “Study hard.”

Contents

Abstract i

Acknowledgements iii

List of Tables vii

List of Figures xiii

1 Introduction and Theory **1**

1.1 Standard Model 1

1.2 Charm Hadroproduction 3

1.2.1 Charm Quark Production 4

1.2.2 Hadronization 6

1.3 Comparing Theory and Data 10

2 The E791 Experiment **13**

2.1 Overview of Fixed-Target Charm Detection 13

2.2 Generating the Beam 16

2.3 The Spectrometer 17

2.3.1 Beam Tracking 18

2.3.2 The Target 19

2.3.3 Downstream Tracking 21

2.3.3.1 Vertex Silicon 21

2.3.3.2 Drift Chambers 21
2.3.3.3 Magnets 24
2.3.4 Čerenkov Counters 25
2.3.5 Calorimeters 26
2.3.6 Muon Detectors 26
2.4 Trigger and Data Acquisition 27
2.5 Scalers 29
2.6 The Monte Carlo 30

3 Event Reconstruction and Selection 33

3.1 Filter and Reconstruction 34
3.1.1 Event Reconstruction 34
3.1.1.1 Track Reconstruction 34
3.1.1.2 Vertex Reconstruction 36
3.1.1.3 Particle Identification Reconstruction 36
3.1.2 Filtering 36
3.1.3 Release 5 and Release 7 Comparison 38
3.2 Stripping, Substripping and Microstripping 41
3.3 The Final Sample 42
3.3.1 Determining selection criteria 42
3.3.2 Final cuts 45

4 Data 59

4.1 Calculating Yields 59
4.2 Using Normalized Mass 61
4.3 Final Data Mass Plots 73

5 Acceptance **83**

5.1 Experiment Livetime 84

5.2 Trigger Efficiency 84

5.3 Reconstruction Efficiency 88

5.3.1 First Order Reconstruction Efficiency Calculation 88

5.3.2 Weighting the Monte Carlo 90

5.3.3 Factoring in Time Dependence 95

5.3.4 Applying the Reconstruction Efficiency 100

6 Results and Systematic Errors **101**

6.1 Cross Section Definition and Calculation 101

6.2 Systematic Errors 104

6.2.1 Systematic Errors Affecting Only the Normalization 104

6.2.2 Systematic Errors for $N_{rec}(D^0 \to Kn\pi)$ 105

6.2.3 Systematic Errors for ϵ_{rec} 105

6.2.3.1 Monte Carlo Production 106

6.2.3.2 Monte Carlo Weighting 106

6.2.3.3 Tracking and Vertexing Efficiency 108

6.3 Results and Comparisons 111

6.3.1 Combining the Errors 111

6.3.2 D^0 x_F and p_T^2 Differential Cross Sections 119

6.3.3 D^0 Total Cross Section 150

7 Conclusions **157**

Bibliography 159

List of Tables

2.1 E791 targets 20

2.2 E791 silicon microstrip vertex detector 22

2.3 E791 drift chamber information 23

3.1 Stages of event reconstruction and reduction. 33

3.2 Final cuts for $K\pi$ candidates 52

3.3 Final cuts for Seed 4 $K\pi\pi\pi$ candidates 53

3.4 Final cuts for Seed 3 $K\pi\pi\pi$ candidates 54

3.5 Release 5 and Release 7 $K\pi$ and $K\pi\pi\pi$ yields from different data samples. 56

4.1 $K\pi$ measured mass and width in bins of x_F for Release 5 and Release 7 data. 62

4.2 $K\pi\pi\pi$ measured mass and width in bins of x_F for Release 5 and Release 7 data. 63

4.3 $K\pi$ measured mass and width in bins of x_F for Release 5 and Release 7 Monte Carlo data. 64

4.4 $K\pi\pi\pi$ measured mass and width in bins of x_F for Release 5 and Release 7 Monte Carlo data. 65

5.1 Trigger efficiency 87

5.2 Percentage of data for each of the five run periods divided by release . 100

6.1 Comparison of PYTHIA/JETSET parameters for MC1 and MC2 107

6.2 Comparison of background-subtracted data to MC1 and MC2 for various variables 107

6.3 x_F differential cross section for D^0 mesons 122

6.4 p_T^2 differential cross section for D^0 mesons 123

6.5 Results of fitting various MNR NLO c quark distributions to the data 127

6.6 Results of fitting various PYTHIA/JETSET c quark distributions to the data 128

6.7 Results of fitting various MNR NLO D meson distributions to the data 132

6.8 Results of fitting various PYTHIA/JETSET D^0 distributions to the data 133

6.9 Effect of changing x_F lower and upper limits on the parameters of Eq. 6.17 137

6.10 Shape parameter results from fits to various MNR NLO c quark x_F distributions 139

6.11 Shape parameter results from fits to various PYTHIA/JETSET c quark x_F distributions 140

6.12 Shape parameter results from fits to various MNR NLO D meson x_F distributions 141

6.13 Shape parameter results from fits to various PYTHIA/JETSET D^0 x_F distributions 142

6.14 Shape parameter results from fits to various MNR NLO c quark p_T^2 distributions 145

6.15 Shape parameter results from fits to various PYTHIA/JETSET c quark p_T^2 distributions 146

6.16 Shape parameter results from fits to various MNR NLO D meson p_T^2 distributions 147

6.17 Shape parameter results from fits to various PYTHIA/JETSET D^0 p_T^2 distributions 148

6.18 Comparison of x_F and p_T^2 shape parameters to previous experiments . 150

6.19 Summary of the error on the total forward D^0 cross section measurement 154

6.20 Results for the MNR NLO $D^0/\overline{D}^0$ total forward cross section 155

List of Figures

1.1 Plots of parton distribution functions for protons and pions 5

1.2 Leading order hadronic charm pair production Feynman diagrams . . 7

1.3 Some of the next-to-leading order hadronic charm pair production Feynman diagrams 7

2.1 The E791 spectrometer. 18

2.2 E791 acceptance functions vs. x_F and p_T^2. 25

3.1 $K\pi$ mass and width versus x_F for data and Monte Carlo events reconstructed with Release 5 and Release 7 39

3.2 Ratio of Release 7 acceptance to Release 5 acceptance as a function of x_F and p_T^2 for $K\pi$ and $K\pi\pi\pi$ 40

3.3 Comparison and optimization of $K\pi$ cut variables using Monte Carlo and data 49

3.4 Comparison and optimization of Seed 4 $K\pi\pi\pi$ cut variables using Monte Carlo and data 50

3.5 Comparison and optimization of Seed 3 $K\pi\pi\pi$ cut variables using Monte Carlo and data 51

3.6 Monte Carlo $K\pi$ and $K\pi\pi\pi$ invariant mass plots with the correct (solid line) and incorrect (dotted line) sign of the K 52

3.7 Sample B $K\pi$ and $K\pi\pi\pi$ yields from the Release 5 E791 data 56

3.8 Sample B $K\pi$ and $K\pi\pi\pi$ yields from the Release 7 E791 data 57

4.1 Sample A $K\pi$ invariant mass plots for 20 bins of x_F from the Release 5 E791 data 68

4.2 Sample A $K\pi$ invariant mass plots for 20 bins of x_F from the Release 7 E791 data 69

4.3 Sample A $K\pi$ normalized mass plots for 20 bins of x_F from the Release 5 E791 data. 70

4.4 Sample A $K\pi$ normalized mass plots for 20 bins of x_F from the Release 7 E791 data. 71

4.5 Ratio of yields obtained from the normalized mass distribution to yields obtained from the invariant mass distribution for data and Monte Carlo versus x_F 72

4.6 Sample B $K\pi$ mass plots for 20 bins of x_F from the Release 5 E791 data 74

4.7 Sample B $K\pi$ mass plots for 20 bins of x_F from the Release 7 E791 data 75

4.8 Sample B $K\pi\pi\pi$ mass plots for 20 bins of x_F from the Release 5 E791 data 76

4.9 Sample B $K\pi\pi\pi$ mass plots for 20 bins of x_F from the Release 7 E791 data 77

4.10 Sample B $K\pi$ mass plots for 20 bins of p_T^2 from the Release 5 E791 data 78

4.11 Sample B $K\pi$ mass plots for 20 bins of p_T^2 from the Release 7 E791 data 79

4.12 Sample B $K\pi\pi\pi$ mass plots for 20 bins of p_T^2 from the Release 5 E791 data 80

4.13 Sample B $K\pi\pi\pi$ mass plots for 20 bins of p_T^2 from the Release 7 E791 data 81

5.1 Effect of Monte Carlo weighting on $K\pi$ x_F and p_T^2 distributions 92

5.2 Effect of Monte Carlo weighting on x_F and p_T^2 acceptance 94

5.3 Ratio of data to Monte Carlo weighted to the average as a function of x_F (p_T^2) in bins of p_T^2 (x_F). 96

5.4 Ratio of data to Monte Carlo weighted to account for correlations as a function of x_F (p_T^2) in bins of p_T^2 (x_F). 97

5.5 $K\pi$ and $K\pi\pi\pi$ reconstruction efficiency versus x_F and p_T^2 for the five run periods 99

6.1 $K\pi\pi\pi$ to $K\pi$ measured branching ratio vs. x_F compared to the PDG value 109

6.2 $K\pi\pi\pi$ to $K\pi$ measured branching ratio vs. p_T^2 compared to the PDG value 110

6.3 $K\pi$ fully corrected x_F differential cross section 114

6.4 $K\pi\pi\pi$ fully corrected x_F differential cross section 115

6.5 $K\pi$ fully corrected p_T^2 differential cross section 116

6.6 $K\pi\pi\pi$ fully corrected p_T^2 differential cross section 117

6.7 D^0 fully corrected x_F differential cross section 120

6.8 D^0 fully corrected p_T^2 differential cross section 121

6.9 Plots of gluon distribution functions for protons and pions from various PDF sets 125

6.10 Comparison of the D^0 x_F distribution to c quark theory predictions . . 130

6.11 Comparison of the D^0 p_T^2 distribution to c quark theory predictions . . 131

6.12 Comparison of the D^0 x_F distribution to D meson theory predictions . 134

6.13 Comparison of the D^0 p_T^2 distribution to D meson theory predictions . 135

6.14 Fits to the D^0 fully corrected x_F differential cross section 138

6.15 Fits to the D^0 fully corrected p_T^2 differential cross section 144

6.16 D^0 fully corrected x_F differential cross sections from E791 and WA92 . 151

6.17 D^0 fully corrected p_T^2 differential cross sections from E791 and WA92 . 152

6.18 Theoretical and experimental results for the $c\overline{c}$ cross section versus energy 156

Chapter 1

Introduction and Theory

1.1 Standard Model

The Standard Model provides the current description of almost everything that is known about particle physics. It tells us what particles and force mediators are present and how they interact. The Standard Model is simply a marriage between the Quantum Chromodynamics (QCD) theory of the strong interaction and the electroweak theory of the electromagnetic and weak interactions. The force carrier for the strong, or color, force is the gluon. The photon mediates the electromagnetic force while the $W^{\pm}$ and Z^0 mediate the weak force. In addition to the force carriers, the Standard Model contains three generations of matter. The quark doublets (up(u)–down(d), charm(c)–strange(s) and top(t)–bottom(b)) are matched by the lepton doublets (electron(e)–electron neutrino(ν_e), muon(μ)–muon neutrino(ν_μ) and tau(τ)–tau neutrino(ν_τ). Each of these particles also has a corresponding antiparticle (e.g. the anti-up quark, $\overline{u}$). A quark can combine with an antiquark to form a meson or with two other quarks to form a baryon, both of which are called hadrons. In fact, the color force which acts on objects with color (quarks and gluons) only allows quarks to

exist inside color neutral hadrons. Neutrons (n) and protons (p) are the most common baryons and are generically labeled nucleons (N). The proton has two up and one down valence quarks while the neutron has one up and two down valence quarks. All ordinary matter is made up of atoms which are combinations of protons, neutrons and electrons. The mesons mentioned in this dissertation are pions (π) and kaons (K) which are both pseudoscalar (spin 0) mesons. The pion is the lightest meson and is composed of up and down valence quarks (antiquarks). The kaon is the lightest strange meson and contains a strange valence quark (antiquark) in addition to an up or down valence antiquark (quark).

Although QCD is a well-defined theory, obtaining solutions to most problems is quite difficult. Therefore, additional experimental information is used to augment the theory. Much of this experimental evidence comes from deep inelastic scattering (DIS) experiments. In DIS experiments, a lepton, usually an electron, is used to probe nucleons at different values of Q^2 (the square of the momentum transfer and a measure of the energy scale). The scattering results indicate that nucleons are made up of free point-like *partons*. Combining these results with the observation that we never find free quarks or gluons, we are led to the main premises of the parton model. The parton model actually predates QCD but still provides a good intuitive understanding of hadronic interactions. The parton model starts by assuming that hadrons are made up of partons (now known to be quarks and gluons). Each parton carries a fraction x of the momentum of the hadron and has no transverse momentum with respect to the hadron. Two other ingredients of the parton model are *asymptotic freedom* and *confinement*. Asymptotic freedom is the statement that at very large Q^2 ($Q^2 =$ the square of the momentum transfer in the interaction) the partons are free inside the hadron. Confinement requires that quarks and gluons must be locked up inside of

color-neutral hadrons. QCD also explains these effects by means of a running coupling constant, α_s, which increases as the distance (energy scale) increases (decreases). In particular, at leading order, the value of α_s, which determines the strength of the interaction, is given by:

$$\alpha_s(Q^2) = \frac{12\,\pi}{(33-2n_f)\,\ln(Q^2/\Lambda^2_{QCD})} \tag{1.1}$$

$$\alpha_s(r) = \frac{6\,\pi}{(33-2n_f)\,\ln(1/\Lambda_{QCD}\,r)} \tag{1.2}$$

where n_f is the number of quark flavors and Λ_{QCD} is a scale parameter which seems to lie between 0.1 GeV and 0.5 GeV. From Eq. 1.1 we see that α_s is small when $Q^2 \gg \Lambda_{QCD}$. In this case, a perturbative expansion in powers of α_s can be expected to give reliable results with only a few terms. At energy scales $\lesssim \Lambda_{QCD}$, perturbative QCD breaks down and other methods, such as lattice gauge theory, must be employed. Equation 1.2 is the Fourier transform of Eq. 1.1 and demonstrates that as $r \to 1/\Lambda_{QCD}$, $\alpha_s \to \infty$. This provides the confinement mechanism in QCD. Some aspects of the parton model including the Q^2 evolution and the intrinsic transverse momentum of the partons is modified by our understanding of QCD. Therefore, a more general parton model, the *QCD improved* parton model is sometimes distinguished from the naïve parton model.

1.2 Charm Hadroproduction

We can now apply the QCD improved parton model to charm particle hadroproduction. For a specific example we take the E791 experiment (cf Chapter 2) where a beam of 500 GeV/c π^- mesons impinged upon a nuclear target. The production of charm mesons and baryons from the π^-–nucleon interaction can be usefully divided into three parts. First, we need to know which partons are involved in the production.

The second part is the production of a charm quark – anticharm quark ($c\overline{c}$) pair from an interaction involving the aforementioned partons. The last part of the interaction is understanding how the $c\overline{c}$ pair converts into hadrons.

1.2.1 Charm Quark Production

The E791 single inclusive charm quark production mechanism from a pion-nucleon interaction can be schematically represented by

$$H_\pi(\mathbf{P}_\pi) \; + \; H_N(\mathbf{P}_N) \;\; \longrightarrow \;\; Q_c(\mathbf{p}_c) \; + \; X \tag{1.3}$$

where H is a hadron and Q_c is a charm quark. The perturbative QCD $c\overline{c}$ production cross section (cf Section 6.1) for this process can be written as

$$d\sigma \;\; = \;\; \sum_{i,j} \int dx_\pi \, dx_N \, f_i^\pi(x_\pi, \mu_F^2) \, f_j^N(x_N, \mu_F^2) \, d\hat{\sigma}_{ij}(x_\pi \mathbf{P}_\pi, x_N \mathbf{P}_N, \mathbf{p}_c, m_c, \mu_R^2) \tag{1.4}$$

where

$\mathbf{P}_\pi$ ($\mathbf{P}_N$) $\equiv$ pion (nucleon) momentum in the hadronic center of mass,

x_π (x_N) $\equiv$ fraction of P_π (P_N) carried by the interacting parton from the pion (nucleon),

f_k^π (f_k^N) $\equiv$ parton distribution function for the pion (nucleon),

μ_R (μ_F) $\equiv$ renormalization (factorization) scale, and

$d\hat{\sigma}_{ij}(x_\pi \mathbf{P}_\pi, x_N \mathbf{P}_N, \mathbf{p}_c, m_c, \mu_R^2)$ $\equiv$ cross section for the two interacting partons to produce a charm quark with mass m_c and momentum $\mathbf{p}_c$.

A parton distribution function (PDF) describes the parton composition of a hadron as a function of the fractional momentum of the parton. That is, $f_k^A(x_A, \mu_F^2)$ gives the probability of finding a k-type parton with fractional momentum x_A in an A-type hadron. While in the naïve parton model the PDF's are independent of energy scale, the results from QCD clearly indicate a dependence on Q^2. The Heisenberg

uncertainty principle allows particles (in this case gluons and $q\overline{q}$ pairs) to pop in and out of existence as long as their stay is short enough ($\Delta t < \hbar/\Delta E$). As Q^2 increases, the distance and time scale decreases and so more of the virtual particles are "seen," thus changing the parton distribution functions. The scale at which the PDF's are evaluated is the *factorization scale*, μ_F. We avoid measuring the PDF's at every energy scale by using the *Altarelli-Parisi* equations which allow us to measure the PDF's at one scale and evolve them to another scale. Examples of PDF's are shown in Fig. 1.1. Summing (integrating) over all parton types (momentum fractions) is explicitly shown in Eq. 1.4. One basic assumption in this formulation is that the partons have no transverse momenta relative to the hadron. Fermi motion and virtual emissions and absorptions should give the partons some transverse motion. This is sometimes added in calculations by giving the partons some *intrinsic* k_t according to a Gaussian distribution with a width of a few hundred MeV/c.

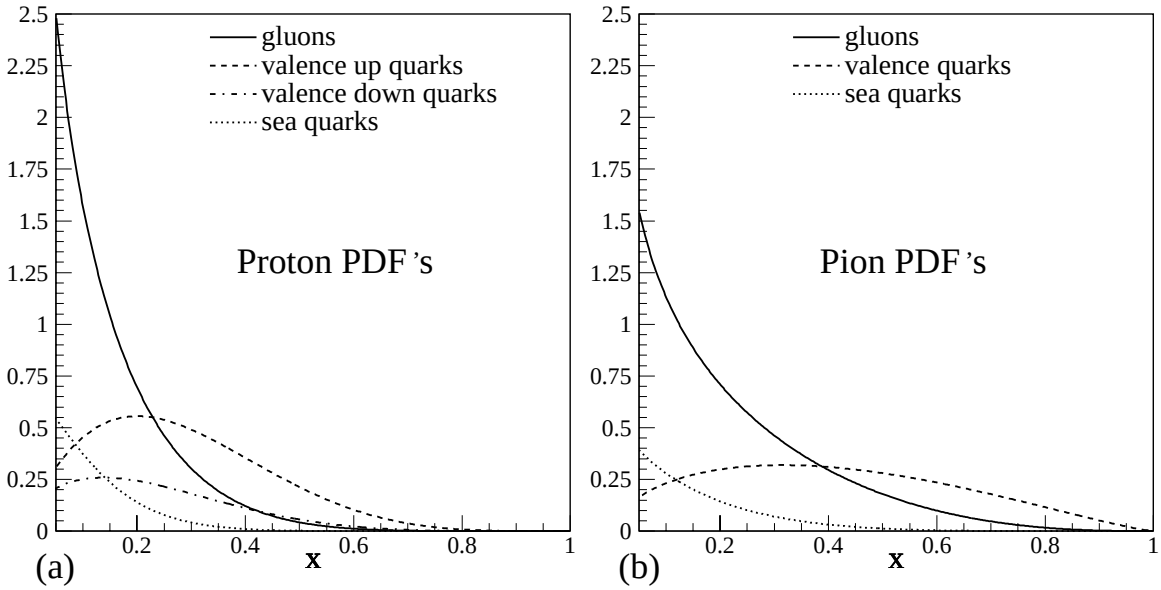

Fig. 1.1.— Plots of parton distribution functions at Q^2=5 (GeV/c)^2 in the range $0.05<x<1.0$ for protons (a) and pions (b). The proton PDF is HMRSB [1] and the pion PDF is SMRS2 [2]. The PDF data are obtained from the CERN program PDFLIB [3].

For each parton type and momentum there is a charm production cross section, $d\hat{\sigma}_{ij}(x_\pi \mathbf{P}_\pi, x_N \mathbf{P}_N, \mathbf{p}_c, m_c, \mu_R^2)$. In addition to the initial and final momenta, the cross section depends on the *renormalization scale*, μ_R, which is the scale at which α_s is evaluated. Producing a $c\overline{c}$ pair from two partons takes place at an energy scale on the order of the charm quark mass ($m_c \approx 1.5 \pm 0.3$ GeV/c^2). Since $\Lambda_{QCD} \lesssim 0.5$ GeV, we expect that charm quark production will be calculable in perturbative QCD but perhaps not too reliably since 1.5 GeV $\not\gg$ 0.5 GeV. The first contributions to the production cross section are the leading order (LO) terms. The Feynman diagrams which contribute to the leading order calculation are shown in Fig. 1.2. The existence of exactly two vertices makes them α_s^2 terms. The top diagram produces a $c\overline{c}$ pair from quark-antiquark annihilation while the bottom diagrams take place via gluon-gluon fusion and account for ~80% of the leading order cross section for the E791 conditions. The full next-to-leading order (NLO) calculation has been performed by Mangano, Nason and Ridolfi (MNR) [4]. A few examples of the NLO diagrams are shown in Fig. 1.3. The NLO diagrams come from three sources. The first source is single gluon emission ($q\overline{q} \to c\overline{c}g$ and $gg \to c\overline{c}g$) which is of order α_s^3. The second source is virtual gluon emission and absorption reabsorption ($q\overline{q} \to c\overline{c}$ and $gg \to c\overline{c}$) which is of order α_s^4 but interferes with the α_s^2 diagrams to give an α_s^3 contribution. The last source of NLO processes is quark-gluon fusion, $gq \to c\overline{c}q$ and $g\overline{q} \to c\overline{c}\overline{q}$, which is of order α_s^3.

1.2.2 Hadronization

The last phase of charm hadroproduction produces the observed charm particles (hadrons) from the charm quarks. This process is termed *hadronization* or *fragmentation*. This process occurs at a scale of the same order as Λ_{QCD} and is therefore not

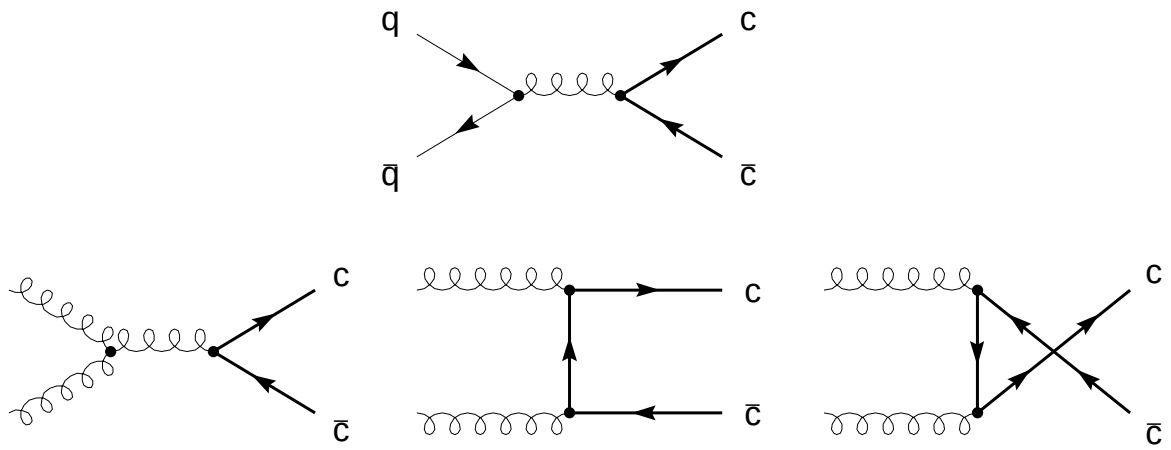

Fig. 1.2.— Leading order Feynman diagrams for hadronic charm pair production. The top diagram is quark-antiquark annihilation and the bottom diagrams are from gluon-gluon fusion.

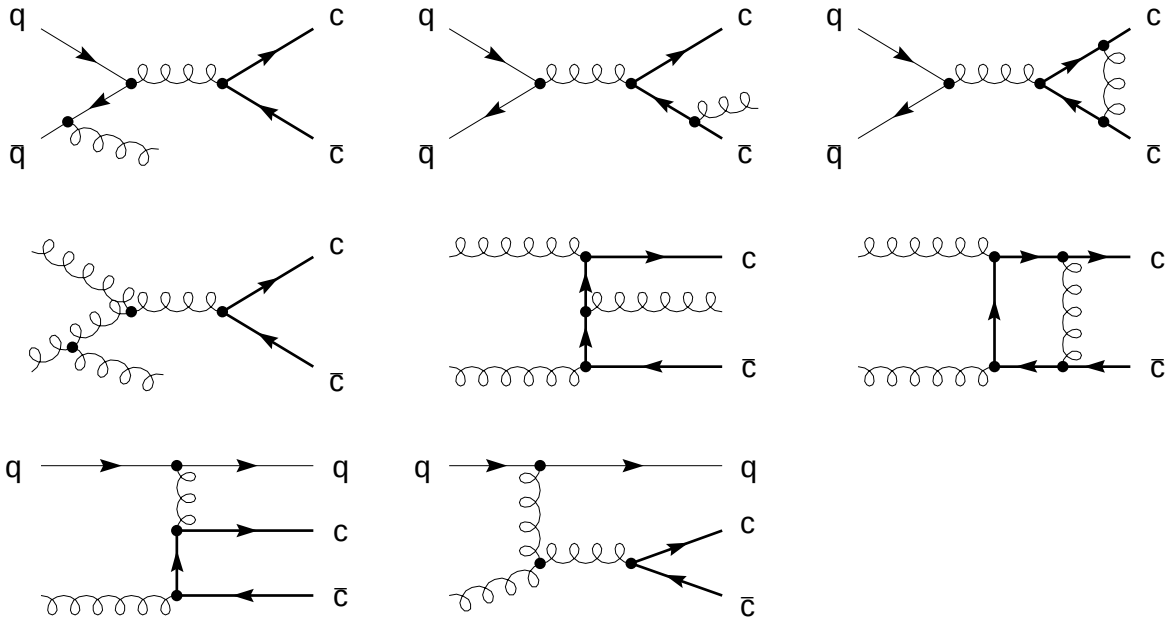

Fig. 1.3.— Some of the next-to-leading order Feynman diagrams for hadronic charm pair production. The top diagram is quark-antiquark annihilation, the middle diagrams are from gluon-gluon fusion and the bottom diagrams come from quark-gluon fusion.

calculable by perturbative QCD. In fact, hadronization is one of the least well understood aspects of QCD, especially in the hadronic environment. Since the hadronization process takes place at a much lower energy scale than the charm quark production, the two processes also take place at two different time scales. Therefore, the two processes should not affect each other and it should be possible to calculate the two processes separately. This is the principle of *factorization*.

The basic picture of hadronization starts with visualizing a color flux tube (or string) connecting the charm quark to the anticharm quark or to remnants of the interaction. The color flux tube has a spring constant which is $\kappa \sim 1$ GeV/fm $\sim$ 0.2 GeV^2. As the flux tube stretches (from the charm quark motion) the potential energy in the string increases until there is enough energy to create a $q\overline{q}$ pair from the vacuum. This quark "popping" continues until the energy in the string is too small to produce any more $q\overline{q}$ pairs. Then, the charm quark can combine with the antiquark nearest it in phase space to form a meson. There are two common methods for modeling the heavy quark fragmentation process, both of which involve fragmentation functions.

The first method only involves the produced charm particle, ignoring the rest of the event. In this picture, the charm quark gives up some of its energy in order to pop a $q\overline{q}$ pair and then combines with the antiquark to form a meson. The most popular heavy quark fragmentation function used in this model is the Peterson formula [5]:

$$f(z) \;\propto\; \frac{1}{z\left(1 - \frac{1}{z} - \frac{\epsilon_Q}{1-z}\right)^2} \tag{1.5}$$

where ϵ_Q is a free parameter scaling approximately as $1/m_Q^2$ where m_Q is the heavy quark mass. The fragmentation function $f(z)$ gives the probability that a meson will be formed with a fraction z $(0 < z < 1)$ of the original quark momentum. Actually,

there are several possible definitions of z including the fractional energy, longitudinal momentum, and energy plus longitudinal momentum. It is clear from this model that the charm hadron must have lower momentum than the charm quark. This model, with the Peterson fragmentation function, describes the data on the production of hadrons from e^+e^- collisions quite well where there are no hadrons except those formed during the hadronization.

In the hadroproduction environment the above method is found to be too simple to explain the observed data. In e^+e^- collisions, the c and $\overline{c}$ are color attached to each other with equal and opposite momenta. This is identical to the picture in which the c (or $\overline{c}$) quark is moving away from a fixed interaction point which is the basis for the Peterson fragmentation described above. In hadroproduction collisions, the charm quarks are attached to the remnant beam or target particles by the color force. Therefore, the momenta of these remnant particles can affect the momenta of the hadrons. This is supported by evidence for the leading-particle effect [6] which finds that charm mesons with a valence quark in common with a valence beam quark are more likely to be produced at high momentum than other charm mesons. In order to include these types of effects, a model of the entire fragmentation process is required. One model of this type is string fragmentation, implemented by the Lund group in the computer program PYTHIA/JETSET [7]. Although the Peterson function could also be used in this model, the "Lund symmetric fragmentation function"

$$f_{\mathrm{Lund}}(z) \;\propto\; \frac{(1\,-\,z)^a}{z}\,\exp\left(\frac{-b\,m_T^2}{z}\right) \tag{1.6}$$

is used for light quarks and gets modified to

$$f_{\mathrm{Bowler}}(z) \;\propto\; \frac{f_{\mathrm{Lund}}(z)}{z^{b\,m_Q^2}} \tag{1.7}$$

for heavy quarks. In these equations,

$z \equiv$ fraction of the available energy plus longitudinal momentum of the string,

$m_T^2 \equiv$ transverse hadron mass $\equiv M_h^2 + p_T^2$,

$m_Q \equiv$ heavy quark mass, and

a and b are free parameters.

1.3 Comparing Theory and Data

The data presented here from experiment E791 are compared to two theoretical models. The first model comes from Mangano, Nason and Ridolfi [8] who have written a Fortran computer program which implements the results of their full next-to-leading order calculations of heavy quark production. This model is restricted to hadronization via a single use of the Peterson fragmentation function. The second model comes from Sjöstrand *et al.* who have written a Monte Carlo event generator, PYTHIA/JETSET [7] (cf Section 2.6). This model only uses leading order matrix elements but includes parton showers to model some of the higher order terms. It also has a more sophisticated hadronization package, described in the previous section. Both models allow the addition of intrinsic k_t to the incoming partons to simulate Fermi motion and virtual emissions/absorptions.

We compare the data to the models described above by measuring various cross sections. The cross section describes the rate at which an interaction occurs. The likelihood of a stream of particles being deflected by a target is dependent on the cross sectional area. Similarly, the effective cross sectional area determines the rate at which charm particle production occurs. The total charm production cross section is simply the cross section summed over all produced charm states and integrated over all kinematic variables. This quantity will be independent of the hadronization mechanism since it only requires knowing how many charm particles are produced, not what

flavor or at what momentum. Differential cross sections are cross sections measured as a function of some kinematic variable. The kinematic variables used should be fairly independent and describe the longitudinal and transverse components of the production. For example, one can choose the longitudinal and transverse momentum of the charm particle. Since the longitudinal momentum distribution will depend strongly on the beam energy, a normalized longitudinal variable is used to make comparisons between experiments easier. This is the Feynman-x scaling variable defined as

$$x_F \equiv \frac{p_z^*}{(p_z^*)_{\max}} \approx \frac{2\,p_z^*}{\sqrt{s}} \tag{1.8}$$

where p_z^* is the charm longitudinal momentum and $\sqrt{s}$ is the energy, both in the hadronic center-of-mass. For the transverse variable we choose p_T^2, the square of the charm particle's transverse momentum.[1] When measuring the differential distribution of one variable, we integrate over all other variables. Unlike the total cross section, the differential cross sections, $d\sigma/dx_F$ and $d\sigma/dp_T^2$, will depend on the hadronization process.

Although we would like to measure the production characteristics of all charm particles, this is well beyond the scope of this thesis. During the hadronization phase, the charm quark can form many different types of charm particles. The most common ground state charm particles are $D^+(c\overline{d})$, $D^0(c\overline{u})$, $D_s^+(c\overline{s})$, and $\Lambda_c^+(cud)$ as well as their charge conjugates (antiparticles).[2] Each of these particles quickly ($\sim$1 ps) decays into one of hundreds of possible decay modes which is what we actually detect.

[1]The longitudinal and transverse momenta are both measured relative to the beam momentum vector on an event-by-event basis. When there are no reconstructed beam tracks ($\approx$5% of the events), the average beam momentum vector is used.

[2]Unless specifically stated otherwise the charge conjugate is assumed to be included throughout this thesis.

In order to get the best measurement using a single produced ground state we use the most copiously produced D^0 and $\overline{D}^0$ states for this analysis. To obtain large numbers of charm particles we want to look for decays which occur frequently and which are efficiently reconstructed. These are the Cabbibo-favored all-charged decay modes. A Cabbibo-favored charm decay is one in which the charm quark decays to a strange quark in contrast to a Cabbibo-suppressed decay in which it decays to a down quark. The latter are suppressed relative to the former by $\tan^2\theta_C$ where $\theta_C \approx 0.22$ radians is the Cabbibo angle. We use all-charged decay modes because charged particle reconstruction is more efficient than neutral particle reconstruction. These criteria leave us with two decay modes, $D^0 \to K^-\pi^+$ and $D^0 \to K^-\pi^+\pi^-\pi^+$, hereafter abbreviated $D^0 \to K\pi$ and $D^0 \to K\pi\pi\pi$. Using two decay modes to measure the same quantity is also helpful in identifying and reducing errors in the analysis.

The remainder of this thesis is divided into six chapters. Next, in Chapter 2, we discuss the experiment E791 used to gather the charm events. In Chapter 3, we describe the reconstruction and event selection process used to obtain our charm sample. In Chapter 4 this sample is shown and the number of observed charm decays is calculated. In Chapter 5 we describe how we correct for unobserved charm decays. In Chapter 6 we present the results of the fully corrected charm cross section and differential cross sections and compare them to the results from the models described above. We also calculate the important systematic errors. Finally, we draw conclusions in Chapter 7.

Chapter 2

The E791 Experiment

The E791 experiment took data between August 1991 and January 1992 at the Fermi National Accelerator Laboratory in Batavia, Illinois. This chapter describes how the π^- beam used by E791 was produced and how the various detectors that made up the E791 experiment worked. First we start with an overview of how fixed-target charm physics is performed.

2.1 Overview of Fixed-Target Charm Detection

The goals of all charm experiments are to produce large amounts of charm particles, efficiently reconstruct the charm particles and efficiently reject non-charm events. The majority of charm results in the past decade have come from experiments which produce charm in one of three ways, e^+e^- annihilation, fixed-target photoproduction and fixed-target hadroproduction. The e^+e^- annihilation production benefits from the cleanest environment but must make do with a fairly small cross section. The main advantages of fixed-target experiments over e^+e^- collision experiments are a higher cross section and boosted charm particles in the laboratory rest frame. The benefit of a higher cross section is clearly better statistics. The benefit of a boosted charm

particle is less obvious and is described below.

In most fixed-target experiments, the first level of charm identification comes from requiring a hadronic interaction. This is easy to accomplish in the trigger decision which determines whether to record an event onto tape. Picking out charm events from other hadronic interactions is a more difficult problem. The most common hadronic interactions, which compose 99% (99.9%) of photo- (hadro-) production hadronic processes, involve strongly decaying resonances and long-lived particles. Since the strongly decaying resonances decay almost immediately, all of the particles in the event appear to come from a common point. This is the production (or primary) vertex. Since a ground state charm particle decays via the weak interaction, it has a lifetime long enough for it to move away from the production point before decaying. The point at which the charm particle decays is the decay (or secondary) vertex. Therefore, if we can find two well-separated vertices in an event, with separation characteristic of the charm lifetime, it is very likely to be a charm event. The average decay length of a particle decay is $<d> = <\beta\,\gamma>\ c\ <\tau>$ where $<\tau>$ is the mean proper lifetime, c is the speed of light, β is the velocity of the charm particle ($\approx$1), and γ is the boost, equal to the particle energy divided by its mass ($\gamma = E/m$). For a D^0 particle, $c\tau$ = (0.3 mm/ps) (0.415 ps) = 0.125 mm. The typical boost for direct $c\overline{c}$ production in an e^+e^- experiment is $\sim$2 while that for a fixed-target experiment is $\sim$30. Therefore, the typical vertex separation will be $\sim$0.25 mm ($\sim$4 mm) for e^+e^- (fixed-target) experiments. Obviously, resolving vertices 4 mm apart is much easier than vertices separated by only 0.25 mm.

The development of techniques to measure the positions of vertices with submillimeter precision is the most important advance in fixed-target charm physics. The first two methods adapted to finding charm vertices were the emulsion and bubble-

chamber detectors. These detectors have the best resolution but the data rate is severely limited. For high-statistics fixed-target charm experiments a silicon vertex system is necessary. A typical silicon vertex system (e.g. as described in Section 2.3.3.1) has a vertex longitudinal resolution of $\sim$300 μm. Therefore, the calculated error on the vertex separation is $\sim$400 μm which gives a separation significance of 4 mm/0.4 mm = 10σ for an average D^0. Requiring a significantly separated vertex is a very powerful method for separating charm events from background events.

Once the promptly produced backgrounds have been sufficiently reduced by requiring a separation significance of $\sim 5\sigma$, another class of backgrounds becomes important. The particles from the production point can interact with the downstream material producing a secondary vertex which mimics a charm decay. This background can be eliminated by requiring the secondary vertex to lie outside of the downstream material. For this to be effective, thin targets should be used with a sufficient air gap to allow most of the charm particles to decay.

Perhaps the most important method for identifying signal from background is through invariant mass reconstruction. Knowing the mass of the particle which decayed, we can determine whether it is consistent with a charm particle. To determine the mass of the decaying particle we need to know the mass and momenta of all of the decay products. In most analyses (including this one) we investigate charm using only one or a few decay channels ($D^0 \to K\pi$ and $D^0 \to K\pi\pi\pi$ in this analysis). Therefore, we already know (with a small ambiguity) the masses of the decay particles. Finding the momentum in a fixed-target experiment is accomplished by tracking the decay particles through one or more dipole magnets. By measuring the change in slope and knowing the magnetic field we can determine the momentum. The E791 downstream

tracking system is described in Section 2.3.3.

2.2 Generating the Beam

The beam starts as H^- ions accelerated to 750 keV by a Cockcroft-Walton accelerator. The hydrogen ions are transferred to a linear accelerator (LINAC) and accelerated to 200 MeV. The H^- ions then pass through a carbon foil which strips off the electrons to create a beam of protons, which is injected into the Booster, a synchrotron with a 75 m radius. The protons are accelerated to 8 GeV in the Booster and delivered to the Main Ring, a 1 km radius synchrotron. The protons reach an energy of 150 GeV in the Main Ring before entering the Tevatron, a superconducting synchrotron directly below the Main Ring in the same tunnel. The Tevatron raises the proton energy to 800 GeV and stores them for delivery to the fixed-target areas. At this point the beam particles are in "buckets" of $\sim$2 ns duration and 19 ns period due to the 53 MHz RF cavities used to accelerate the beam. The 19 ns bucket separation sets the time scale for the entire experiment.

Magnets and electrostatic septa are used to extract the beam in a uniform manner over the course of one "spill." During the 1991/92 run, the spill length was 23 seconds while the interspill lasted 34 seconds. The extracted beam was split into three areas, Meson, Neutrino and Proton. The proton beam was further split into Proton-East (PE), Proton-Center (PC) and Proton-West (PW). The PE line also had a spur which went to Proton-Broadband (PB). The E791 experiment was located at the end of the PE line in the Tagged Photon Laboratory (TPL). Before reaching TPL, the 800 GeV proton beam was directed into a 30 cm long Beryllium primary target. A system of collimators and magnets was used to select a 500 ± 10 GeV negative hadron beam from the produced secondaries. The $\gtrsim$98% pure pion beam was directed

at and focused on the experiment target by means of a string of bending (dipole) and focusing (quadrupole) magnets. The experiment was allocated 2×10^{12} protons per spill at the primary target which resulted in $\sim 4 \times 10^{7}$ pions per spill into TPL. The choice of a negative pion beam is not made at random. The cross section for charm production from a pion beam is significantly greater than that for a proton beam. This is because gluons inside the pion are harder than those inside the proton. Since the main charm production mechanism is gluon-gluon fusion and the total cross section increases with energy, the pion cross section is higher than the proton cross section for charm production at a given beam energy. A negative beam is chosen to eliminate the large proton contamination in the positive beam.

2.3 The Spectrometer

The spectrometer, illustrated in Fig. 2.1, was an upgraded version of the apparatus used in Fermilab experiments E516 [9], E691 [10], and E769 [11]. Figure 2.1 only shows the detectors downstream of the experimental target; the beam tracking devices, described below, are not shown. The major differences between E769 and E791 were the addition of more planes of silicon microstrip detectors (SMD's), enhancement of the muon identification system, new front-end detector-signal digitizers and a new data acquisition system. The most important part of the spectrometer for this analysis was the charged-particle tracking system.

The coordinate system was defined to be a right-handed coordinate system in which increasing z is in the beam direction, x is the horizontal dimension and y increases vertically upward. The w, u and v axes were rotated by $+60°$, $+20.5°$ and $-20.5°$ with respect to the positive x axis. The spectrometer was approximately centered on the beam line. The $z = 0$ point is set 2.1 cm downstream of the most

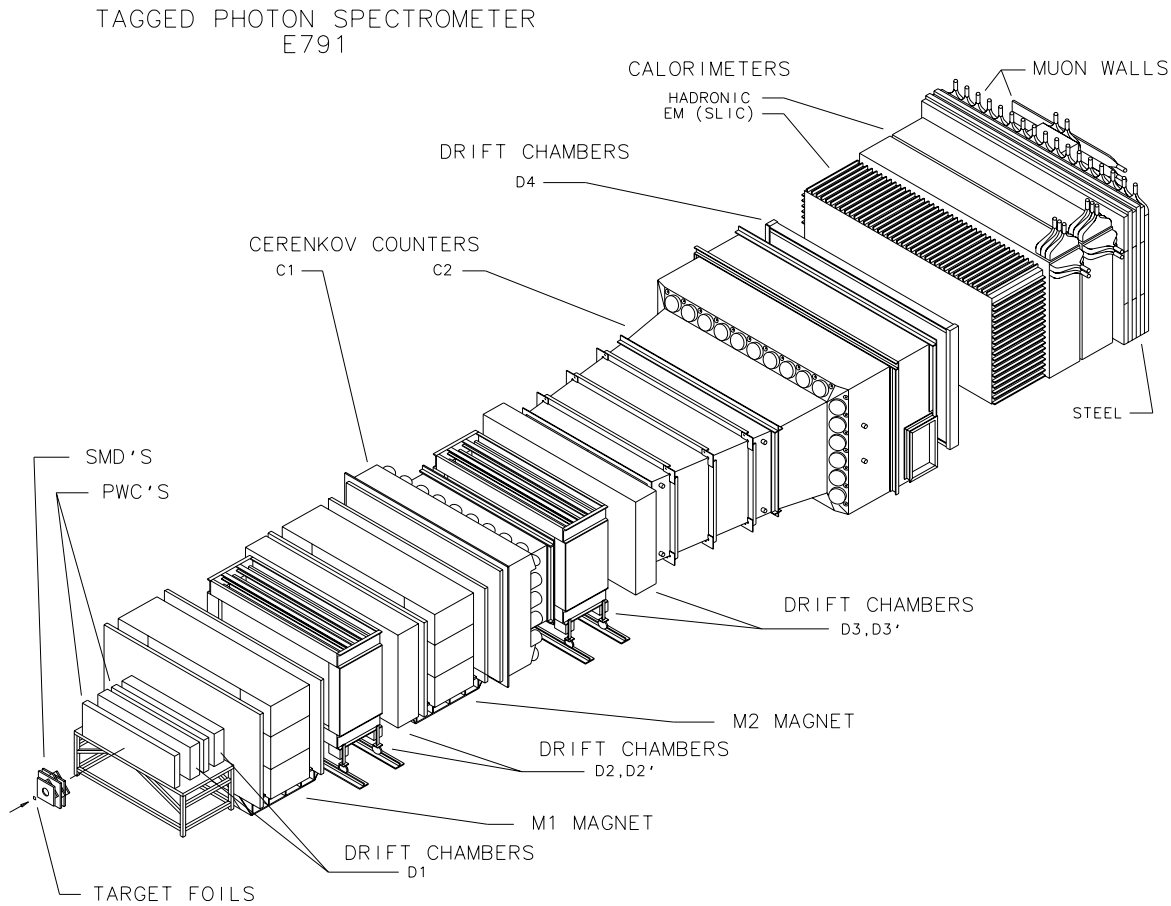

Fig. 2.1.— The E791 spectrometer.

downstream target.

2.3.1 Beam Tracking

The π^- beam particles were tracked with eight Proportional Wire Chamber (PWC) planes and six Silicon Microstrip Detector (SMD) planes upstream of the target region.

The PWC's are composed of alternating (in z) layers of instrumented anode wires, near ground, and cathode planes, at high (negative) voltage. An incident charged particle ionizes the gas, liberating electrons and ions which drift toward the anode and cathode, respectively. At a point close to the anode, the electric field

accelerates the drifting electrons enough to ionize other electrons which causes an "avalanche," resulting in a gain of several orders of magnitude. This signal is amplified and latched. The beam PWC's [12] had a wire spacing of 1 mm and were arranged in two stations widely separated in z so as to measure the angle of the incoming beam particle with high precision. The first station was 31 m upstream; and the second was 12 m upstream. Each station consisted of 4 planes: two x planes staggered by 1/2 of a wire spacing in x, a y plane and a w plane. The gas used for the PWC's was an 80%/20% mixture of Ar/CO_2 plus $\sim 0.3\%$ freon.

The silicon planes used by E791 are composed of many ($\sim$1000) reverse-biased silicon strips per plane. A charged particle passing through each 300 μm thick silicon plane releases $\sim$25000 electron-hole pairs. The image charge of the electrons and holes are collected at the end of the strips by a preamplifier, the output of which is amplified and latched. The upstream (beam) SMD's had a pitch of 25 μm and were arranged in two stations, each with an x, y and w plane. The first SMD station was 78 cm upstream and the second station was 31 cm upstream. The most upstream x and y planes, installed for E769, were 85% efficient, while the other four beam planes, added for E791, were 91% efficient.

For triggered events (cf Section 2.4), the pion beam had RMS spreads in x and y positions at the target of 0.16 cm and 0.18 cm, respectively. The mean (RMS) xz and yz beam angles were -0.26 (0.27) milliradians and 0.96 (0.08) milliradians, respectively.

2.3.2 The Target

As mentioned in Section 2.1, requiring the decay vertex to be located outside of the target greatly reduces background from secondary interactions. Segmenting the target, as was done in E791, allows more air gaps in which the charm can decay, mak-

Target Number	1	2	3	4	5
Material	Platinum	Carbon	Carbon	Carbon	Carbon
z position (cm)	-8.164	-6.680	-5.141	-3.599	-2.056
Thickness (cm)	0.052	0.1572(3)	0.1567(3)	0.1530(3)	0.1585(3)
Diameter (cm)	1.606	1.369(2)	1.377(3)	1.368(2)	1.360(7)
Mass (g)	2.2396	0.7490(2)	0.7507(2)	0.7373(2)	0.7523(2)
Computed Density (g/cm^3)	21.3	3.238(15)	3.217(18)	3.278(16)	3.267(39)
Pion Interaction Lengths (%)	0.381	0.384	0.381	0.379	0.392
Nuclear Interaction Lengths (%)	0.586	0.591	0.586	0.583	0.603
Radiation Lengths (%)	16.9	1.2	1.2	1.2	1.2

Table 2.1: E791 target information. Approximately 5% of the data (not used in this analysis) were taken with 1 platinum and 3 carbon targets. Figures in parentheses give 1-σ uncertainties in the last place(s).

ing the out-of-target criterion more efficient. The use of platinum as a target material is motivated by the fact that charm production increases linearly [13] with the atomic number, A, while the inelastic cross section, which produces most of the background, only increases as $A^{0.71}$ [14]. Thus, the charm signal to background ratio in platinum is enhanced relative to that in lighter targets. Also, its high density means that the platinum target can be thinner for the same number of interaction lengths than less dense, lower A targets. The advantages of a thin target are good localization of the primary vertex and, for a given air gap, closer placement to the downstream SMD system, which increases acceptance. The disadvantage of the platinum target is that it is also high Z, so that it causes more multiple scattering, which makes the measurements of tracks and vertices less precise. Also, photons from π^0 decays are more likely to convert into e^+e^- pairs, resulting in more tracks and greater confusion. Therefore, only the most upstream target was made of platinum. The downstream targets were made of industrial diamond. These were $\sim$3 times thicker but contained less than 1/12 the number of radiation lengths which determines the amount of scattering and

number of photon conversions.

2.3.3 Downstream Tracking

The charged-particle tracking system downstream of the target consisted of 17 SMD planes, two PWC planes, and 35 drift chamber planes. In general, several planes of tracking chambers with different angular orientations around the beam axis were grouped together in each tracking station to provide hit ambiguity resolution.

2.3.3.1 Vertex Silicon

The E791 silicon microstrip detector system is described in Table 2.2 and information about the E691 silicon system can be found in references [15] and [16] .

2.3.3.2 Drift Chambers

Like a PWC, a drift chamber (DC) is composed of alternating layers of cathode planes and anode planes. For E791, the anode planes contained alternating sense (anode) wires near ground and field-shaping (cathode) wires at a negative high voltage. The cathode planes were also constructed of wires and held at a negative potential. The rectangular area defined by two cathode planes and two field-shaping wires is a "cell" with a sense wire in the middle. The electrons ionized by the passing of a charged particle follow a nearly straight line to the sense wire. Throughout most of the cell, the electrons travel at a uniform velocity and by measuring the time it takes to collect the charge we determine how far from the wire the charged particle passed. This was accomplished by using a time-to-digital converter (TDC) on each DC anode wire. To resolve the left-right ambiguity (which side of the wire the particle passed) we need at least three views. Near the anode, the electric field increases sharply, generating an electron avalanche from the drifting electrons and giving rise to measurable signals.

Plane	z position (cm)	strip pitch (μm)	Efficiency (%)	Acceptance (mr)	View	First Experiment
1	0.518	25 : 50	83	$\pm 328 : \pm 674$	y	E769
2	0.848	25 : 50	85	$\pm 302 : \pm 620$	x	E769
3	2.195	50 : 50	93	$\pm 235 : \pm 233$	x	E691
4	3.293	50 : 50	95	$\pm 195 : \pm 194$	y	E691
5	6.957	50 : 50	96	$\pm 125 : \pm 124$	v	E691
6	11.314	50 : 50	98	$\pm 132 : \pm 174$	y	E691
7	11.629	50 : 50	97	$\pm 129 : \pm 170$	x	E691
8	15.241	50 : 50	94	$\pm 104 : \pm 137$	v	E691
9	20.210	50 : 50	90 [a]	$\pm 106 : \pm 108$	x	E691
10	20.519	50 : 50	88	$\pm 105 : \pm 107$	y	E691
11	24.165	50 : 50	93	$\pm 91 : \pm 93$	v	E691
12	27.280	50 : 200	98	$\pm 159 : \pm 147$	v	E653 [b]
13	31.679	50 : 200	96	$\pm 139 : \pm 129$	x	E653 [b]
14	34.388	50 : 200	98	$\pm 129 : \pm 120$	y	E653 [b]
15	37.022	50 : 200	99	$\pm 120 : \pm 112$	x	E653 [b]
16	39.714	50 : 200	99	$\pm 113 : \pm 105$	y	E653 [b]
17	45.287	50 : 200	99	$\pm 100 : \pm 93$	v	E653 [b]

Table 2.2: Parameters of the E791 downstream SMD planes. The strip pitch is given for the inner:outer region of the detector. "View" refers to the coordinate measured by that plane, with $v = -20.5^\circ$ to $+x$. The acceptance is parallel:perpendicular to the view direction for a decay at $z = -3.25$ cm, the average z position for the D^0 events in this analysis.

[a] 57% efficient for the first 15% of the data used in this analysis.

[b] New amplification and digitization electronics for E791.

Most of the drift chambers used in E791 were originally built for E516 while the rest were added for E691. They were arranged in four stations as illustrated in Figure 2.1. Each station was subdivided into substations with plane orientations such that an $x-y-z$ space point could be reconstructed in each substation and combined to give a slope for the station. The characteristics of these chambers are given in Table 2.3. The E791 drift chambers used a 90%/10% mixture of Ar/CO_2 plus $\sim 1\%$ freon. Each of the D1 substations was augmented by a PWC which measured the y coordinate. These PWC's had a wire spacing of 2 mm.

Station	D1	D2	D3	D4
Approximate size (cm)	130 × 75	280 × 140	320 × 140	500 × 250
Number of substations	2	4	4	1
Views per substation	$x,\ x',\ u,\ v$	$u,\ x,\ v$	$u,\ x,\ v$	$u,\ x,\ v$
u and v cell size (cm)	0.446	0.892	1.486	2.974
x cell size (cm)	0.476	0.953	1.588	3.175
z position of first plane	142.5	381.4	928.1	1738.0
z position of last plane	183.7	500.8	1047.1	1749.4
Approximate resolution (μm)	400–500	330–420	260–350	500–900
Typical efficiency	93% [a]	94%	93%	85%

Table 2.3: Characteristics of the E791 drift chambers. "View" refers to the coordinate measured by that plane, with $u = +20.5°$, $v = -20.5°$ and x' is staggered by one-half a wire spacing relative to the x plane. The efficiencies and resolutions are for the region outside the central inefficient area. The range of resolutions encompasses the entire run period.

[a] The second pair of u and v planes were dead for the first 15% of the data used in this analysis.

The E791 beam, operating at 2 MHz, creates a very high-rate environment for the part of the drift chambers in the vicinity of the beam. This high-rate environment causes a decrease in efficiency due to space-charge build up. Space-charge buildup is caused by ions not being collected fast enough on the cathode, resulting in a build up of positive charge and reducing the electric potential seen by the electrons. This

should be rate dependent but not time dependent. However, this effect can be aggravated by polymerization which occurs when ions, usually from organic compounds, are neutralized on the cathode. The resulting substance can coat and insulate the cathode, increasing the time it takes ions to be neutralized. This effect should be time dependent. One reason the E791 experiment operated with an inorganic gas mixture, Ar/CO_2, instead of the more usual Ar/Ethane, was to avoid this problem. However, it has been found that the efficiency in the center of the drift chambers, as well as the resolution, degraded significantly during the course of the run while the instantaneous rate did not. The cause is not proven although it could be from polymerization due to contaminants in the gas. Also, chambers which were cleaned for the E769 run showed a smaller loss of efficiency relative to the chambers which were not cleaned. Therefore, history can also affect the performance. The net result is an approximately Gaussian inefficiency, or "hole," in the central region with a peak inefficiency of 100% and a width increasing from 4.0 mr to 7.0 mr. The D1 and D4 detectors had widths approximately 50% greater, but were the least important chambers for this analysis. The result of this degradation is clearly seen in the rapid drop in acceptance with increasing x_F in Fig. 2.2

2.3.3.3 Magnets

Momentum analysis was provided by two dipole magnets that bent particles in the same direction in the horizontal plane. The transverse momentum kicks were 212 MeV/c for the first magnet and 320 MeV/c for the second magnet. The centers of the two magnets were 2.8 m and 6.2 m downstream of the targets. The $x-y$ aperture of the first magnet was 183 cm by 81 cm and that of the second was 183 cm by 86 cm.

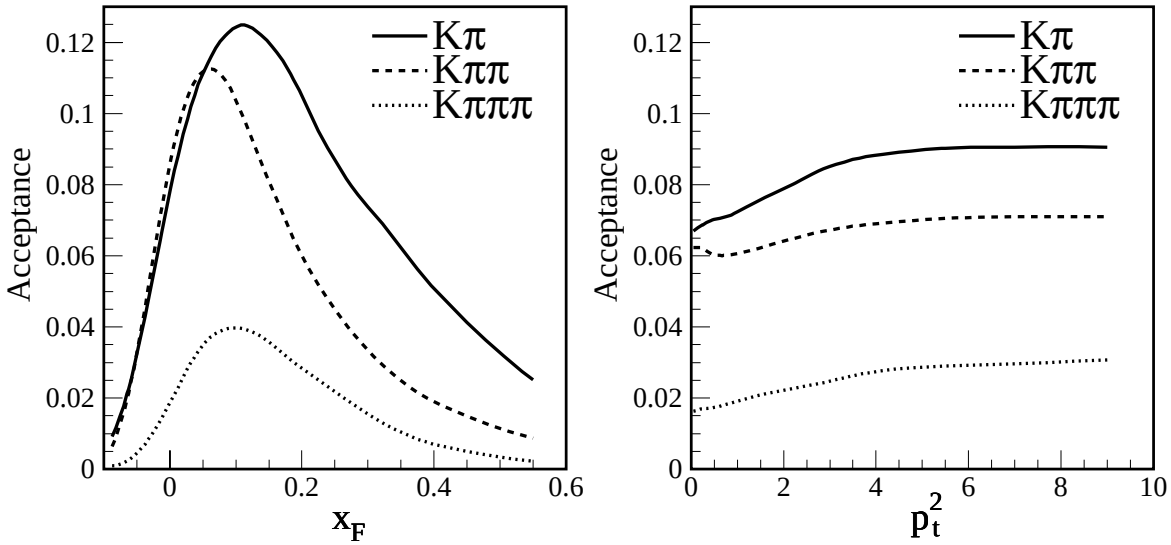

Fig. 2.2.— E791 acceptance functions vs. x_F and p_T^2 for $K\pi$, $K\pi\pi$ and $K\pi\pi\pi$ candidates. The p_t^2 acceptance is obtained for charm mesons with $-0.1 < x_F < 0.6$.

2.3.4 Čerenkov Counters

Two segmented, gas-filled, threshold Čerenkov counters [17] provided particle identification over a large range of momenta. The threshold momenta above which a charged particle emits light were 6, 20 and 38 GeV/c for π's, K's, and p's, respectively, for the first counter, and 11, 36, and 69 GeV/c for the second. The pulse heights seen in photomultiplier tubes (PMT's) looking at each of the mirrors were digitized by analog-to-digital converters (ADC's) for each event trigger. The offline particle identification algorithm correlates the Čerenkov light observed in a given mirror-phototube segment with the charged particle tracking information. The algorithm indicates the likelihood that a charged particle of a given mass could have generated the observed Čerenkov light in the segment(s) in question. Čerenkov information was not used in this analysis (cf Section 3.3.2).

2.3.5 Calorimeters

The electromagnetic calorimeter [18, 19] was a Segmented Liquid Ionization Calorimeter (SLIC) consisting of 20 radiation lengths of lead and liquid scintillator and located 19 m from the target. Layers of scintillator counters 3.17 and 6.24 cm wide were arranged transverse to the beam and their orientations alternated among horizontal and $\pm 20.5^\circ$ with respect to the vertical direction. The hadronic calorimeter [20] consisted of six interaction lengths of steel and acrylic scintillator. There were 36 layers each with a 2.5-cm-thick steel plate followed by a plane of 14.3-cm-wide by 1-cm-thick scintillator slats; the slats were arranged alternately in the horizontal and vertical directions, and the upstream and downstream halves of the calorimeter were summed separately. The signals from the hadronic calorimeter as well as those from the electromagnetic calorimeter were read out for each event trigger using ADC's and were used for electron identification [21, 22, 23]. Calorimeter particle identification was not used in this analysis.

2.3.6 Muon Detectors

Muons were identified by two planes of scintillation counters located behind a total of 15 interaction lengths of shielding, including the calorimeters. The first plane, 22.4 m from the target, consisted of 12 40-cm-wide by 300-cm-long vertical scintillation counters in the outer region and three counters 60 cm wide in the central region. This plane was not very efficient, and was used for only a very few analyses. The second plane, added for E791, consisted of 16 scintillation counters 24.2 m from the target. These counters were each 14 cm wide and 300 cm long, and measured position in the vertical plane. These counters were equipped with TDC's as well as latches in order to provide some indication of the horizontal position of the incident muons. Muon

identification was not used in this analysis.

2.4 Trigger and Data Acquisition

Triggering information came from several sources. The beam spot counter was a circular scintillation detector, 1.27 cm in diameter, located at $z = -22.7$ cm. The beam halo counter, located at $z = -16.3$ cm, was a 7.62 cm square scintillator with a 0.97 cm diameter hole in the middle. The interaction counter was a square scintillation detector, 3.97 cm across, located between the targets and silicon system at $z = -0.1$ cm. The scintillation counters were connected to PMTs, the outputs of which were sent to discriminators. The high voltage settings of the PMTs were adjusted several times during the run to maintain the same response to minimum ionizing particles (MIPs). Total energy and transverse energy from the SLIC and hadron calorimeter were also used by the trigger. The total energy was an analog sum of the PMT dynode outputs weighted differently for the SLIC and the hadron calorimeter. The transverse energy (E_T) was obtained similarly but with each phototube output also weighted by the angle between the beam axis and a line between the appropriate scintillator and the target.

From the above inputs, several logic (NIM) signals were formed. A MIP is defined as the most probable signal from a minimum ionizing particle. In general, in order to be 100% efficient for a single particle, the threshold for a discriminator is set at one-third to one-half of a MIP. BEAM_SPOT_LOW gave a 9 ns true pulse if the beam spot counter registered a hit more than one-third of a MIP. BEAM_SPOT_HIGH gave a 10 ns true signal if the beam spot counter registered a hit significantly greater than 2 MIP. HALO was on for 27 ns if the beam halo counter signal was greater than one-third of a MIP. INTERACTION_LOW gave a 25 ns true pulse if the interaction counter registered a

hit greater than one-half of a MIP. INTERACTION_HIGH was true for 14 ns if the interaction counter signal was more than approximately 4.5 MIP. GOOD_BEAM required a coincidence of BEAM_SPOT_LOW and not HALO. GOOD_BEAM_TARGET_INTERACTION required a coincidence of BEAM_SPOT_LOW and INTERACTION_HIGH and not HALO to be true. These coincidences each stayed on for 50 ns. NEARLY_IN_TIME_BEAM was true if the interaction counter registered another hit within $\pm$78 ns of the original hit. ET was true if the transverse energy was greater than $\sim$3 GeV while ETOT_TOO_HIGH was true if the total energy was greater than $\sim$800 GeV. The BEAM_SPOT_HIGH was actually set such that it eliminated $\approx$5% of the beam tracks which corresponds to a discriminator threshold of 2 MIP. The discriminator threshold for the INTERACTION_HIGH input was set by analyzing the ratio (INTERACTION_HIGH counts / INTERACTION_LOW counts) versus INTERACTION_HIGH threshold. At a threshold of about 4.5 MIP, this ratio is $\approx$2.5% with the targets in and 0.5% with the targets out. Since the total interaction length of the targets is 2% (Table 2.1), this threshold is consistent with a hadronic interaction requirement while suppressing the Landau-tail from straight-through pions.

Two types of data triggers, prescaled interaction (9%) and E_T (91%), were taken by E791 although only the E_T triggers are used in this analysis. The pretrigger is the same in both cases and simply required GOOD_BEAM_TARGET_INTERACTION be true. If the experiment was "live," that is, not currently reading out data or processing a previous pretrigger, the pretrigger signal was used to strobe a LeCroy model 4508 programmable lookup unit (PLU) which was used to determine the full experiment trigger. For the interaction trigger, the PLU required NEARLY_IN_TIME_BEAM, BEAM_SPOT_HIGH and ETOT_TOO_HIGH all be false. The primary motivation for all of these requirements was to eliminate events with more than one beam particle. The

BEAM_SPOT_HIGH was also intended to eliminate events with an upstream interaction. The long (156 ns) window for the NEARLY_IN_TIME_BEAM requirement was made necessary by the integration time of the calorimeters. The E_T trigger added the ET requirement to the interaction trigger requirements. This reduced the data rate by a factor of two while retaining all of the reconstructible charm.

The time for the full hardware trigger decision was about 470 ns. For each trigger, a total of 24,000 channels were digitized and read out in 50 μs with a parallel-architecture data acquisition (DAQ) system [24]. Events were accepted at a rate of 9 kHz during the 23-second Tevatron beam spill. The typical recorded event size was 2.5 kbytes. Data were written continuously (during the 23-second spill and the 34-second interspill periods) to 42 Exabyte 8200 8mm tape drives at a rate of 9.6 Mbytes/s. Over 2×10^{10} hadronic interactions were recorded on 24,000 tapes.

2.5 Scalers

While the standard DAQ system provided a great deal of information about each triggered event, it does not provide any information about what is happening during non-triggered events. This information, however, is necessary for measuring the cross section. In order to measure a cross section, we need to know what fraction of the beam particles produced a charm event. Therefore, we need to know how many beam particles passed through the target while the experiment was live, not just how many beam particles resulted in a trigger. This type of information is collected through the use of scalers which are used to count events. Two types of LeCroy scalers were used in E791. The 20 MHz 4432 ECL-input scalers were used to count trigger PLU inputs and outputs. Rapidly changing inputs such as beam counters were counted with 100 MHz 2551 NIM input scalers. Since the accelerator operated at 53 MHz and

the typical beam rate was ~2 MHz, these scalers were fast enough to count any rate present in the experiment. The scalers were read out and written to disk at the end of each spill. This scaler information, along with visual scalers present in the counting room, gave nearly instant access to the state of the experiment, especially the beam. Of the 87 scalers read out in E791, 28 of them were used for muon information and the rest for trigger information (including the trigger scintillators).

2.6 The Monte Carlo

The scaler information allows us to account for beam particles which did not produce an event which we wrote to tape. However, not every charm particle that was produced at the target and subsequently decayed to either of the states used for this analysis resulted in a trigger and was written to tape, nor was every charm decay of this type that was written to tape correctly identified as signal. The geometric acceptance, as well as detector and reconstruction efficiency results in an overall acceptance much smaller than 100% as can be seen in Fig. 2.2. To measure this efficiency we use a Monte Carlo technique. A computer program was written which simulates the production and decay of the charm particle of interest. The program also simulates the response of the E791 detectors to this generated event.

The program which simulates the event itself is the public domain event generator PYTHIA/JETSET [7] which simulates the entire pion-nucleon interaction and decays all unstable particles. After the event generation, the detector simulation is performed. The first part of the detector simulation traces each particle through the detector including magnetic field effects, multiple Coulomb scattering, hard interactions, conversions, etc. This result is the basis of the "truth-table" information which is the correct representation of the event. The second phase of the detector simu-

lation is the digitization. Using the known sizes, efficiencies and noise rates of the various detectors, output is produced in the same format as the real experiment. The Monte Carlo technique where a random number is selected to decide a choice is used throughout the program. For example, the event generation randomly picks a decay time for an unstable particle using the known exponential distribution; the event tracing randomly selects from a distribution the amount of multiple Coulomb scattering a particle undergoes at each slice of the detector; the digitization selects a random number from a flat distribution and compares it with the efficiency to determine if a particular detector element is on.

The output of the Monte Carlo program results in "fake" data of the exact same format as the real data. The Monte Carlo data are processed by the same programs used for the real data. By comparing the charm decays of a particular type that were reconstructed to the number of that type that were generated, as indicated in the truth-table, we can determine the acceptance for each decay type, as shown in Fig. 2.2. This is described in greater detail in Chapter 5.

Chapter 3

Event Reconstruction and Selection

The 20 billion interactions recorded by E791 onto 24,000 8 mm tapes comprise about 50 Terabytes of data. These data needed to be reconstructed and pared down to a manageable size. First, all events were reconstructed and filtered using loose criteria that were designed to enhance the charm content of the remaining data. Further data reduction was effected in a second stage of data processing in which tighter requirements were placed on the events to further enhance the charm content and in which the data were also split into separate subsamples organized by physics goals. The reconstruction and multiple reduction stages are shown in Table 3.1.

Stage	Outputs	Tapes out	Events out
1. Raw Data	1	24,000	20×10^9
2. Reconstruction/Filtering	1	13,000	3×10^9
3. Stripping	2	3,500	1×10^9
4. Substripping	15	300	500×10^6
5. Microstripping	$\sim$50	33	30×10^6
6. Analyses	$\sim$50	2	1×10^6

Table 3.1: Stages of event reconstruction and reduction. The number of output tapes and events are for this analysis.

3.1 Filter and Reconstruction

Event reconstruction and filtering took place over a period of two and a half years at four locations: the University of Mississippi, The Ohio State University (moved to Kansas State University in 1993), Fermi National Accelerator Laboratory, and Centro Brasileiro de Pesquisas Físicas, Rio de Janeiro, Brazil (CBPF). The first three sites used clusters of commercial UNIX/RISC workstations controlled from a single processor with multiprocessor management software [25, 26, 27], while CBPF custom-built ACP-II single-board computers [28, 29].

3.1.1 Event Reconstruction

The event reconstruction program takes the raw data from all of the detectors and attempts to construct higher-level objects such as tracks, vertices and showers. This information is also stored on 8 mm tapes in a format called DST (Data Summary Tape).

3.1.1.1 Track Reconstruction

The first stage in the event reconstruction is the track finding. The first track to be reconstructed is the beam track. Using the hits from the upstream PWC and SMD planes, all possible straight lines are formed and the best track, based on the χ^2 and the number of hits, is kept. The beam track reconstruction efficiency is $\sim$95%.

Following the beam track reconstruction, SMD tracks are formed using the 17 downstream silicon planes. This is done by constructing single-view tracks in each of the three views and then forming three-view tracks from these single-view tracks. The three-view tracks are ordered by quality, determined from the number of hits, number of unique hits and the χ^2 of the tracks. These tracks, starting with the best one, are

projected into the drift chamber system.

The drift chamber reconstruction starts by constructing all the "triplets" for D2, D3 and D4. The "triplets" are space-point measurements which come from the u, x, and v views of each plane. The SMD tracks are projected into D3 in the non-bend (y) view and a region of about ± 2.5 cm is searched for matching triplets. For each matching triplet, "roads," $\sim$4 mm wide, are created in the other views using the SMD information and an approximation to the magnetic field. The roads are searched for hits in D3, D2, D4 and D1 to identify track candidates. These candidates must satisfy the following requirements: out of the 12 planes in each of D3 and D2, a minimum of 8 hits are required in D3, 5 hits in D2, 14 hits in D3+D2 and 11 hits in the 17 SMD planes and 12 D2 planes. A χ^2 minimization fit is performed on the track candidates to determine the slopes, intercepts and momenta taking into account multiple scattering. During this fit, hits can be added, subtracted and swapped. After this final fit, the resulting track candidates are required to have at least eight SMD hits, five D2 hits, five D3 hits, seven D2+D3 hits, $\geq$50% unique DC hits from D2 and D3. The track candidates are also required to have $\chi^2<5$ and $\geq$50% unique SMD hits or $\chi^2<3$ and $\geq$75% unique DC hits from D2 and D3. The SMD segments, drift chamber triplets and hits used by the tracks that pass these criteria are marked to discourage sharing. When this process is completed, the remaining SMD tracks are projected into D2 to look for tracks which do not make it through the second magnet. These tracks require at least 8 hits in D2 and 15 hits in the 17 SMD planes and D2. In the final fit, these tracks are required to have at least 19 total hits in the 17 SMD planes, 8 D1 planes, 2 PWC planes and 12 D2 planes, 8 hits in the SMD planes, 5 hits in the D2 planes, $\geq$50% unique hits in D2 and $\geq$50% unique hits in the SMD's. Tracks found this way, with SMD and drift chamber hits, are called SESTR (Silicon + ESTR) tracks.

Drift chamber only tracks are found in a similar fashion but without the SMD seed. These "ESTR (Exhaustive Search Track Reconstruction)" tracks are not used in this analysis.

3.1.1.2 Vertex Reconstruction

The vertex reconstruction attempts to combine tracks into a common point of origin (vertex). The vertexing algorithm starts by finding the primary vertex. The beam track, if available, is used to seed the vertex. SESTR tracks are then combined to form a vertex. A track is kept in the primary vertex if its χ^2 contribution to the vertex fit is low enough. The primary vertex is also loosely required to lie inside one of the targets. SESTR tracks which are not part of the primary are used to find secondary vertices with track sharing between vertices discouraged. The list of the vertices found is referred to as the "vertex list." The vertex list is often used in a "topology-driven" approach where a detached secondary vertex is the primary requirement. An alternative method, the "candidate-driven" or "mass-driven" approach looks for specific decay modes in a specific mass region, allowing the relaxation of some of the vertex detachment cuts. The vertex list is the starting point for this analysis.

3.1.1.3 Particle Identification Reconstruction

Particle identification information for the charged tracks comes from three sources, the Čerenkov counters, the calorimeters and the muon counters. No particle identification information was used in this analysis.

3.1.2 Filtering

During the event reconstruction, a filter was applied which kept ~15% of the events. To pass this filter, an event was required to have a reconstructed primary pro-

duction vertex whose location loosely coincided with one of the target foils. The E791 data were reconstructed with two versions of the reconstruction and filter program. The first version, Release 5, required at least one of the following:

1. At least one reconstructed secondary decay vertex of net charge 0 for an even number of decay tracks and ± 1 for an odd number of decay tracks. The significance of the longitudinal separation of the secondary vertex from the primary had to be at least four for secondary vertices with three or more tracks and at least six for those with two tracks. This is the most relevant criterion for this analysis.

2. At least one reconstructed $K_s \to \pi^- \pi^+$ or $\Lambda \to p\pi$ candidate whose decay was observed upstream of the first magnet.

3. At least one reconstructed $\phi \to K^+ K^-$ candidate. The first 20% of the processed data did not have this requirement.

The second version used to reconstruct and filter the data, Release 7, also allowed several other classes of events, most importantly:

4. Events in which the net charge of all the reconstructed tracks was negative, their total momentum was greater than 350 GeV/c and the net p_T was less than 2 GeV/c.

5. $K_s \to \pi^- \pi^+$ or $\Lambda \to p\pi$ candidates that decayed inside the aperture of the first magnet.

6. The ϕ requirement was replaced by a direct search for $D_s \to \phi + X$ where X is a charged track and $P \to p\phi\pi, pK^*K$ where P is a pentaquark.

3.1.3 Release 5 and Release 7 Comparison

Besides the additional event classes allowed by the Release 7 filter, described above, there were several other differences in the Release 5 and Release 7 versions of the reconstruction programs. The Release 5 momentum determination was made assuming a single-bend-point approximation for the magnetic fields of the magnets. The single-bend approximation assumes that the particle is bent once at the center of eachmagnet. For Release 7, a full-field algorithm was implemented which is a more accurate representation of the effect of the magnetic fields. In addition, a kink found between the SMD and drift chamber coordinate systems was accounted for in the Release 7 tracking algorithm. These changes affect the mass and mass resolution of the D candidates. The average $K\pi$ ($K\pi\pi\pi$) mass is $\sim$1 MeV/c^2 ($\sim$0.5 MeV/c^2) higher in Release 5 than Release 7. In addition, the mass and mass resolution x_F dependencies are different between the two releases as shown for the $K\pi$ data and Monte Carlo in Fig. 3.1.

The other major changes made for Release 7 primarily affected reconstruction efficiency. The drift chamber resolutions were updated more frequently. Also, the drift chamber resolutions were made position dependent. This was to account for resolution degradation near the center of the drift chambers caused by the incident π^- beam. Since the resolutions were used to determine the window size allowed for finding hits during the track reconstruction, degrading the resolution actually increases the reconstruction efficiency. The effect on the $K\pi$ and $K\pi\pi\pi$ acceptance versus x_F is shown in Fig. 3.2.

Finally, minor changes were made in some calculations and in what information was written out. One of the changes was the calculation of the χ^2/dof of a track. It was found that the Release 5 average χ^2/dof was a function of momentum. A post hoc

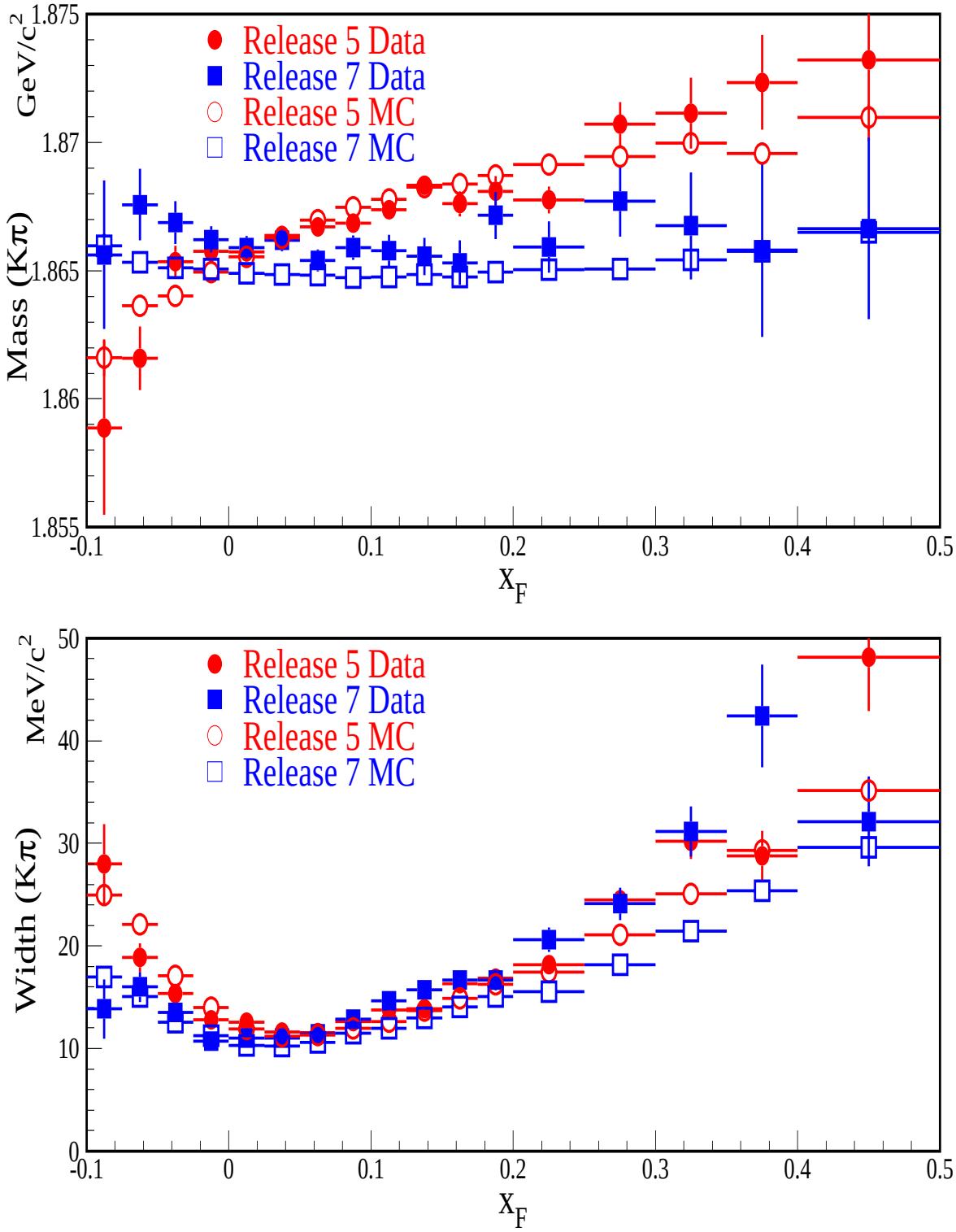

Fig. 3.1.— $K\pi$ mass (top) and width (bottom) versus x_F for data and Monte Carlo events reconstructed with Release 5 and Release 7.

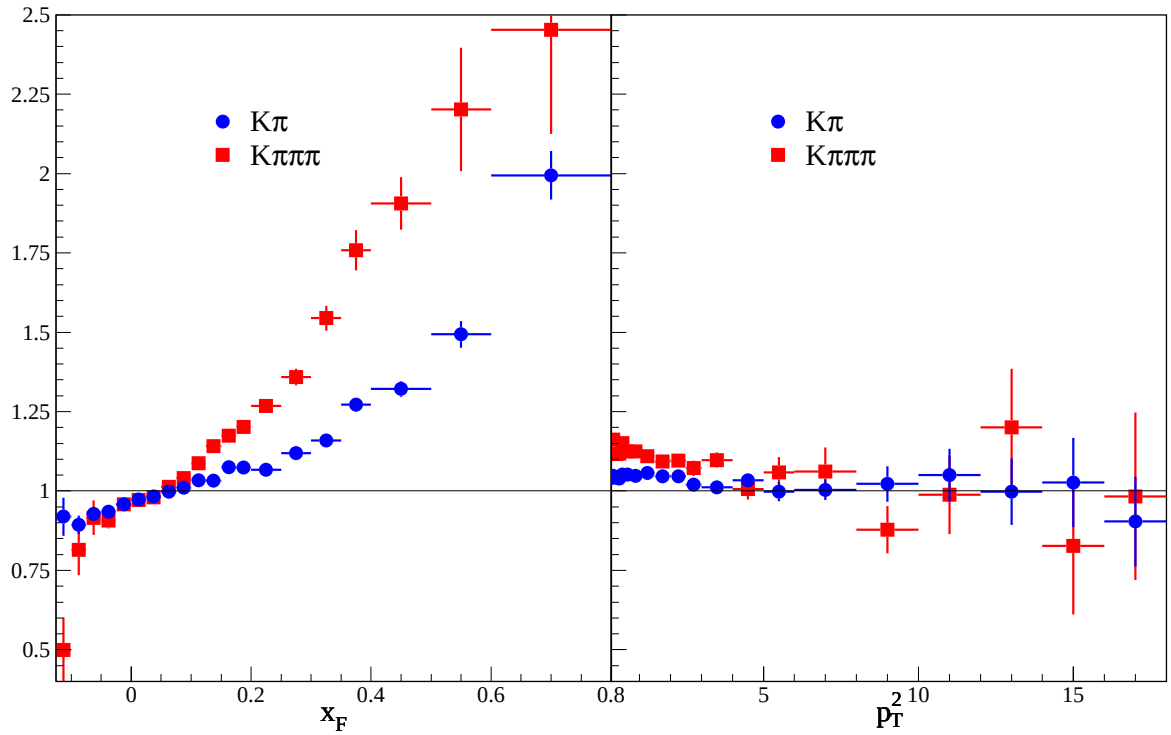

Fig. 3.2.— Ratio of Release 7 acceptance to Release 5 acceptance as a function of x_F (left) and p_T^2 (right) for $K\pi$ and $K\pi\pi\pi$.

correction was made to the Release 5 data while a more accurate χ^2/dof was calculated for Release 7. Also, in Release 5, the χ^2/dof of the fit to a track was required to be less than 6.5 while in Release 7 the limit was 5. Neither of these requirements is very restrictive. Another change was in the calculation of the momentum error. Due to a couple of programming mistakes, the only error which was propagated correctly is the momentum error for positively charged Release 5 tracks. Therefore, the momentum errors for negatively charged Release 5 tracks and all Release 7 tracks are obtained from a fit to the momentum error as a function of momentum for the positively charged Release 5 tracks. Because the geometry is better determined and the magnetic field treatment is more correct in Release 7 than Release 5, the Release 7 momentum error is probably overestimated, relative to the Release 5 error, by this approach.

Approximately three-fourths of the E791 data were reconstructed with Release 5, the rest, with Release 7.

3.2 Stripping, Substripping and Microstripping

The stripping, substripping and microstripping were designed to reduce the data which needed to be processed for a given analysis by splitting the data into more analysis-specific data sets and by applying more stringent requirements. This strip program was run on the filtered data at the same institution where the data reconstruction took place with the exception of the CBPF data, which was stripped at Fermilab. The strip generated a tag for each event that indicated which of the physics requirements the event passed. Events which passed one of the physics requirements designed to find events with a secondary vertex significantly displaced from the primary vertex were written to Stream A. Events which passed one of the physics requirements designed to keep events with a long-lived particle (e.g. K_S^0 or Λ^-) were sent to Stream B. The data used in this analysis came from Stream A.

The substrip and microstrip for this analysis were performed at Kansas State University. In both cases the number of events was reduced by imposing more restrictions on the event and selecting fewer charm decay modes. The final 33-tape microstrip includes two, three and four prong charm decay candidates. These contain secondary vertices with two, three or four charged tracks with a calculated invariant mass for the most common decay modes within ~200 MeV/c^2 of the nominal D^0, D^+, D_s^+ or Λ_c^+ mass.

3.3 The Final Sample

3.3.1 Determining selection criteria

The final sample actually consists of two candidate D^0 decay samples, the $K\pi$ sample, and the $K\pi\pi\pi$ sample. To obtain the $K\pi$ sample the 33 microstrip tapes were run through a program which selected events with a two-prong vertex in the vertex list which satisfied all of the microstrip requirements and a couple of additional loose cuts. The $K\pi\pi\pi$ sample was obtained in a similar fashion. However, while the global vertexing algorithm used to create the vertex list was reasonably efficient for two and three prong modes, it was not as efficient for four prong modes. Therefore, for the $K\pi\pi\pi$ mode, events with three-prong vertices as well as those with four-prong vertices were examined. For the three-prong vertices, the vertex was required to pass the three-prong microstrip criteria. Then a loop through all tracks which were not included in either the primary or secondary vertex was performed. Each track was added to the secondary vertex, and if the result passed cuts similar to, but looser than, the four-prong requirements, the event was kept. The D candidates from converted three-prong vertices, referred to as Seed 3 candidates, are typically events in which the χ^2 of the secondary vertex fit is poor and/or the likelihood that the extra track came from the primary is good (although not good enough to be included in the primary vertex). The D candidates from four-prong vertices are referred to as Seed 4 candidates. In this analysis, the Seed 3 candidates account for $\sim$1/3 of the total $K\pi\pi\pi$ candidates with somewhat worse signal-to-background than the Seed 4 candidates.

The $K\pi$ and $K\pi\pi\pi$ samples were each passed through another program from which "ntuples" were generated. The ntuples contain information about every event including physics variables such as x_F, p_T^2 and lifetime as well as cut variables, described

below. The first use of this ntuple is to obtain the best set of final selection criteria. Generally, selection criteria, or cuts, are requirements made of an event to help select signal and reject background. The optimal set of cuts is one in which the relative error of the final answer is minimized. Since the final answer is usually obtained by counting events, the relative error of the total number of candidates is a good indication of the relative error of the final answer. Minimizing the relative error on the total number of candidates is the same as maximizing the significance, defined as $S/\delta S$ where S is the measured signal and δS is the error on the signal. The error on the signal can be approximated by $\sqrt{S+B}$ where B is the background underneath the signal. This approximation is most valid when the signal is large, the background is small and the background is well fit by a functional form. In this case the error on the background measurement is negligible and the error on the signal comes from counting the entries in the signal region. The number of entries in the signal region is $S+B$ and the error on counting the entries is $\sim\sqrt{S+B}$.

Maximizing the significance of the signal generally leads to the smallest statistical error on the final answer. However, if systematic errors are important, then the cuts should also be chosen to minimize the systematic errors. One source of systematic error in this anlaysis comes from disagreement between the real data and the data generated from the Monte Carlo simulation program. The Monte Carlo program is designed to produce charm events and model their interactions in the various detectors of the spectrometer. Using the Monte Carlo program to measure the acceptance allows one to correct the data for events lost due to geometry, inefficiencies in the detector, inefficiencies in the reconstruction algorithm and events excluded by the applied cuts. If a cut variable distribution is different for data signal and Monte Carlo signal, then a cut on that variable will result in an incorrectly calculated acceptance. This type of

systematic error can be minimized by avoiding cuts where the Monte Carlo and data do not agree. Obviously this is not entirely possible because the data sample one uses already has cuts applied to it.

The final set of cuts were obtained by maximizing $S/\sqrt{S+B}$ for the $K\pi$, Seed 3 $K\pi\pi\pi$ and Seed 4 $K\pi\pi\pi$ event samples using variables where the agreement between Monte Carlo and data was good. This was done in the following way. For each cut variable, a data signal, a Monte Carlo signal, and a background distribution were generated. Events in the signal region are events where the reconstructed mass is ± 2 sigma around the mean value. The mean value and sigma are the measured D mass and width respectively. Events in the background (or "sideband") region are events where the reconstructed mass is greater than 4 sigma away from the mean value and less than 8 sigma away from the mean value. The background distribution for a cut variable is obtained by taking events in the background region. The signal plus background distribution is obtained by taking events in the signal region. The signal distribution is the signal plus background distribution (from the signal region) minus 1/2 of the background distribution (from the background region). The factor of 1/2 is needed because the background region is a total of 8 sigma wide while the signal region is only 4 sigma wide. The Monte Carlo signal distribution is obtained in exactly the same way using the Monte Carlo data. The differences in mass and width between the Monte Carlo and data require using slightly different signal and background regions. The Monte Carlo signal distribution is scaled to contain the same number of events as the data signal distribution. First the data signal and Monte Carlo signal distributions are compared to be sure they are in relatively good agreement. Next the value of $S/\sqrt{S+B}$ is calculated as a function of the cut variable. The signal is taken from the Monte Carlo and the background from the data. The higher statistics

Monte Carlo signal is used to avoid tuning the cuts to fluctuations in the data. Then the cut variable which gives the highest value of $S/\sqrt{S+B}$ is chosen. The cut value is usually chosen to be slightly looser than the point at which $S/\sqrt{S+B}$ is a maximum in order to compensate for the predilection of the Monte Carlo to be more optimistic than the data. This cut is then applied and the whole process is repeated for the next cut. For each x_F range, there were approximately 5(12) iterations for the $K\pi$ ($K\pi\pi\pi$) mode.

3.3.2 Final cuts

The cut variables used in this analysis and the reason the cut is used are:

SDZ The separation between the primary vertex and the secondary vertex in the beam (z) direction divided by the uncertainty on the separation. This requires a detached vertex which is the most important criterion in fixed-target charm physics.

PTB P_T (in GeV/c) of the D candidate relative to the primary-secondary line-of-flight to ensure that the D candidate comes from the primary.

DIP Distance (in microns) between the reconstructed D momentum vector and the primary at the z position of the primary to ensure that the D candidate comes from the primary.

PISO Minimum separation of all the decay tracks from the primary vertex (in microns) to ensure the decay products do not come from the primary.

TAU proper lifetime of the D candidate in picoseconds. Long lifetime events can come from secondary interactions or misreconstructed D^+ decays.

PT2DK Σp_T^2 of the tracks in the secondary vertex relative to the D candidate momentum in $\mathrm{GeV}^2/\mathrm{c}^2$. This cut is used to pick out events containing high-mass decays which generally have high relative p_T tracks compared to background events.

COSTHET Cosine of the angle between the K momentum and the D-candidate momentum in the D-candidate rest frame. This is similar to PT2DK in that it removes decays with collinear tracks.

JCAT Minimum JCATSG of tracks in the secondary vertex. The track category, JCATSG, is defined as $(2^0 r1 + 2^1 r2 + 2^2 r3 + 2^3 r4)$ where rN is 1 if the track uses hits in region N and 0 otherwise. Region 1 is upstream of the first magnet (silicon, PWC's and D1), Region 2 is between the two magnets (D2), Region 3 is immediately downstream of the second magnet (D3), and Region 4 is just before the calorimeters (D4). All tracks in this analysis are category 3, 7 and 15 tracks which are reconstructed in the silicon and make it through at least one magnet.

MXXIS Maximum χ^2/dof of the tracks in the secondary vertex. This reduces the number of "ghost" tracks.

SIGMA Miniumum distance between the secondary vertex and any solid material divided by the uncertainty on the distance. This cut is used to avoid vertices due to secondary interactions in material.

CHIVTX χ^2/dof for the fit of the decay tracks to a common vertex.

ZPRIM Z position of the primary vertex in cm. This cut is used to eliminate interactions in the interaction counter and vertex silicon planes.

MXRAT Maximum ratio of each secondary track's secondary vertex miss distance to primary vertex miss distance. This is used to make sure the decay tracks are more likely to have originated in the secondary vertex than in the primary vertex.

P(X) Momentum of particle X in GeV/c.

Examples of the type of plots used to optimize the signal for these cut variables are shown in Fig. 3.3 for the $K\pi$ signal, Fig. 3.4 for the $K\pi\pi\pi$ Seed 4 signal and Fig. 3.5 for the $K\pi\pi\pi$ Seed 3 signal. The first and third columns show a comparison of data signal, MC signal and data background for each variable. The second and fourth columns show the significance ($S/\sqrt{S+B}$) as a function of the appropriate variable. For the iteration shown in the figures, the set of cuts are approximately midway between the microstrip set and the final set. It is clear that, in all cases, the DIP variable needs to be tightened from its current 0.008 value, and for the $K\pi\pi\pi$ case (especially Seed 3), the SIGMA variable will be important. The agreement between Monte Carlo and data is fairly good for most of these variables. Exceptions are generally variables which were used in the microstrip or previous analysis stages for which there is no recourse (e.g. SDZ and PTB) and/or for which only loose cuts are applied which will have little effect on the final result (e.g. DIP and PTB). Other cut variables were investigated but they either did not increase the significance or were not well modeled by the Monte Carlo, or both. Notably missing from this list are any Čerenkov cut variables. It has been found that the Čerenkov modeling by the Monte Carlo is not very good. Although it is possible to calculate Čerenkov efficiencies using data, the error would be of the same order as the actual measurement. Therefore, to avoid the extra error and complication, there is no Čerenkov information used in this analysis. This means that a real two-prong D^0 candidate will often show up as

a fake $\overline{D}^0$ candidate and a real four-prong D^0 candidate will often appear twice as a fake $\overline{D}^0$ candidate and once as a fake D^0 candidate. Because the fake D candidates have two misidentified decay products, the background formed from them peaks near the correct mass but is much, much broader than the signal and will be accounted for by the background function in the fits to the mass distribution. To demonstrate the difference in the distributions, the same Monte Carlo candidates are plotted with the correct and incorrect mass assignments for both decay modes in Fig 3.6

Different reconstruction errors dominate in different regions of x_F. For instance, at low x_F (momentum), multiple Coulomb scattering is important for track and invariant mass reconstruction while at high x_F (momentum) the intrinsic measurement uncertainties dominate. Therefore, cut optimization was performed separately for different regions of x_F. This had little effect on the cut values chosen for the $K\pi$ mode. For the $K\pi\pi\pi$ mode, however, the optimization yielded different sets of cuts for the different x_F regions. In addition, the $K\pi\pi\pi$ cuts were optimized separately for Seed 3 and Seed 4 events. The final cut values for the $K\pi$ candidates are given in Table 3.2. The final cut values for the $K\pi\pi\pi$ candidates are given in Table 3.3 and Table 3.4 for Seed 4 and Seed 3 candidates, respectively.

In order to limit systematic errors, additional restrictions were also placed on the data. All events with a primary vertex consistent with being inside the platinum target ($Z_{prim} < -7.4$ cm) were discarded. It was found that interactions in the platinum target could result in back-splash into the halo counter 8 cm behind it, vetoing the event. In fact, since charm production is a hard process, charm events were vetoed more frequently than non-charm events. This effect does not appear in any other target, probably due to shielding by the (larger) platinum target. While there was enough calibration data to detect the effect, the statistics were too poor to correct for it, and

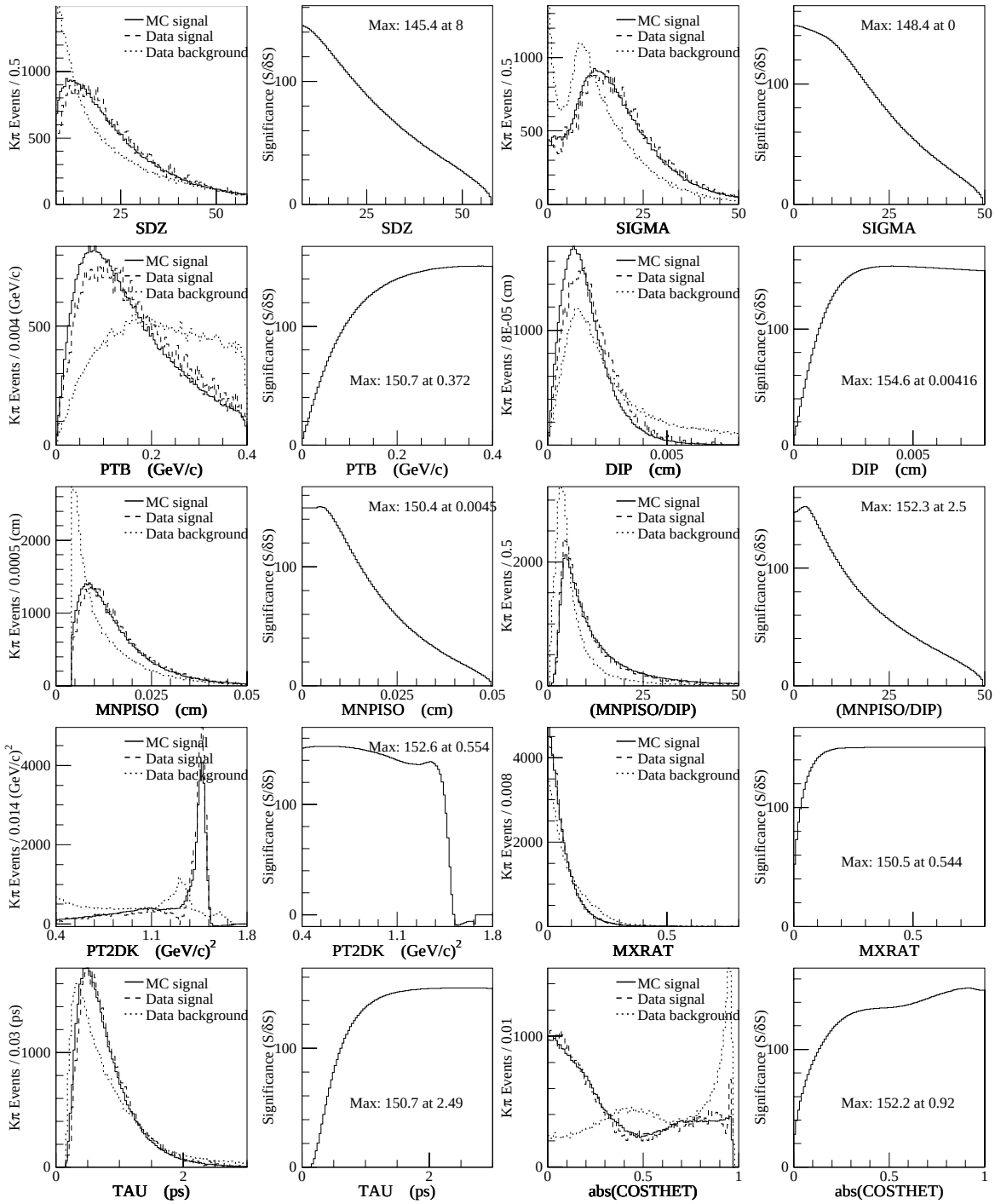

Fig. 3.3.— The first and third columns show a comparison of $K\pi$ Monte Carlo signal (solid), data signal (dashed) and data background (dotted) for cut variables used in this analysis. The second and fourth columns show the effect on $S/\sqrt{S+B}$ as the cut variables change. This sample contains data from all x_F with cuts approximately midway between the microstrip cuts and the final cuts.

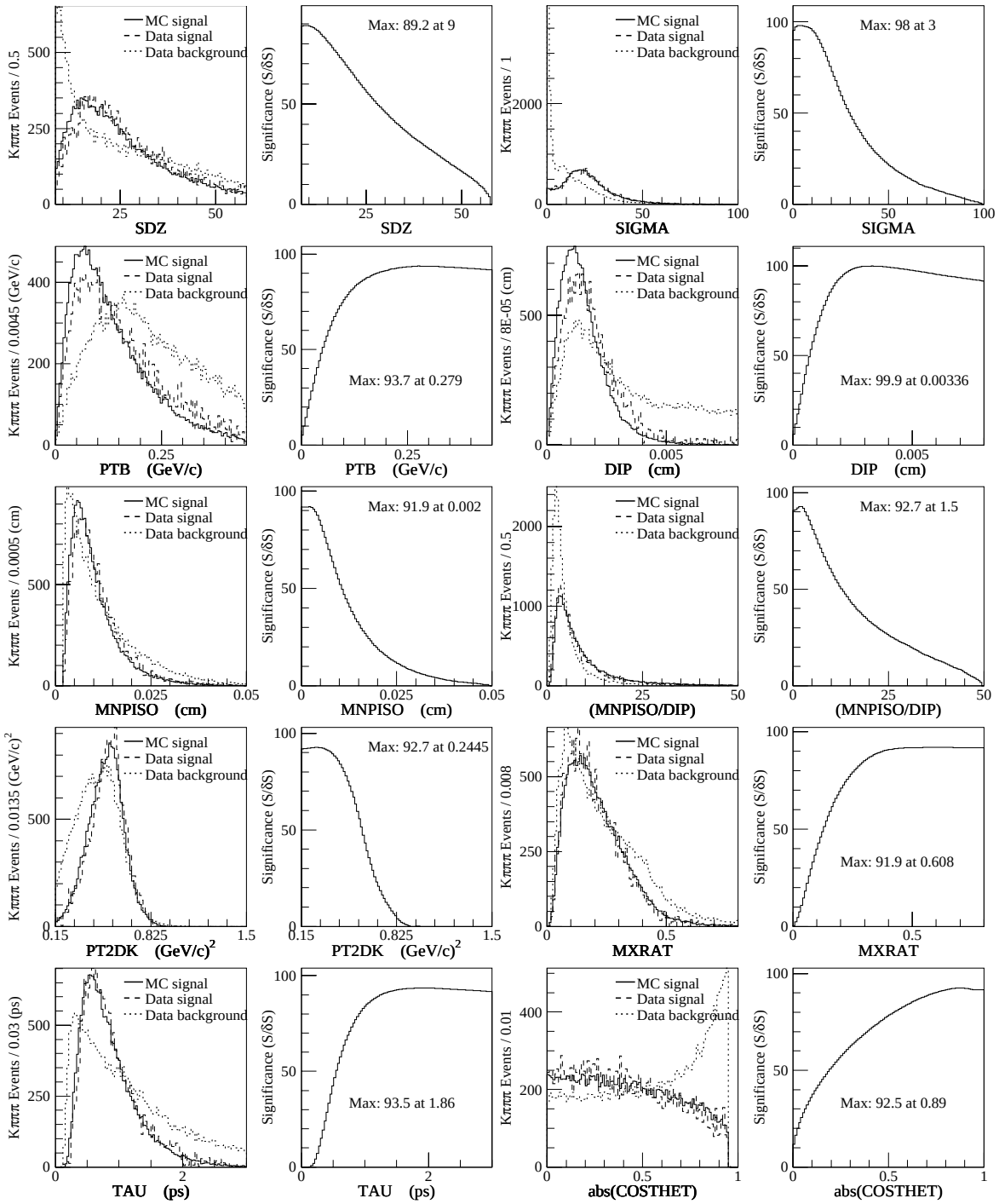

Fig. 3.4.— The first and third columns show a comparison of Seed 4 $K\pi\pi\pi$ Monte Carlo signal (solid), data signal (dashed) and data background (dotted) for cut variables used in this analysis. The second and fourth columns show the effect on $S/\sqrt{S+B}$ as the cut variables change. This sample contains data from all x_F with cuts approximately midway between the microstrip cuts and the final cuts.

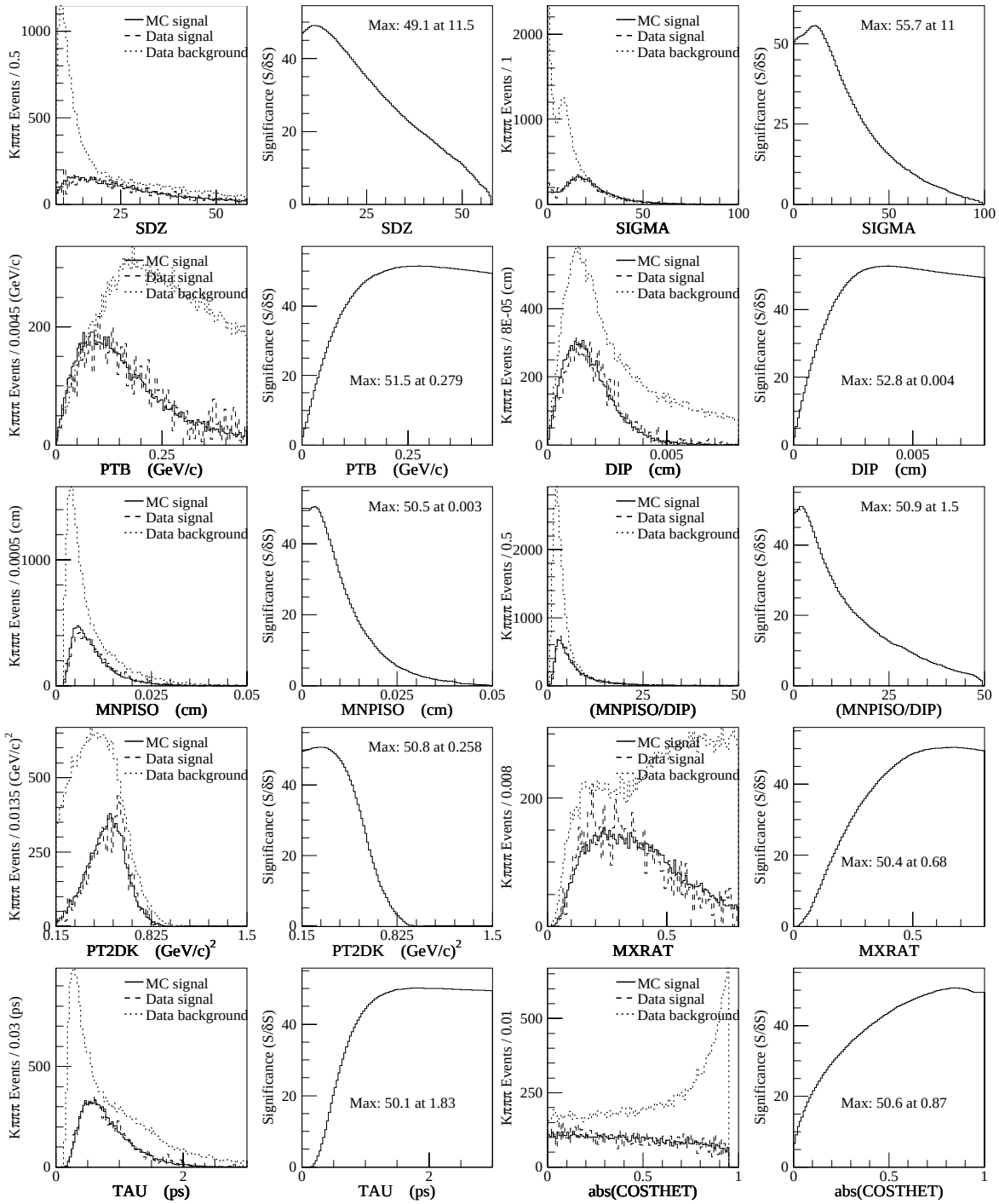

Fig. 3.5.— The first and third columns show a comparison of Seed 3 $K\pi\pi\pi$ Monte Carlo signal (solid), data signal (dashed) and data background (dotted) for cut variables used in this analysis. The second and fourth columns show the effect on $S/\sqrt{S+B}$ as the cut variables change. This sample contains data from all x_F with cuts approximately midway between the microstrip cuts and the final cuts.

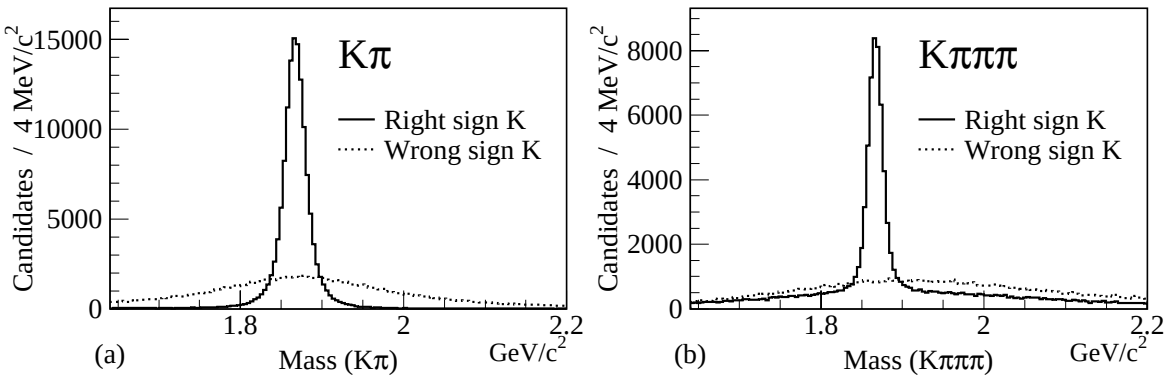

Fig. 3.6.— Monte Carlo $K\pi$ (a) and $K\pi\pi\pi$ (b) invariant mass plots with the correct (solid line) and incorrect (dotted line) sign of the K. For the $K\pi\pi\pi$ case, a correctly signed K still allows a two-fold ambiguity which explains the background in the solid histogram.

Cut	Sign	$x_F < 0.2$	$x_F > 0.2$	μstrip cut
Mass	>	1.625 GeV/c^2		1.70 GeV/c^2 [a]
SDZ	>	8		8
PTB	<	0.40 GeV/c		0.40 GeV/c
DIP	<	60 μm		
PISO	>	40 μm		
PISO/DIP	>	2.25		
SIGMA	>	0		
PT2DK	>	0.4 GeV^2/c^2		
TAU	<	3 ps		5 ps
|COS(θ)|	<	0.99		0.995
MXXIS	<	5		5[b]
ZPRIM	<	-0.35 cm		-1.00 cm
P(K),P(π)	>	2 GeV/c		2 GeV/c
JCAT	=	3,7,15	7,15	3,7,15

Table 3.2: Final cuts for $K\pi$ candidates. The μstrip column show the microstrip level cuts.

[a] Mass of KK

[b] Release 5 cut = 6.5, Release 7 cut = 5.0

Variable	Sign	$-.2 < x_F < 0$	$0 < x_F < .2$	$.2 < x_F < .8$	μstrip($K\pi\pi\pi$)
Mass	>	1.625 GeV/c^2			1.70 GeV/c^2 [a]
SDZ	>	9		10	7
PTB	<	0.4 GeV/c	0.45 GeV/c		0.45 GeV/c
DIP	<	50 μm		35 μm	120 μm
PISO	>	20 μm	30 μm		
SIGMA	>	8	2	0	
PT2DK	>	0.15 GeV^2/c^2			
TAU	<	3 ps			4 ps
|COS(θ)|	<	0.93		0.95	
MXXIS	<	5			5[b]
CHIVTX	<	25			$\approx$ 12[c]
ZPRIM	<	-0.35 cm			-1.00 cm
MXRAT	<	0.7			$\approx$ 1[d]
P(K)	>	2 GeV/c			2 GeV/c
P(π)	>	2 GeV/c			2 GeV/c

Table 3.3: Final cuts for Seed 4 $K\pi\pi\pi$ candidates. The μstrip column shows the microstrip level cuts.

[a] Mass of $KK\pi\pi$

[b] Release 5 cut = 6.5, Release 7 cut = 5.0

[c] While there is no explicit cut on this variable, there is a related cut applied which limits the χ^2 contribution from an individual track in the vertex.

[d] While there is no explicit cut on this variable, there are related cuts applied. One cut limits the χ^2 contribution from an individual track in the vertex. Another cut requires a track in the secondary vertex to give a large χ^2 contribution when added to the primary vertex.

Variable	Sign	$-.2 < x_F < 0$	$0 < x_F < .2$	$.2 < x_F < .8$	μstrip($K\pi\pi$)
Mass	>	1.625 GeV/c^2			1.70 GeV/c^2 [a]
SDZ	>	9	11		8
PTB	<	0.35 GeV/c	0.45 GeV/c	0.40 GeV/c	0.35 GeV/c
DIP	<	50 μm	45 μm	40 μm	100 μm
PISO	>	30 μm			
SIGMA	>	8	2	0	
PT2DK	>	0.15 GeV^2/c^2			
TAU	<	3 ps			5 ps
|COS(θ)|	<	0.93		0.95	
MXXIS	<	5			5[b]
CHIVTX	<	25			$\approx$ 12[c]
ZPRIM	<	-0.35 cm			-1.00 cm
MXRAT	<	0.7			$\approx$ 1[d]
P(K)	>	2 GeV/c			2 GeV/c
P(π)	>	2 GeV/c			2 GeV/c

Table 3.4: Final cuts for Seed 3 $K\pi\pi\pi$ candidates. The μstrip column shows the microstrip level cuts for three prong decays.

[a] Mass of $KK\pi$

[b] Release 5 cut = 6.5, Release 7 cut = 5.0

[c] While there is no explicit cut on this variable, there is a related cut applied which limits the χ^2 contribution from an individual track in the vertex.

[d] While there is no explicit cut on this variable, there are related cuts applied. One cut limits the χ^2 contribution from an individual track in the vertex. Another cut requires a track in the secondary vertex to give a large χ^2 contribution when added to the primary vertex.

thus the platinum target events were discarded. The first 5% of the data taken by E791 was with a four-target configuration, without one of the diamond planes. Some of the reconstruction routines did not handle the old target configuration correctly. In addition, the Monte Carlo was run and vetted with the new configuration. Therefore all of the four-target runs were also discarded. The remaining data are used to measure quantities such as the masses and widths of the D candidates and are referred to as Sample A. The data used for analysis required some more restrictions, however. Approximately 2% of the remaining data were found to have some problems including readout errors, pedestal errors, large inefficiencies, magnet setting errors, trigger setting errors, etc. These runs were discarded. The runs taken with only an interaction trigger (no E_T requirement) were also discarded. This eliminates an additional 5% of the data. Proper normalization of the distributions requires information from the scalers, described in Section 2.5. These scalers were read out once per spill during a run, independent of the data acquisition system. Approximately 3/4 of the way through the data taking it was discovered that the full initialization of all detectors in the middle of a run caused the scaler data acquisition to overwrite the old scaler data for that run with new data starting from the initialization. Fortunately this full initialization was not performed frequently and only ~5% of the data are without proper scaler information. The remaining Release 5 and Release 7 data, called Sample B, are shown in Figures 3.7 and 3.8. The yields for the various samples are shown in Table 3.5. The fits use a single Gaussian for the signal and a cubic (quadratic) polynomial for the $K\pi$ ($K\pi\pi\pi$) background.

Data Set	$K\pi$ Yield		$K\pi\pi\pi$ Yield	
	Release 5	Release 7	Release 5	Release 7
Full Sample	57372 ± 414	22086 ± 267	32144 ± 287	14247 ± 196
Sample A	46685 ± 375	15519 ± 220	26641 ± 261	10354 ± 165
Sample B	39800 ± 344	12447 ± 196	22667 ± 241	8375 ± 148

Table 3.5: Release 5 and Release 7 $K\pi$ and $K\pi\pi\pi$ yields from different data samples. Full sample includes all E791 data; Sample A requires no four-target runs and no primary interaction in the platinum target; Sample B also requires no poor quality runs, no interaction trigger runs and no runs with missing or inaccurate scaler data.

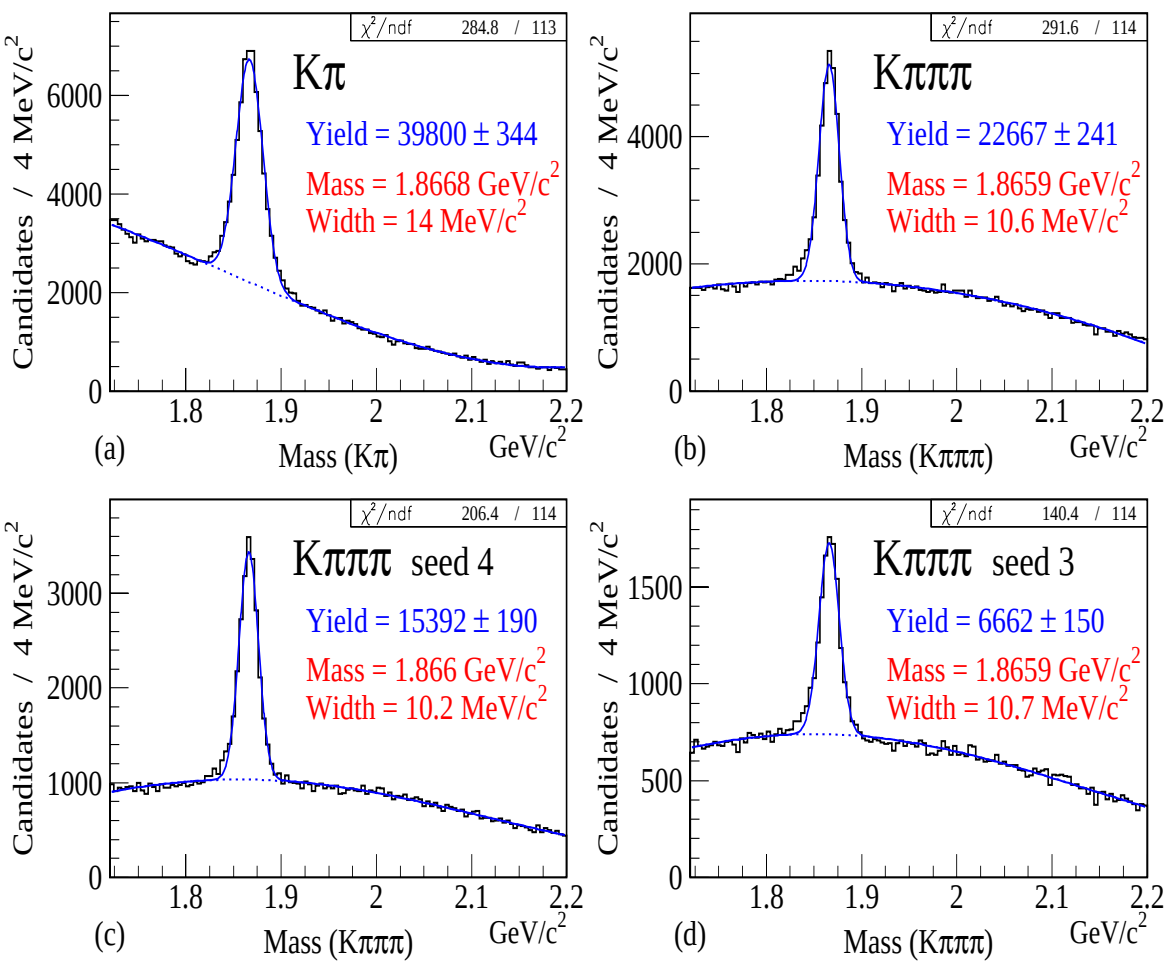

Fig. 3.7.— Sample B $K\pi$ (a) and $K\pi\pi\pi$ (b) yields from the Release 5 E791 data with the nominal cuts used in this anlaysis plus no four-target runs, no interaction trigger runs, no poor quality runs, no runs with missing or inaccurate scaler data and no events with an interaction in the platinum target. The $K\pi\pi\pi$ sample is also shown separated into Seed 4 (c) and Seed 3 events (d).

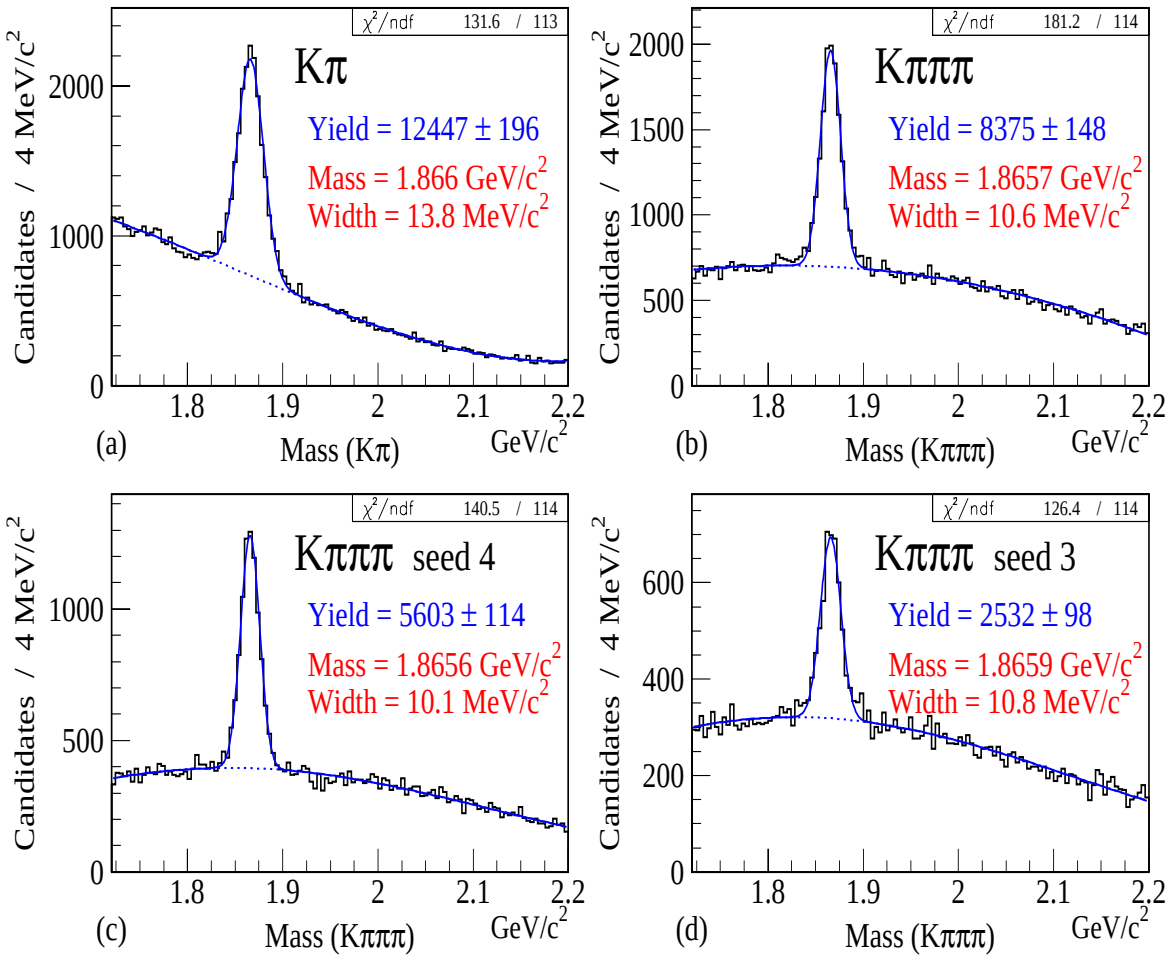

Fig. 3.8.— Sample B $K\pi$ (a) and $K\pi\pi\pi$ (b) yields from the Release 7 E791 data with the nominal cuts used in this anlaysis plus no four-target runs, no interaction trigger runs, no poor quality runs, no runs with missing or inaccurate scaler data and no events with an interaction in the platinum target. The $K\pi\pi\pi$ sample is also shown separated into Seed 4 (c) and Seed 3 events (d).

Chapter 4

Data

To obtain the x_F and p_T^2 distributions we need a method to determine the amount of signal and a means to correct for the amount of signal missed. The first issue is addressed here.

4.1 Calculating Yields

Generally, the amount of signal is obtained by fitting a function to the mass distribution. The function consists of one part which represents signal and one part which represents background. The mass resolution of the spectrometer is much larger than the intrinsic width of the D^0 mass state. Therefore, a Gaussian, rather than a Breit-Wigner, is chosen to represent the signal. The background function can be anything which adequately models the background. In this analysis, first, second, and third degree polynomials, exponentials and Gaussians are used to model the background. The calculated yields obtained by fitting the mass plots shown in Figures 3.7 and 3.8 are only approximations to the true number of reconstructed candidates. One major failing of this approximation comes from the assumption that the signal can be represented by a single Gaussian with one central value and one width. Imperfect

knowledge of the E791 spectrometer magnetic field and geometry has already been shown to produce a mass shift correlated with x_F, as shown in Fig. 3.1. Figure 3.1 also demonstrates the mass resolution (width) dependence on x_F. In fact, each D candidate has a different mass resolution which depends upon the measurement errors associated with the decay tracks. The mass resolution can be calculated by differentiating the invariant mass formula. To evaluate the resulting expression requires knowing the momentum error, the x slope error, the y slope error and all of their correlations for each track as well as correlations between the decay tracks. The track errors come mainly from two sources. The fractional momentum error due to multiple Coulomb scattering is constant and dominates at low momentum. Intrinsic measurement errors due to the resolution of the detectors dominate at higher momenta since the fractional momentum error from this contribution is proportional to momentum. For category 7 and 15 tracks, where the track passes through both magnets, the momentum resolution is $\delta p/p \approx 0.6\% \oplus (0.02p)\%$ where $\oplus$ indicates a quadratic sum and p is in GeV/c. Category 3 tracks, which pass through only the first magnet, have a resolution $\delta p/p \approx 2\% \oplus (0.1p)\%$. Other effects such as incorrect geometry and/or magnetic fields can also affect the momentum resolution. The measured D mass depends also on correlations between the decay tracks, primarily the opening angle between the tracks. The mass width is most sensitive to the number of decay tracks (actually the Q-value — amount of energy available in a decay), the percentage of category 3 decay tracks, and the D^0 x_F value. The $K\pi\pi\pi$ width is 25% smaller than the $K\pi$ width. The mass width dependence on x_F (at low x_F) is closely connected with the dependence on the number of category 3 decay tracks. Since category 3 tracks are generally low momentum tracks, category 3 decay tracks usually come from low momentum (x_F) D candidates, especially for two-body decays. The mass width dependence on x_F as seen

in Fig. 3.1 comes from two sources. The increase at low x_F is due to an increasing fraction of events with category 3 decay tracks. The increase at high x_F is due to intrinsic detector resolution. The momentum resolution decreases as the momentum (x_F) increases and the opening angle measurement resolution also decreases as the opening angle decreases (x_F increases). The resolution variation versus x_F can be up to a factor of four or more as shown in Fig. 3.1. The mass and width values for the $K\pi$ and $K\pi\pi\pi$ candidates are summarized in Table 4.1 and Table 4.2 respectively. These were obtained from Sample A by fitting a Gaussian for the signal. The $K\pi$ background is fit with a third-degree polynomial except for the first bin and the last two bins in x_F which are fit with an exponential background. The $K\pi\pi\pi$ background is fit with a quadratic function. The measured masses and widths for Monte Carlo data are found in Table 4.3 and Table 4.4 for $K\pi$ and $K\pi\pi\pi$ respectively. The Monte Carlo $K\pi$ ($K\pi\pi\pi$) data are fit with a Gaussian signal and a linear (quadratic) background. The mass and width dependence on p_T^2 is minimal in both data and Monte Carlo.

4.2 Using Normalized Mass

One way to compensate for the broadening of the mass peak that results from combining events from different kinematic regions, which have different central values for the mass as well as different mass resolutions, is to convert to the normalized mass. The normalized mass of a $D^0 \to K\pi$ candidate is:

$$m_n = \frac{m_{K\pi} - m_{D^0}}{\sigma_{K\pi}} \tag{4.1}$$

where $m_{K\pi}$ is the measured mass of the candidate, m_{D^0} is the average mass of the D^0 candidates and $\sigma_{K\pi}$ is the mass resolution of the candidate. In this analysis, the average mass (m_{D^0}) is measured by fitting a Gaussian to the signal of interest. This

x_F Range	Release 5		Release 7	
	Mass (GeV/c^2)	Width (MeV/c^2)	Mass (GeV/c^2)	Width (MeV/c^2)
-0.125 $< x_F <$ -0.100	1.8606 ± 0.0111	42.0 ± 13.5	1.9050 ± 0.0198	64.3 ± 15.8
-0.100 $< x_F <$ -0.075	1.8567 ± 0.0035	31.1 ± 4.1	1.8683 ± 0.0018	7.6 ± 2.2
-0.075 $< x_F <$ -0.050	1.8618 ± 0.0012	18.4 ± 1.3	1.8678 ± 0.0014	16.4 ± 1.4
-0.050 $< x_F <$ -0.025	1.8651 ± 0.0006	15.5 ± 0.7	1.8673 ± 0.0008	13.1 ± 1.0
-0.025 $< x_F <$ 0.000	1.8659 ± 0.0004	12.9 ± 0.4	1.8662 ± 0.0005	10.8 ± 0.6
0.000 $< x_F <$ 0.025	1.8658 ± 0.0003	12.6 ± 0.3	1.8658 ± 0.0004	10.9 ± 0.4
0.025 $< x_F <$ 0.050	1.8664 ± 0.0003	11.4 ± 0.3	1.8663 ± 0.0004	11.0 ± 0.4
0.050 $< x_F <$ 0.075	1.8667 ± 0.0003	11.6 ± 0.3	1.8654 ± 0.0004	11.3 ± 0.4
0.075 $< x_F <$ 0.100	1.8669 ± 0.0003	12.6 ± 0.3	1.8660 ± 0.0005	12.9 ± 0.5
0.100 $< x_F <$ 0.125	1.8674 ± 0.0003	13.7 ± 0.3	1.8656 ± 0.0006	14.6 ± 0.6
0.125 $< x_F <$ 0.150	1.8683 ± 0.0004	13.9 ± 0.4	1.8655 ± 0.0007	15.9 ± 0.8
0.150 $< x_F <$ 0.175	1.8678 ± 0.0005	16.2 ± 0.5	1.8653 ± 0.0009	16.9 ± 0.9
0.175 $< x_F <$ 0.200	1.8685 ± 0.0006	17.2 ± 0.6	1.8679 ± 0.0009	16.4 ± 1.0
0.200 $< x_F <$ 0.250	1.8681 ± 0.0005	18.3 ± 0.6	1.8661 ± 0.0010	21.3 ± 1.2
0.250 $< x_F <$ 0.300	1.8707 ± 0.0009	24.1 ± 1.0	1.8676 ± 0.0014	24.2 ± 1.6
0.300 $< x_F <$ 0.350	1.8714 ± 0.0014	30.6 ± 1.7	1.8674 ± 0.0021	30.7 ± 2.4
0.350 $< x_F <$ 0.400	1.8733 ± 0.0019	29.3 ± 2.3	1.8662 ± 0.0034	39.3 ± 4.5
0.400 $< x_F <$ 0.500	1.8748 ± 0.0030	51.3 ± 4.8	1.8672 ± 0.0037	33.8 ± 4.5
0.500 $< x_F <$ 0.600	1.8734 ± 0.0069	64.6 ± 8.9	1.8821 ± 0.0067	49.7 ± 9.1
0.600 $< x_F <$ 0.800	1.8631 ± 0.0085	66.0 ± 12.0	1.8861 ± 0.0096	64.0 ± 13.2

Table 4.1: $K\pi$ measured mass and width in bins of x_F for Release 5 and Release 7 data.

x_F Range	Release 5		Release 7	
	Mass (GeV/c^2)	Width (MeV/c^2)	Mass (GeV/c^2)	Width (MeV/c^2)
-0.125 $< x_F <$ -0.100	1.8637 ± 0.0063	13.8 ± 4.9	1.8742 ± 0.0143	3.8 ± 9.6
-0.100 $< x_F <$ -0.075	1.8564 ± 0.0030	16.9 ± 2.6	1.8792 ± 0.0066	17.9 ± 5.5
-0.075 $< x_F <$ -0.050	1.8644 ± 0.0018	13.8 ± 1.8	1.8664 ± 0.0014	6.5 ± 1.5
-0.050 $< x_F <$ -0.025	1.8622 ± 0.0008	12.1 ± 0.8	1.8650 ± 0.0010	9.0 ± 0.9
-0.025 $< x_F <$ 0.000	1.8630 ± 0.0005	11.1 ± 0.5	1.8668 ± 0.0007	9.0 ± 0.7
0.000 $< x_F <$ 0.025	1.8648 ± 0.0003	9.9 ± 0.4	1.8657 ± 0.0005	8.5 ± 0.5
0.025 $< x_F <$ 0.050	1.8659 ± 0.0003	8.9 ± 0.3	1.8656 ± 0.0004	9.3 ± 0.5
0.050 $< x_F <$ 0.075	1.8659 ± 0.0003	9.3 ± 0.3	1.8656 ± 0.0004	9.6 ± 0.4
0.075 $< x_F <$ 0.100	1.8663 ± 0.0003	9.0 ± 0.3	1.8657 ± 0.0004	9.4 ± 0.4
0.100 $< x_F <$ 0.125	1.8664 ± 0.0003	9.9 ± 0.3	1.8654 ± 0.0005	10.3 ± 0.5
0.125 $< x_F <$ 0.150	1.8673 ± 0.0004	10.2 ± 0.4	1.8651 ± 0.0006	10.5 ± 0.6
0.150 $< x_F <$ 0.175	1.8658 ± 0.0005	12.3 ± 0.5	1.8660 ± 0.0007	11.6 ± 0.7
0.175 $< x_F <$ 0.200	1.8673 ± 0.0005	10.9 ± 0.5	1.8668 ± 0.0008	11.7 ± 0.9
0.200 $< x_F <$ 0.250	1.8672 ± 0.0005	12.8 ± 0.5	1.8653 ± 0.0007	12.4 ± 0.7
0.250 $< x_F <$ 0.300	1.8654 ± 0.0009	15.1 ± 1.0	1.8660 ± 0.0016	19.3 ± 2.1
0.300 $< x_F <$ 0.350	1.8682 ± 0.0014	16.1 ± 1.5	1.8689 ± 0.0019	16.8 ± 1.9
0.350 $< x_F <$ 0.400	1.8665 ± 0.0019	17.6 ± 1.8	1.8698 ± 0.0026	15.3 ± 2.6
0.400 $< x_F <$ 0.500	1.8660 ± 0.0025	19.9 ± 2.4	1.8692 ± 0.0051	28.2 ± 8.4
0.500 $< x_F <$ 0.600	1.8614 ± 0.0123	42.1 ± 15.4	1.8534 ± 0.0124	35.1 ± 15.9
0.600 $< x_F <$ 0.800	1.8739 ± 0.0084	32.9 ± 7.4	1.8672 ± 0.0100	20.3 ± 11.2

Table 4.2: $K\pi\pi\pi$ measured mass and width in bins of x_F for Release 5 and Release 7 data.

x_F Range	Release 5		Release 7	
	Mass (GeV/c^2)	Width (MeV/c^2)	Mass (GeV/c^2)	Width (MeV/c^2)
-0.125 $< x_F <$ -0.100	1.8601 ± 0.0010	27.8 ± 0.9	1.8661 ± 0.0007	19.4 ± 0.7
-0.100 $< x_F <$ -0.075	1.8597 ± 0.0005	25.2 ± 0.4	1.8644 ± 0.0003	16.7 ± 0.3
-0.075 $< x_F <$ -0.050	1.8633 ± 0.0002	21.6 ± 0.2	1.8651 ± 0.0002	14.9 ± 0.2
-0.050 $< x_F <$ -0.025	1.8641 ± 0.0001	17.1 ± 0.1	1.8650 ± 0.0001	12.6 ± 0.1
-0.025 $< x_F <$ 0.000	1.8650 ± 0.0001	13.9 ± 0.1	1.8651 ± 0.0001	11.1 ± 0.1
0.000 $< x_F <$ 0.025	1.8657 ± 0.0001	12.0 ± 0.1	1.8650 ± 0.0001	10.4 ± 0.1
0.025 $< x_F <$ 0.050	1.8663 ± 0.0001	11.3 ± 0.1	1.8649 ± 0.0001	10.3 ± 0.1
0.050 $< x_F <$ 0.075	1.8669 ± 0.0001	11.4 ± 0.1	1.8648 ± 0.0001	10.6 ± 0.1
0.075 $< x_F <$ 0.100	1.8675 ± 0.0001	12.0 ± 0.1	1.8649 ± 0.0001	11.4 ± 0.1
0.100 $< x_F <$ 0.125	1.8679 ± 0.0001	12.7 ± 0.1	1.8649 ± 0.0001	12.0 ± 0.1
0.125 $< x_F <$ 0.150	1.8682 ± 0.0001	13.7 ± 0.1	1.8649 ± 0.0001	13.0 ± 0.1
0.150 $< x_F <$ 0.175	1.8685 ± 0.0001	14.8 ± 0.1	1.8649 ± 0.0001	14.1 ± 0.1
0.175 $< x_F <$ 0.200	1.8687 ± 0.0001	16.3 ± 0.1	1.8650 ± 0.0001	15.1 ± 0.1
0.200 $< x_F <$ 0.250	1.8691 ± 0.0001	17.3 ± 0.1	1.8651 ± 0.0001	15.4 ± 0.1
0.250 $< x_F <$ 0.300	1.8695 ± 0.0001	20.7 ± 0.1	1.8653 ± 0.0001	18.0 ± 0.1
0.300 $< x_F <$ 0.350	1.8701 ± 0.0002	24.8 ± 0.2	1.8658 ± 0.0002	21.3 ± 0.1
0.350 $< x_F <$ 0.400	1.8702 ± 0.0003	28.5 ± 0.3	1.8660 ± 0.0002	24.6 ± 0.2
0.400 $< x_F <$ 0.500	1.8715 ± 0.0004	34.2 ± 0.3	1.8668 ± 0.0003	29.0 ± 0.3
0.500 $< x_F <$ 0.600	1.8731 ± 0.0008	43.5 ± 0.7	1.8689 ± 0.0006	37.4 ± 0.5
0.600 $< x_F <$ 0.800	1.8786 ± 0.0012	52.6 ± 1.1	1.8722 ± 0.0010	45.2 ± 0.9

Table 4.3: $K\pi$ measured mass and width in bins of x_F for Release 5 and Release 7 Monte Carlo data.

x_F Range	Release 5		Release 7	
	Mass	Width	Mass	Width
	(GeV/c^2)	(MeV/c^2)	(GeV/c^2)	(MeV/c^2)
-0.125 $< x_F <$ -0.100	1.8638 ± 0.0016	12.1 ± 1.6	1.8647 ± 0.0016	10.8 ± 1.4
-0.100 $< x_F <$ -0.075	1.8634 ± 0.0011	16.2 ± 1.0	1.8647 ± 0.0008	11.1 ± 0.7
-0.075 $< x_F <$ -0.050	1.8641 ± 0.0004	11.5 ± 0.3	1.8647 ± 0.0003	8.8 ± 0.3
-0.050 $< x_F <$ -0.025	1.8645 ± 0.0002	10.0 ± 0.2	1.8650 ± 0.0002	8.3 ± 0.1
-0.025 $< x_F <$ 0.000	1.8652 ± 0.0001	8.8 ± 0.1	1.8650 ± 0.0001	7.7 ± 0.1
0.000 $< x_F <$ 0.025	1.8658 ± 0.0001	8.4 ± 0.1	1.8651 ± 0.0001	7.4 ± 0.1
0.025 $< x_F <$ 0.050	1.8664 ± 0.0001	8.2 ± 0.1	1.8651 ± 0.0001	7.7 ± 0.1
0.050 $< x_F <$ 0.075	1.8668 ± 0.0001	8.2 ± 0.1	1.8650 ± 0.0001	7.9 ± 0.1
0.075 $< x_F <$ 0.100	1.8673 ± 0.0001	8.4 ± 0.1	1.8651 ± 0.0001	8.1 ± 0.1
0.100 $< x_F <$ 0.125	1.8677 ± 0.0001	8.7 ± 0.1	1.8650 ± 0.0001	8.4 ± 0.1
0.125 $< x_F <$ 0.150	1.8679 ± 0.0001	9.1 ± 0.1	1.8650 ± 0.0001	9.0 ± 0.1
0.150 $< x_F <$ 0.175	1.8678 ± 0.0001	9.5 ± 0.1	1.8649 ± 0.0001	9.6 ± 0.1
0.175 $< x_F <$ 0.200	1.8683 ± 0.0001	10.4 ± 0.1	1.8652 ± 0.0001	10.3 ± 0.1
0.200 $< x_F <$ 0.250	1.8683 ± 0.0001	11.2 ± 0.1	1.8651 ± 0.0001	11.0 ± 0.1
0.250 $< x_F <$ 0.300	1.8685 ± 0.0002	12.8 ± 0.2	1.8653 ± 0.0001	12.1 ± 0.1
0.300 $< x_F <$ 0.350	1.8686 ± 0.0003	15.0 ± 0.3	1.8654 ± 0.0002	14.0 ± 0.2
0.350 $< x_F <$ 0.400	1.8684 ± 0.0004	16.4 ± 0.5	1.8655 ± 0.0004	15.6 ± 0.4
0.400 $< x_F <$ 0.500	1.8704 ± 0.0006	19.6 ± 0.7	1.8668 ± 0.0005	18.6 ± 0.5
0.500 $< x_F <$ 0.600	1.8715 ± 0.0016	27.4 ± 1.8	1.8660 ± 0.0011	24.3 ± 1.2
0.600 $< x_F <$ 0.800	1.8766 ± 0.0035	35.0 ± 4.2	1.8666 ± 0.0020	26.2 ± 2.3

Table 4.4: $K\pi\pi\pi$ measured mass and width in bins of x_F for Release 5 and Release 7 Monte Carlo data.

allows the value of m_{D^0} to be different for different decay modes or bins of x_F, for example. The mass resolution is calculated for each event by determining the error on the invariant mass calculation. If the mass resolution is calculated correctly, the normalized mass distribution will be a unit Gaussian centered at zero for all signal events. As long as the background can still be well fit, the signal is easy to extract by fitting a single Gaussian.

Using normalized mass to extract yields has some disadvantages. The E791 Data Summary Tapes (DSTs) contain some information about the momentum errors of the downstream spectrometer and the slope errors of the silicon system. However, as mentioned in Section 3.1.3, the momentum errors were not properly stored for negatively charged tracks in the Release 5 code or for any tracks in the Release 7 code. In addition, the correlation between momentum error and slope error was not written out. This, along with imperfect knowledge of the geometry and magnetic fields of the E791 spectrometer, causes the calculated mass resolution to be just an approximation to the true value. The calculated mass resolution does a good job of accounting for momentum errors due to different track categories but it does not accurately account for the increase in mass width with increasing x_F. This makes the normalized mass very effective at low x_F where the number of category 3 tracks is larger and the mass width is reasonably stable. Another disadvantage of using normalized masses comes from the limited fit range. Since a cut has already been placed on the mass of the D candidate, extending the normalized mass range too far can result in distortions of the distribution which can create a false peak and/or an artificially low background. Since the mass of the D candidate is required to be between 1.625 and 2.200 GeV/c^2, the limits of the normalized mass distribution for a D^0 mass of 1.865 GeV/c^2 should be $(1.625 - 1.865)/\sigma^{max}$ and $(2.200 - 1.865)/\sigma^{max}$.

Although the $K\pi$ ($K\pi\pi\pi$) σ values extend to 0.2 GeV/c^2 (0.1 GeV/c^2), 99% of the candidates have σ less than 0.027 GeV/c^2 (0.019 GeV/c^2). Using the 99% values, the normalized mass histograms have limits of -9.0 to 12.5 and -12.5 to 17.5 for the $K\pi$ and $K\pi\pi\pi$ modes, respectively. The widest possible mass range is desired to allow the best possible measurement of the background. The average calculated resolution is 0.013 GeV/c^2 for $K\pi$ and 0.009 GeV/c^2 for $K\pi\pi\pi$. Assuming an approximately linear shape for the background, this implies less than half of the background events in the sample are plotted on the normalized mass plots, reducing the accuracy with which the background (and thus the background-subtracted signal) can be measured.

Figures 4.1 and 4.2 show the $K\pi$ fitted invariant mass plots versus x_F for Release 5 and Release 7 respectively, from which the values in Table 4.1 were obtained (Sample A). Figures 4.3 and 4.4 show the $K\pi$ fitted normalized mass plots versus x_F for the same sample for Release 5 and Release 7 respectively. The yields in these four figures (and similar plots for the Monte Carlo data) were used to calculate the ratios plotted in Fig. 4.5 which compares the yields obtained using invariant masses and normalized masses for $K\pi$ events as a function of x_F for data and Monte Carlo. The minimization and error analysis was performed using the MINUIT [30] software which is part of the CERN program library. The fits to the mass distributions are all performed using a binned maximum log-likelihood technique. In addition, errors are determined using the MINOS method in MINUIT which finds the points at which the function changes by 0.5 log-likelihood units rather than using the error matrix calculated at the minimum and assuming parabolic errors.

As mentioned above, the calculated resolution correctly accounts for category 3 tracks but not for the high x_F resolution degradation. Therefore, the biggest gain is at low x_F where there are the most category 3 tracks. $K\pi$ candidates with a

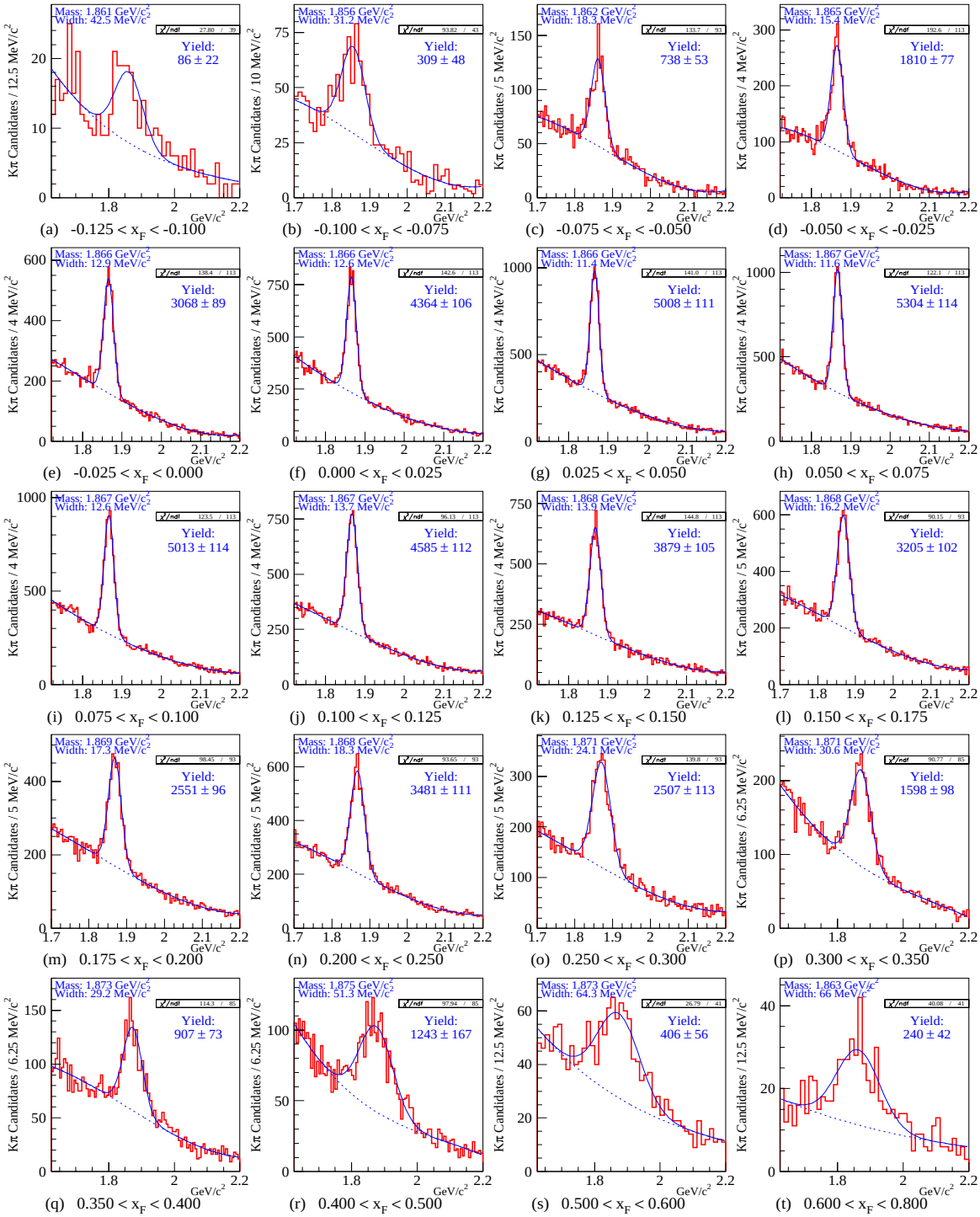

Fig. 4.1.— Sample A $K\pi$ invariant mass plots for 20 bins of x_F from the Release 5 E791 data with the nominal analysis cuts plus no events with an interaction in the Platinum target.

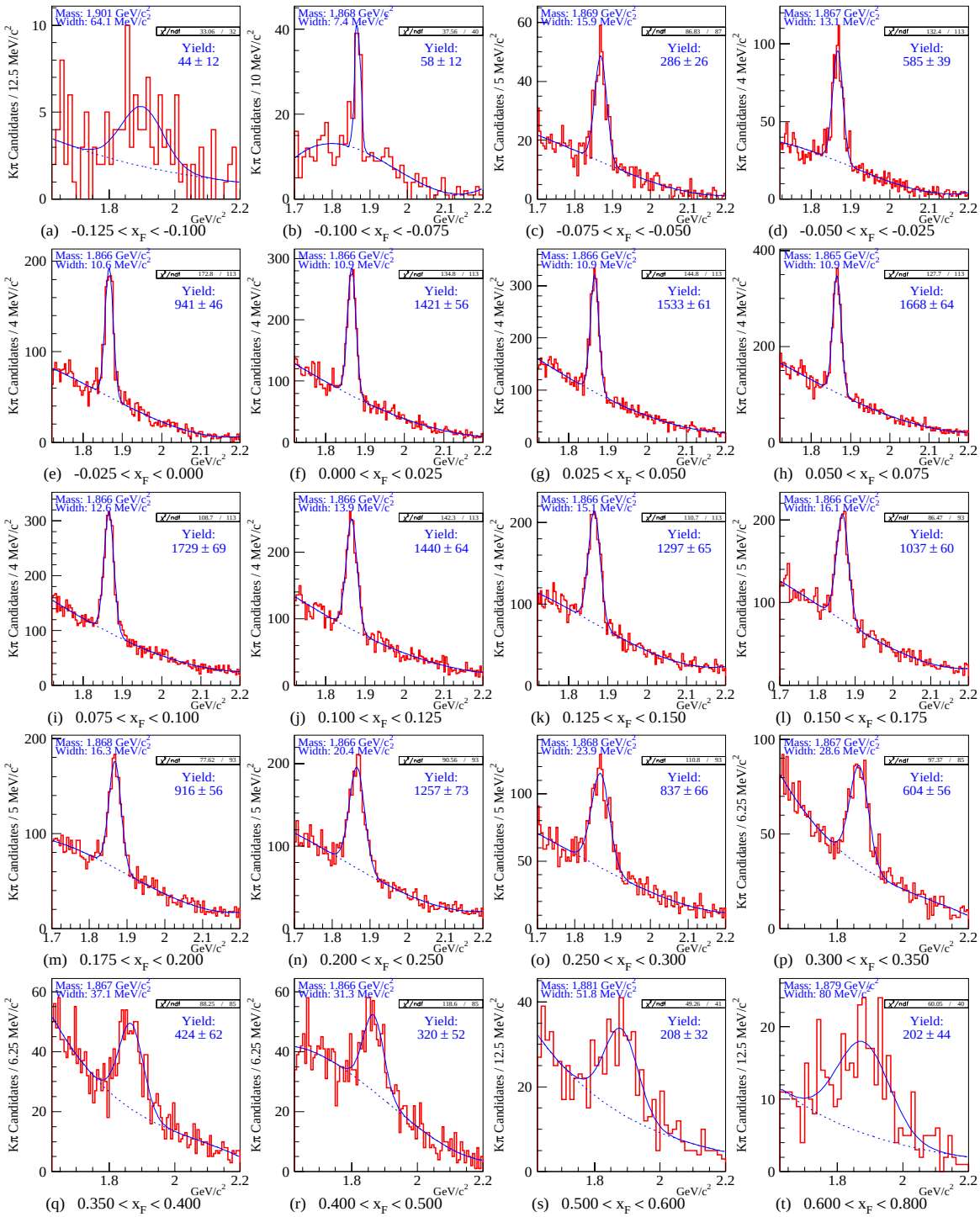

Fig. 4.2.— Sample A $K\pi$ invariant mass plots for 20 bins of x_F from the Release 7 E791 data with the nominal analysis cuts plus no events with an interaction in the Platinum target.

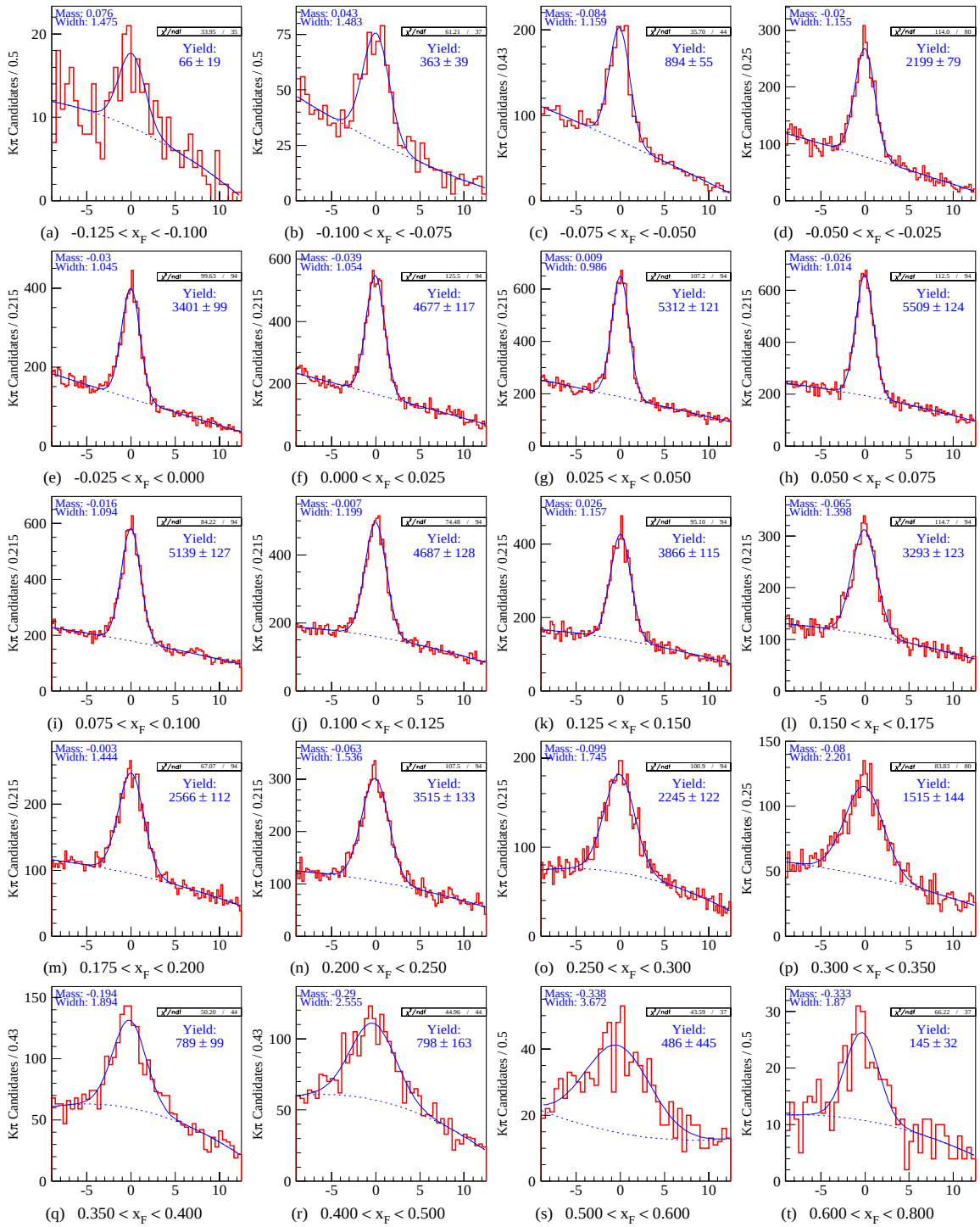

Fig. 4.3.— Sample A $K\pi$ normalized mass plots for 20 bins of x_F from the Release 5 E791 data with the nominal analysis cuts plus no events with an interaction in the Platinum target.

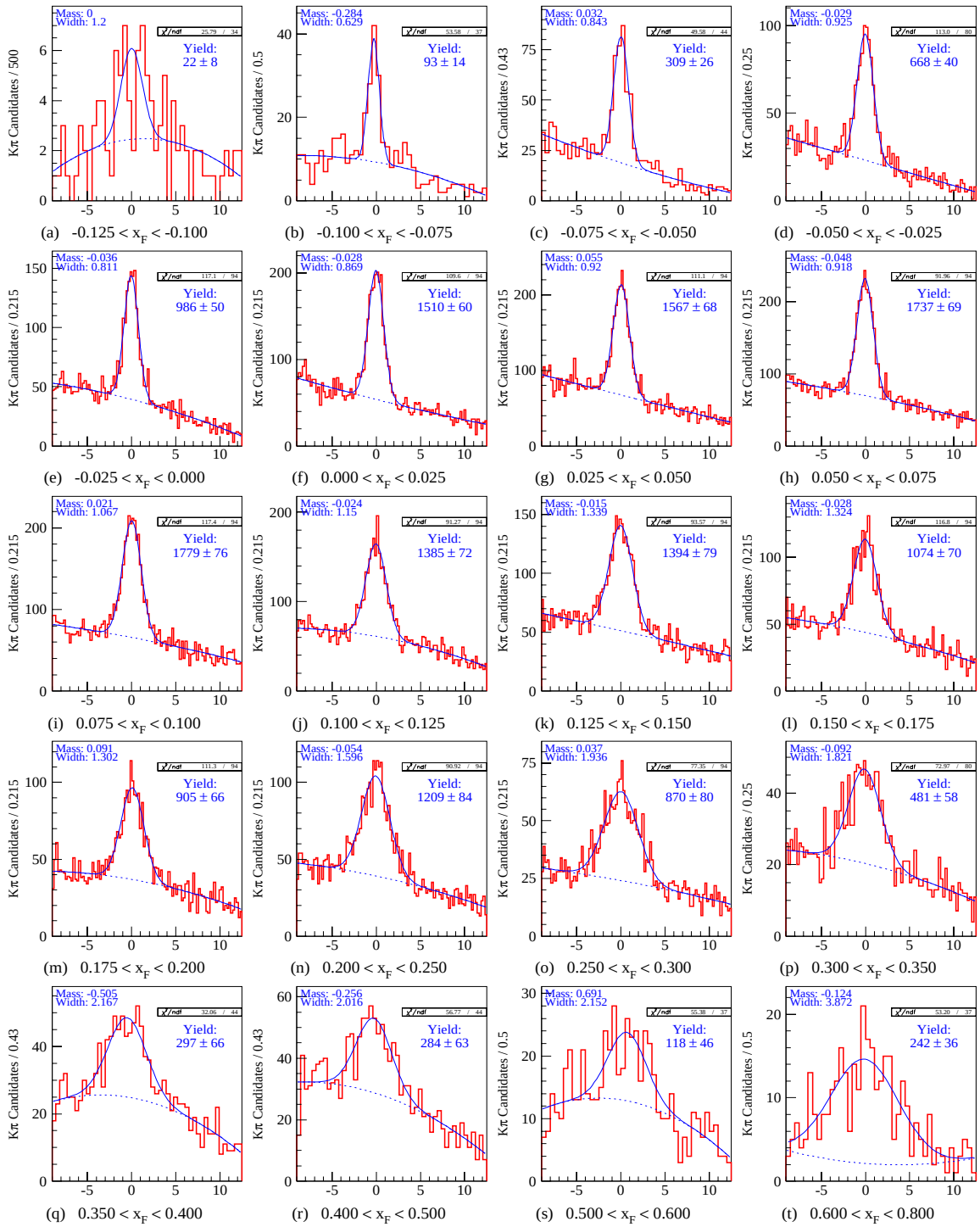

Fig. 4.4.— Sample A $K\pi$ normalized mass plots for 20 bins of x_F from the Release 7 E791 data with the nominal analysis cuts plus no events with an interaction in the Platinum target.

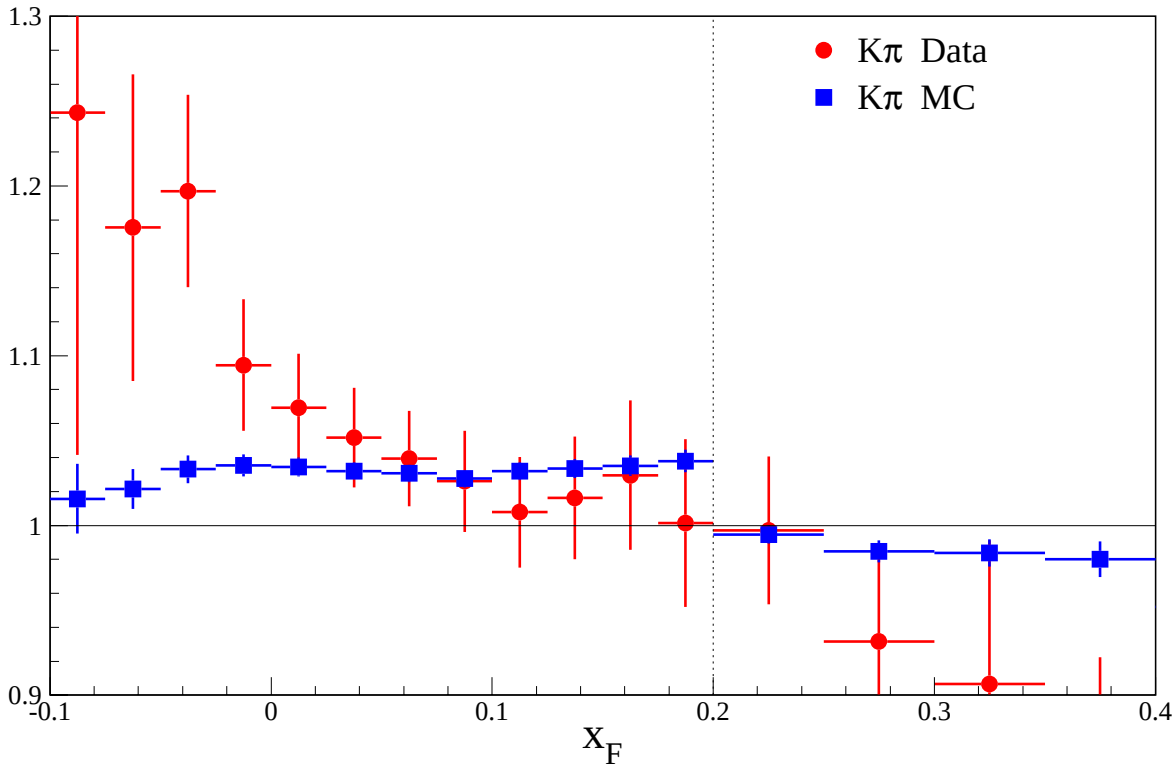

Fig. 4.5.— Ratio of yields obtained from fits to the normalized mass distribution to yields obtained from fits to the invariant mass distribution for data and Monte Carlo versus x_F. The errors are overestimated due to the significant correlations which are not taken into account.

category 3 track have a calculated resolution approximately twice as great as $K\pi$ candidates with only category 7 and 15 tracks. These events are often incorporated into the background of invariant mass plots but are correctly identified as signal in the normalized mass plots. Including category 3 track events into the background is less likely to occur in Monte Carlo events because the background level is much smaller, and its shape less complex. This is why the gains in Monte Carlo are smaller than in data. Since the calculated resolution does not account for the high x_F resolution loss, the width becomes too great to reliably fit above $x_F \sim 0.2$. Thus, for $K\pi$ and $K\pi\pi\pi$, the normalized mass plots are used to calculate yields for $x_F < 0.2$ and the invariant mass plots are used to calculate yields for $x_F > 0.2$. Category 3 decay tracks in $K\pi$

events with $x_F > 0.2$ are generally spurious and the few events with real category 3 decay tracks will not be correctly counted using the invariant mass. Therefore, for $K\pi$ events with $x_F > 0.2$, category 3 decay tracks are not allowed, as shown in Table 3.2. This explains why the Monte Carlo ratio shows a sudden jump to ≈ 1 above x_F of 0.2.

4.3 Final Data Mass Plots

The Release 5 and Release 7 signals used in the x_F distribution analysis for $K\pi$ and $K\pi\pi\pi$ are shown in Figures 4.6– 4.9. The signal functions are single Gaussians while the backgrounds are quadratic, cubic, quadratic and quadratic polynomials for the normalized mass $K\pi$ plots, invariant mass $K\pi$ plots, normalized mass $K\pi\pi\pi$ plots, and invariant mass $K\pi\pi\pi$ plots, respectively. The Release 5 and Release 7 signals used in the p_T^2 distribution analysis for $K\pi$ and $K\pi\pi\pi$ are shown in Figures 4.10– 4.13. The p_T^2 distributions are all obtained by fitting the normalized mass distributions with a Gaussian signal and a linear (quadratic) background for the $K\pi$ ($K\pi\pi\pi$) mode.

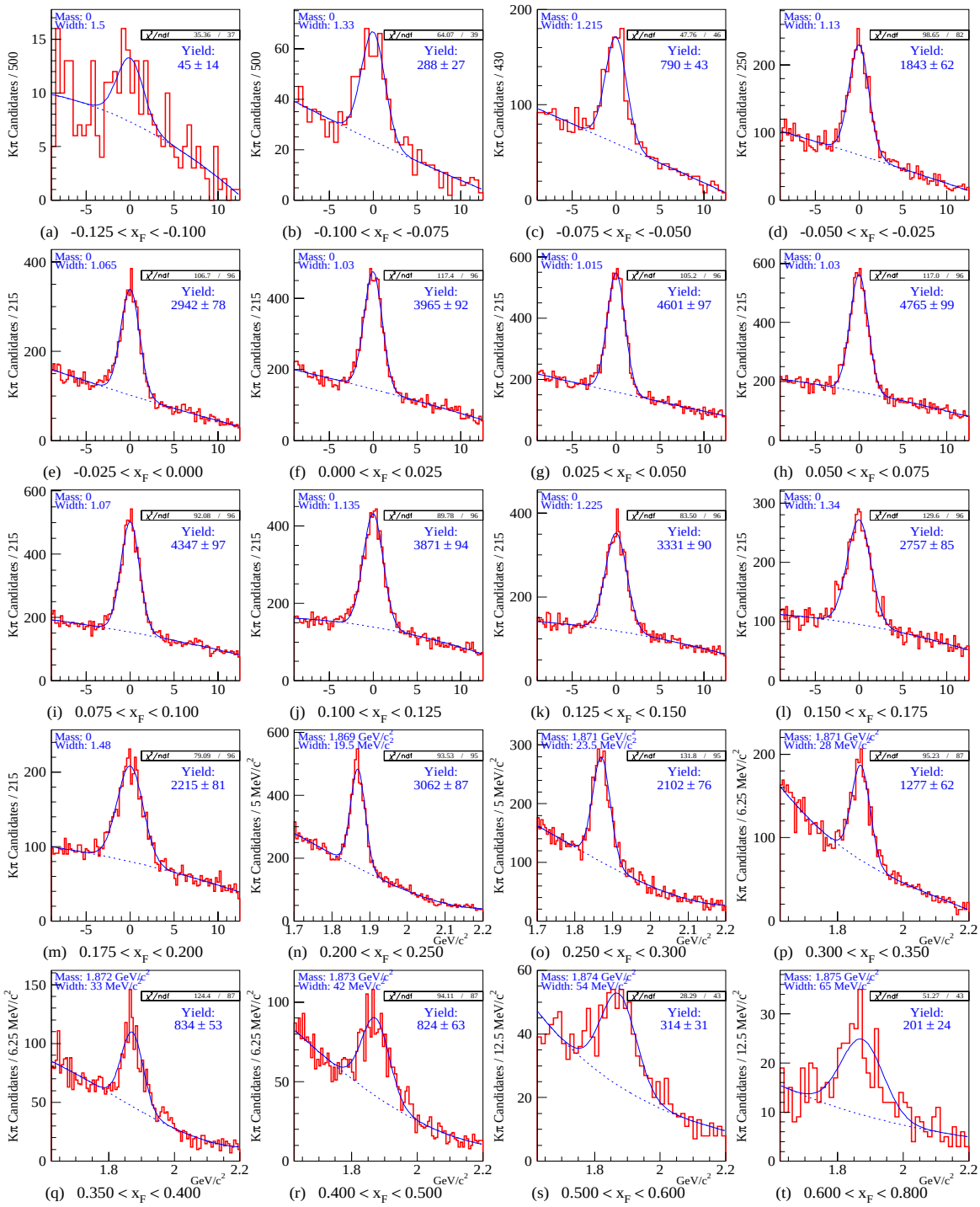

Fig. 4.6.— Sample B $K\pi$ mass plots for 20 bins of x_F from the Release 5 E791 data with the nominal cuts used in this analysis plus no interaction trigger runs, no poor quality runs, no runs with missing or inaccurate scaler data and no events with an interaction in the Platinum target.

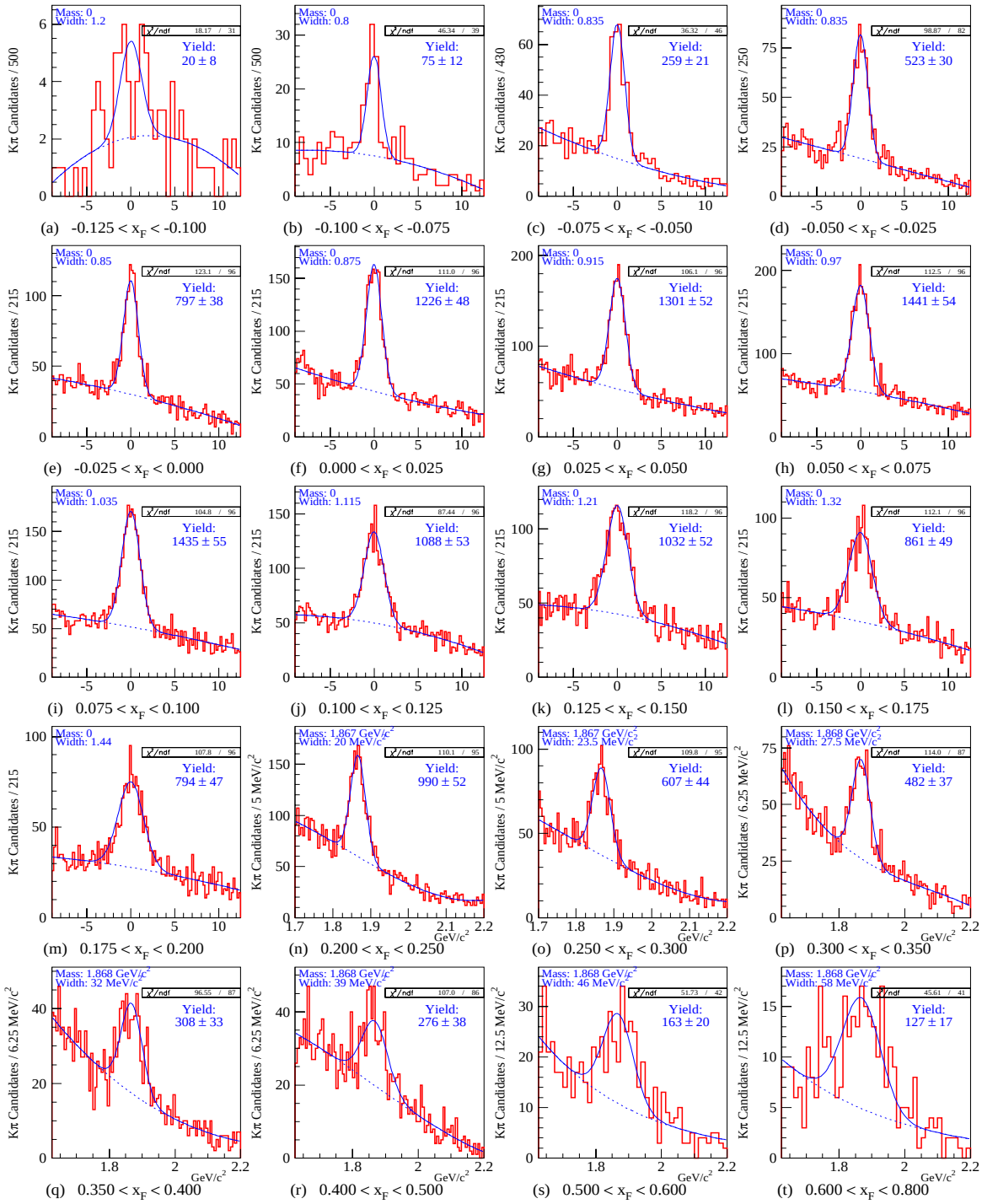

Fig. 4.7.— Sample B $K\pi$ mass plots for 20 bins of x_F from the Release 7 E791 data with the nominal cuts used in this analysis plus no interaction trigger runs, no poor quality runs, no runs with missing or inaccurate scaler data and no events with an interaction in the Platinum target.

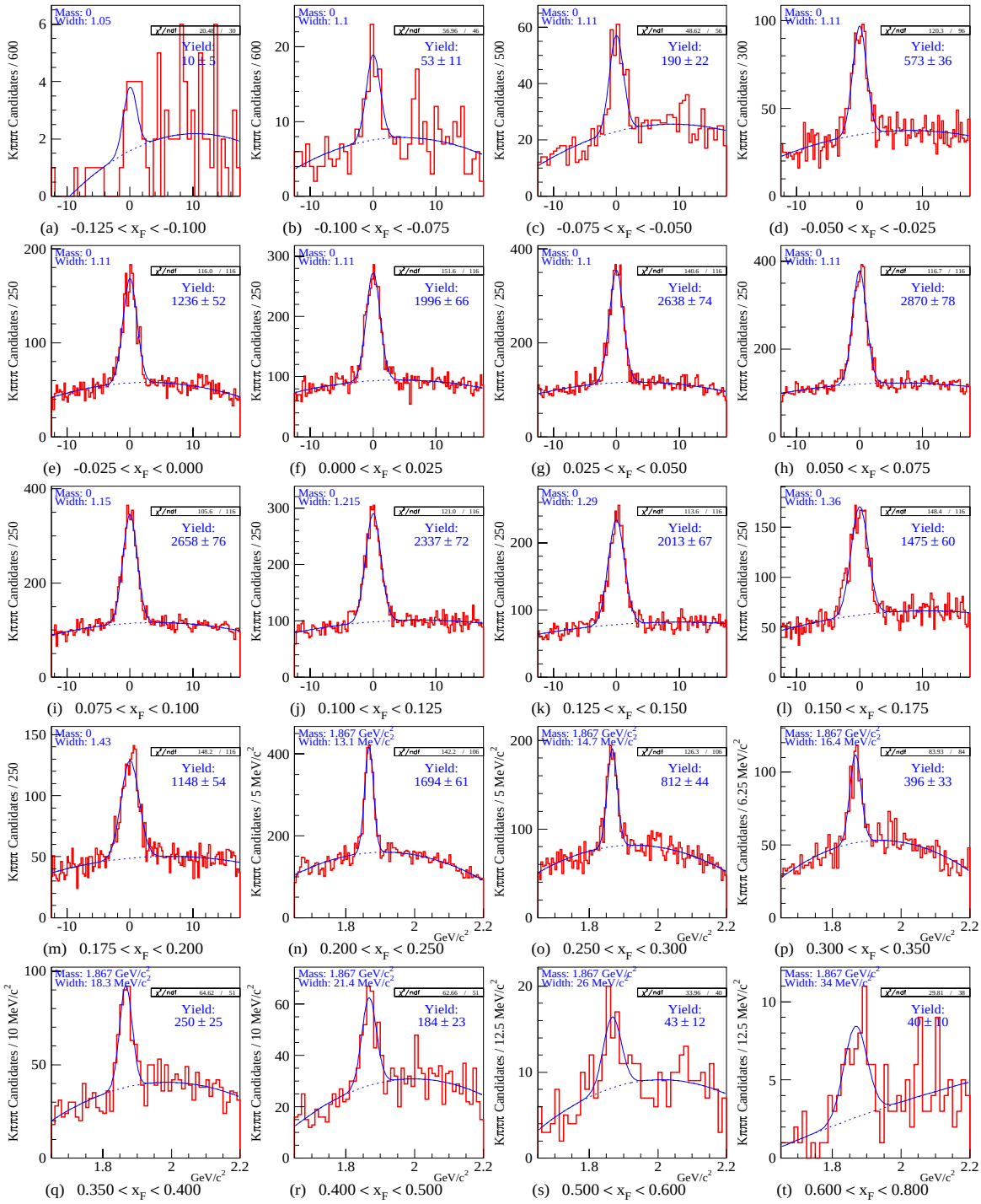

Fig. 4.8.— Sample B $K\pi\pi\pi$ mass plots for 20 bins of x_F from the Release 5 E791 data with the nominal cuts used in this analysis plus no interaction trigger runs, no poor quality runs, no runs with missing or inaccurate scaler data and no events with an interaction in the Platinum target.

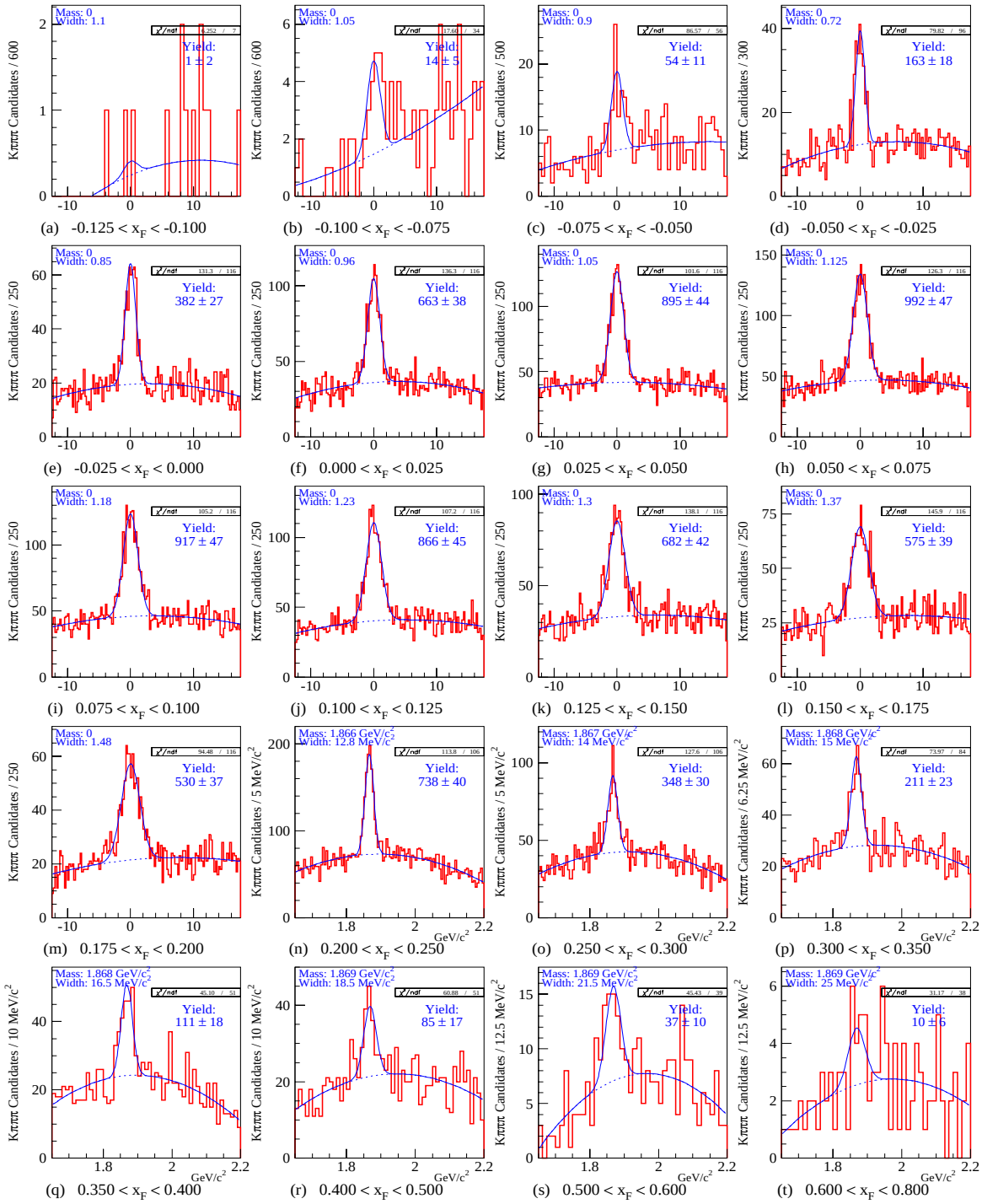

Fig. 4.9.— Sample B $K\pi\pi\pi$ mass plots for 20 bins of x_F from the Release 7 E791 data with the nominal cuts used in this analysis plus no interaction trigger runs, no poor quality runs, no runs with missing or inaccurate scaler data and no events with an interaction in the Platinum target.

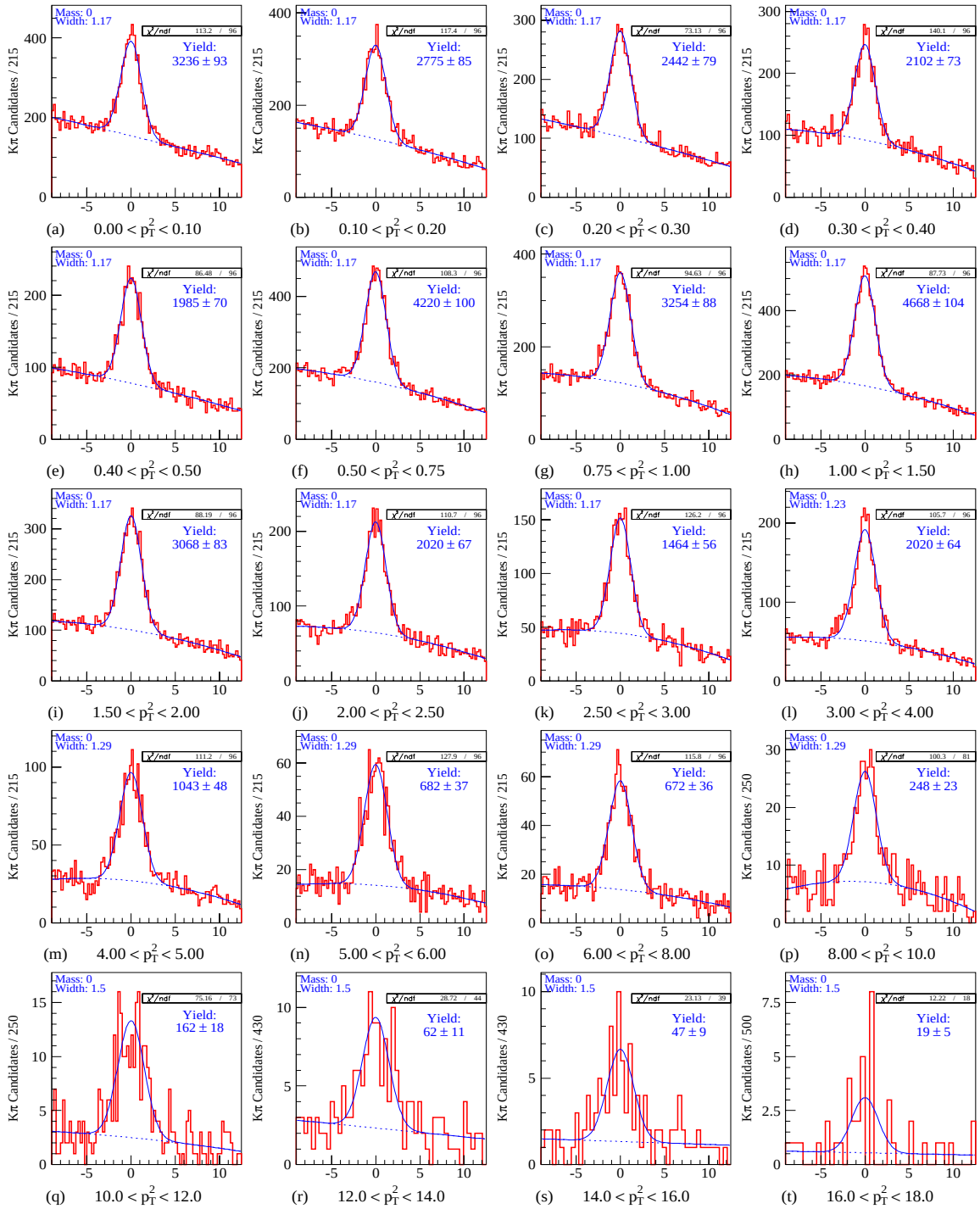

Fig. 4.10.— Sample B $K\pi$ mass plots for 20 bins of p_T^2 from the Release 5 E791 data with the nominal cuts used in this analysis plus no interaction trigger runs, no poor quality runs, no runs with missing or inaccurate scaler data and no events with an interaction in the Platinum target.

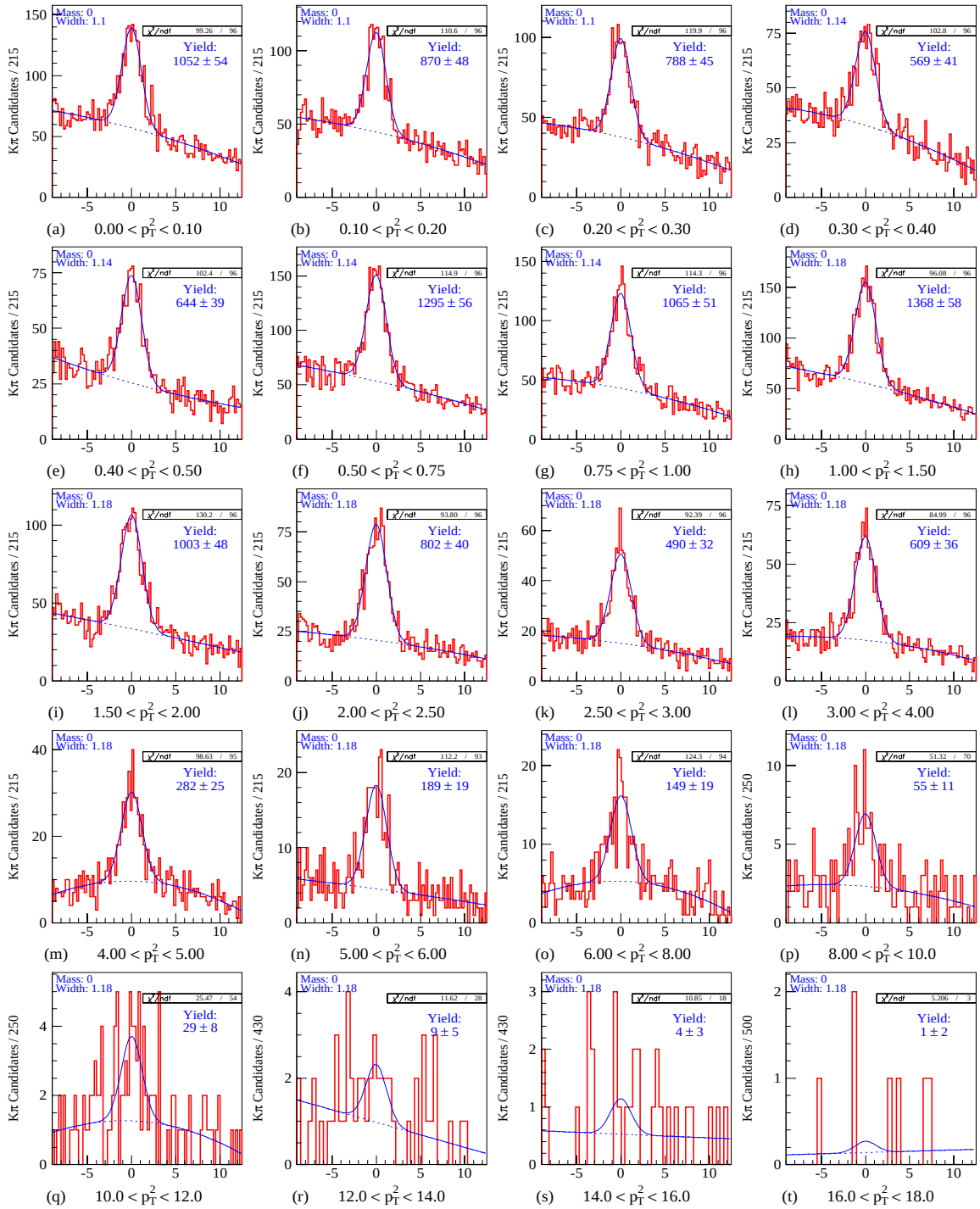

Fig. 4.11.— Sample B $K\pi$ mass plots for 20 bins of p_T^2 from the Release 7 E791 data with the nominal cuts used in this analysis plus no interaction trigger runs, no poor quality runs, no runs with missing or inaccurate scaler data and no events with an interaction in the Platinum target.

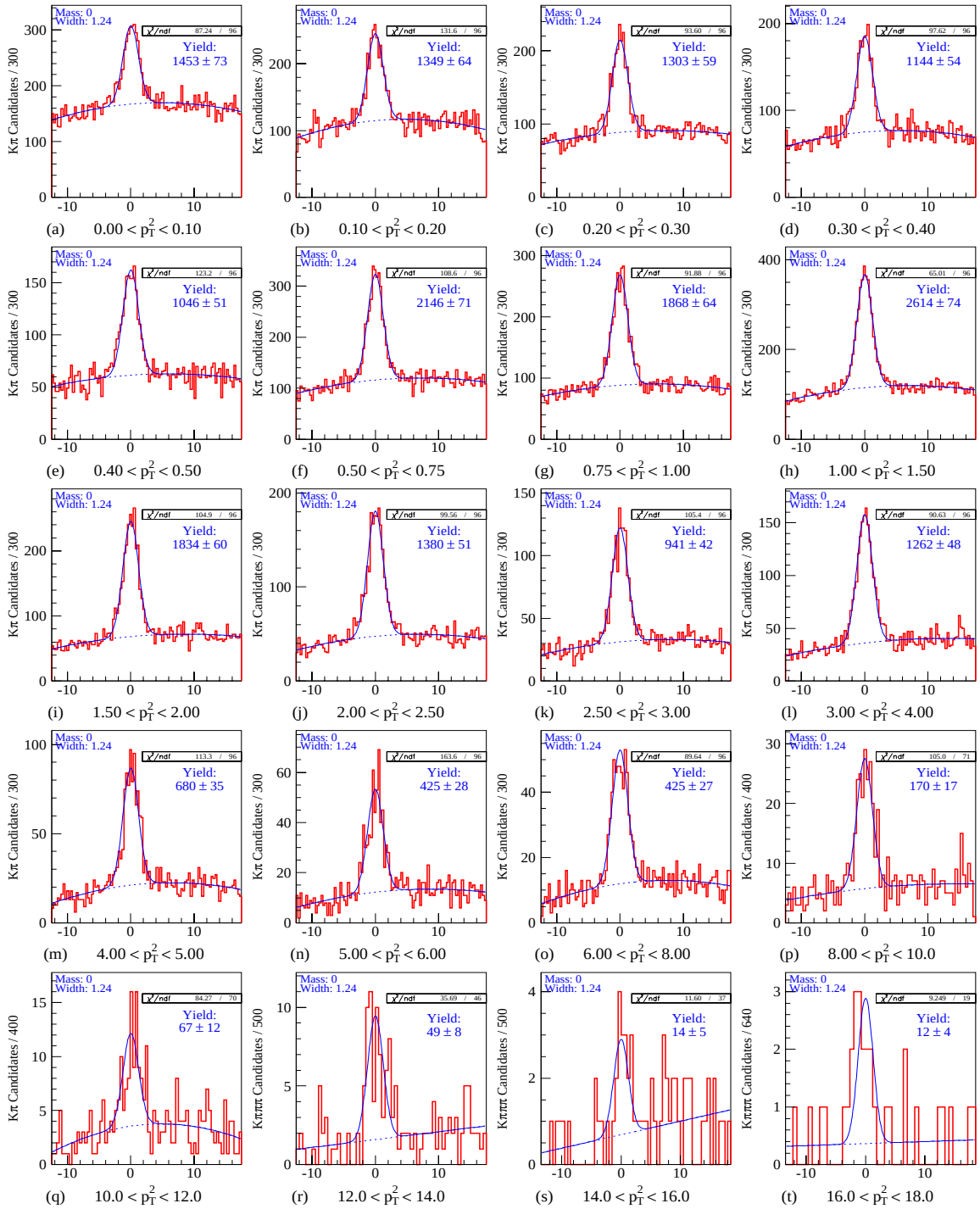

Fig. 4.12.— Sample B $K\pi\pi\pi$ mass plots for 20 bins of p_T^2 from the Release 5 E791 data with the nominal cuts used in this analysis plus no interaction trigger runs, no poor quality runs, no runs with missing or inaccurate scaler data and no events with an interaction in the Platinum target.

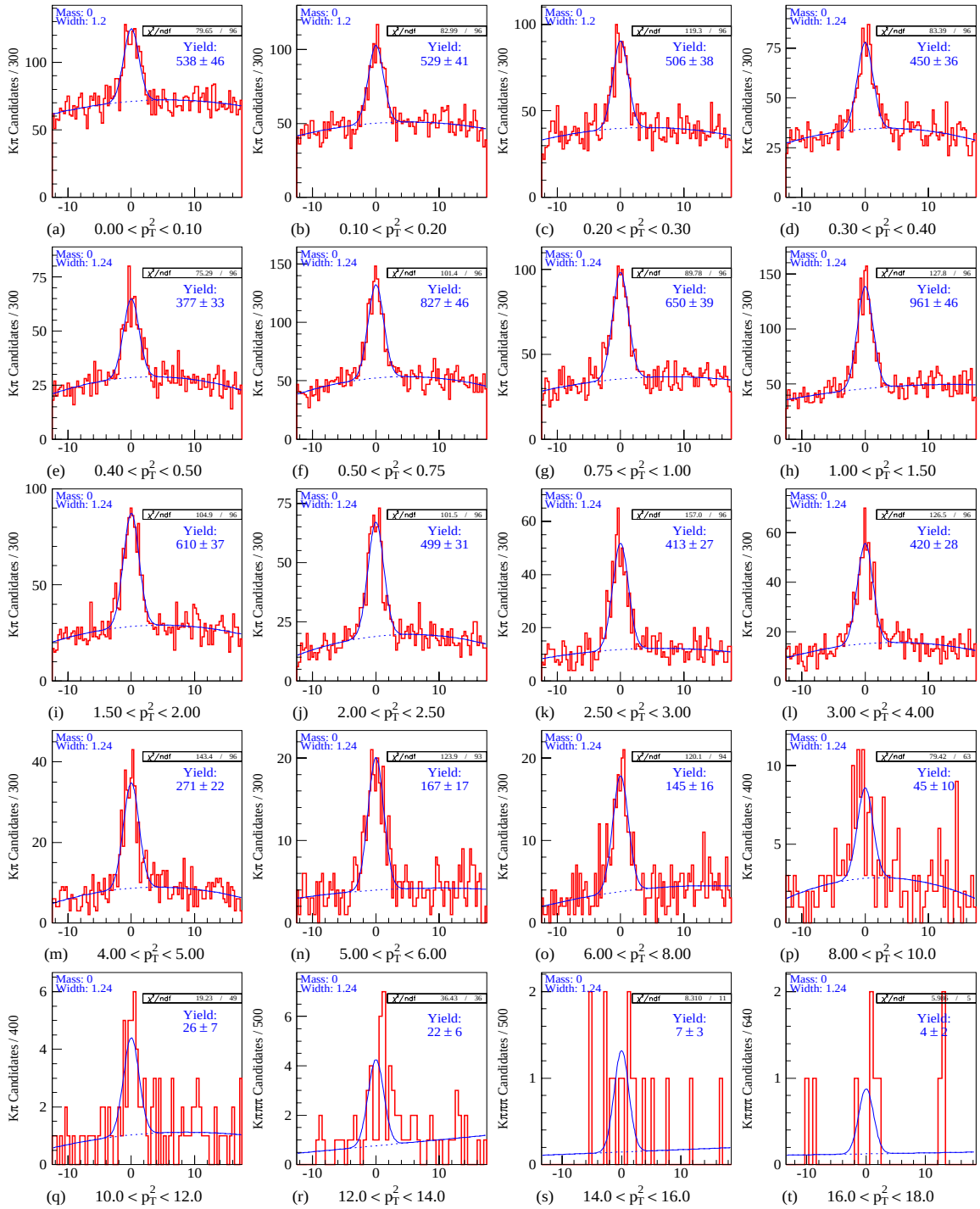

Fig. 4.13.— Sample B $K\pi\pi\pi$ mass plots for 20 bins of p_T^2 from the Release 7 E791 data with the nominal cuts used in this analysis plus no interaction trigger runs, no poor quality runs, no runs with missing or inaccurate scaler data and no events with an interaction in the Platinum target.

Chapter 5

Acceptance

In order to determine the D^0 production cross sections, one needs to know how many D^0 particles were produced by a given number of beam particles. The figures in Chapter 4 only provide the number of $D^0 \to K\pi$ and $D^0 \to K\pi\pi\pi$ particles reconstructed. To obtain a cross section measurement, we must account for all of the D^0 particles we missed. First we must correct for the unseen decay states of the D^0. We can obtain the total number of D^0 particles from each of the decay samples by using the Particle Data Group (PDG)[31] branching fractions; $(3.85 \pm 0.09\%)$ for $K\pi$ and $(7.6 \pm 0.4\%)$ for $K\pi\pi\pi$. Therefore, once we know the number of $D^0 \to K\pi$ and $D^0 \to K\pi\pi\pi$ candidates, we can obtain two independent measurements of the number of D^0 candidates. Since we do not correctly identify 100% of the $K\pi$ and $K\pi\pi\pi$ D^0 candidates, we must also make a correction for our inefficiency. The efficiency, or acceptance, for finding a decay $D^0 \to X$ can be written as

$$A(D^0 \to X) = \epsilon_{live}\, \epsilon_{trig}(D^0 \to X)\, \epsilon_{rec}(D^0 \to X) \tag{5.1}$$

where ϵ_{live} is the livetime of the experiment, ϵ_{trig} is the triggering efficiency and $\epsilon_{rec}(D^0 \to X)$ is the reconstruction efficiency. Each of these terms is calculated below.

5.1 Experiment Livetime

The quantity ϵ_{live} is the livetime of the experiment, that is, the fraction of the time that the experiment was able to take data, or "live." The deadtime, time when the experiment was unable to take data, was due to processing a previous pretrigger or reading out the detectors after a trigger. If we had recorded the total number of π^- beam particles incident on our target (N_{beam}), we would have overestimated the number of beam particles that were able to trigger the experiment, since we were only sensitive to $\epsilon_{live}N_{beam}$ beam particles. Instead, we counted beam particles using a scaler that was gated off when the experiment was "busy," i.e., not able to record a new event and thus measured $\epsilon_{live}N_{beam}$ directly. In all cases, N_{beam} actually refers to good beam, which is a hit in the beam spot counter and no hit in the halo counter (Section 2.4).

5.2 Trigger Efficiency

If we had triggered the experiment for every beam particle, we would have recorded every event in which charm was produced. Since we imposed additional requirements in the trigger beyond good beam we need to determine the efficiency of each of them for selecting the two charm decay samples we are using to measure the D^0 cross section. The primary requirements, described in Section 2.4, are a 4.5 MIP pulse in the interaction counter, E_T energy greater than 3 GeV, not more than $\sim$ 800 GeV total energy, less than $\sim$ 2 MIPs in the beam spot counter and no hits in the beam spot counter for 78 ns on either side of the triggering hit.

The efficiency for the interaction requirement is very close to 100% for events which we can reconstruct. Since the reconstruction program requires the primary vertex to contain at least two tracks and since our decay modes have 2-4 charged

tracks, there is a minimum of 4 charged tracks passing through the interaction counter. In addition, there will be other tracks from the unreconstructed charm decay and other low momentum tracks which were not used in fitting the primary. For the charm sample, the average number of (non-beam) tracks used to fit the primary is 6.5 and the average number of tracks reconstructed with both the silicon and the drift chambers is 13. Therefore, we believe the interaction requirement to be essentially 100% efficient for the charm decays of interest. Events which would not pass the interaction trigger requirement would also fail to be reconstructed. Therefore, these events will be accounted for by the reconstruction efficiency, described in Section 5.3.

The second part of the trigger efficiency comes from the E_T requirement. Since 9% of the data was taken with only an interaction requirement, it is possible to determine the E_T efficiency directly. Using the interaction runs we find the amount of signal with and without the E_T bit set. This efficiency is the "E_T Efficiency" in Table 5.1, and it is also very close to 100% for reconstructible charm.

The three vetoes compose the last part of the trigger efficiency. Events triggered with the vetoes not imposed are referred to as "dirty," while events where the veto bits are required to be off are "clean." The veto efficiency can be calculated in two ways. The first is to use an approach similar to that for the E_T efficiency. There were some dirty interaction runs taken where the vetoes were not used. In addition, the normal E_T trigger also included prescaled interaction events. For half of the data taking, these prescaled interaction events also did not use the cleaning vetoes. Using these samples of events in which the beam cleaning vetoes were not required but were simply recorded using bits in a latch, we can calculate the number of charm decays with and without the latch bits set to determine the inefficiency caused by the cleaning vetoes. This method yields an inefficiency of $25.3 \pm 1.2\%$. That is, $25.3 \pm 1.2\%$ of the

charm events have one or more of the veto bits set and would not have been recorded had the vetoes been required. The second method of measuring the veto efficiency uses the scaler information. For each live pretrigger a PLU calculates whether or not it was a clean live pretrigger and both of these quantities are scaled. The ratio of dirty live pretriggers to live pretriggers is 34.0%. The discrepancy between the number from charm and the number from the scalers seems to come from two sources. The number from charm (25.3%) can be low because events with vetoes are usually more difficult to reconstruct (they have multiple beam particles and higher track multiplicities). Therefore, we miss more of the charm events with vetoes than the charm events without vetoes. However, the value obtained from the scalers can be high because it is easier for a veto event to fake the pretrigger than a non-veto event. That is, multiple beam particles or upstream interactions (which are detected by the vetoes) can simulate a target interaction and cause a pretrigger without there being a real target interaction. Since we don't know the relative importance of these, or other, effects, we take the average of the two numbers and assign a systematic error of half the difference which we add in quadrature with the statistical errors. The resulting efficiency is one minus the measured inefficiency and is reported as "Veto Efficiency" in Table 5.1.

There is another inefficiency which, although not due to the trigger, will be included here as part of the trigger efficiency. The inefficiency is the loss of data between the full trigger decision and the events reaching the filter. There are two places where data can be lost. The data can fail to be written on tape or the data can fail to be read from the tape. The first effect can be measured by counting the number of events which were written onto tape divided by the number of full triggers recorded by the scalers. Runs where this ratio is greater than 100% were due to bad

scaler files and have already been discarded. Runs where this ratio is less than 100% are due to problems with the event readout. This occurs because the event builder makes checks on the data and if any of them fail, the event is discarded. Two runs where this was a large (greater than 5%) problem were discarded. The remaining runs give a total loss of 0.8%, or 99.2% efficiency, with virtually zero error. The second loss, failure to read data from tapes, comes mainly from problems with the tape media. During the event reconstruction, tapes and tape drives would fail during the event reading. If the tape was past a certain point when the failure occurred, the tape was not rerun. Also, in some cases the tape could not be rerun because the error was too severe. The experiment database kept track of the number of events *into* the filter. Therefore, the tape reading efficiency should be the number of events into the filter divided by the number of events written to tape which is 98.4%. However, a closer look at the database reveals many small discrepancies. After fixing many of these discrepancies, the numbers remained virtually the same; however, we take a conservative approach and assign an error of 1.0%. Combining these two efficiencies gives us the "Tape Efficiency" shown in Table 5.1. The tape reading efficiency after the event reconstruction is assumed to be 100%.

Decay mode	E_T Efficiency	Veto Efficiency	Tape Efficiency	Trigger Efficiency
$K\pi$	$99.3 \pm 0.2\%$	$70.3 \pm 4.3\%$	$97.6 \pm 1.0\%$	$68.1 \pm 4.2\%$
$K\pi\pi\pi$	$99.9 \pm 0.1\%$	$70.3 \pm 4.3\%$	$97.6 \pm 1.0\%$	$68.5 \pm 4.2\%$

Table 5.1: Trigger efficiency

The total "Trigger Efficiency" in Table 5.1 is the product of the E_T efficiency, veto efficiency and tape efficiency. Since the error is much larger than the difference between the $K\pi$ and $K\pi\pi\pi$ efficiencies, we use the average as the final triggering efficiency and increase the error to include the range of both values. That is, $\epsilon_{trig}(D^0 \rightarrow$

$K\pi) \;=\; \epsilon_{trig}(D^0 \to K\pi\pi\pi) \;=\; 68.3 \pm 4.4\%.$

5.3 Reconstruction Efficiency

The last term in Eq. 5.1 is the reconstruction efficiency. The reconstruction efficiency is used to correct for $D^0 \to X$ events which were written on tape and were within the kinematic regions we are investigating, but were not counted as signal. This loss of events can be an effect of the selection criteria, inefficient detectors, geometric acceptance of the spectrometer, etc. This is all modeled by the Monte Carlo program.

5.3.1 First Order Reconstruction Efficiency Calculation

To measure the reconstruction efficiency we use the Monte Carlo program described in Section 2.6. We run the Monte Carlo program with the requirement that there is a D^0 in the event and that it decays to $K\pi$ ($K\pi\pi\pi$). In the generation stage we can count the number of $D^0 \to X$ candidates and compare this to the number of $D^0 \to X$ candidates reconstructed. The reconstruction efficiency is thus

$$\epsilon_{rec}(D^0 \to X) = \frac{N_{rec}(D^0 \to X)}{N_{gen}(D^0 \to X)}. \tag{5.2}$$

When measuring the differential cross section (versus x_F or p_T^2), we will bin the reconstruction efficiency in x_F and p_T^2, i.e.,

$$\epsilon_{rec}(D^0 \to X,\, x_F) = \frac{N_{rec}(D^0 \to X,\, x_F)}{N_{gen}(D^0 \to X, x_F)} \qquad \text{and} \tag{5.3}$$

$$\epsilon_{rec}(D^0 \to X,\, p_T^2) = \frac{N_{rec}(D^0 \to X,\, p_T^2)}{N_{gen}(D^0 \to X, p_T^2)}. \tag{5.4}$$

When measuring p_T^2 or x_F distributions and the total cross section, we must restrict ourselves to a range for which we have non-zero acceptance. In the case of the total cross section, previous fixed-target experiments have quoted a value for $x_F > 0$ which

will be followed here. For the p_T^2 distributions we also choose the range $x_F > 0$; for the x_F distribution we allow $-0.125 < x_F < 0.8$.

When calculating the reconstruction efficiency as a function of one variable (e.g. x_F or p_T^2) we are effectively integrating over all other variables. Therefore, in order for the Monte Carlo calculation to give the correct result, all other variables must either be the same in Monte Carlo and data or must not affect our reconstruction efficiency. While "all other variables" comprises a nearly infinite set, we can use our knowledge of how charm is reconstructed to determine which variables are important in determining the reconstruction efficiency. The variables which we are analyzing, x_F and p_T^2, are two variables with respect to which the longitudinal and transverse reconstruction efficiency of the D^0 varies. The reconstruction efficiency versus these two variables can be found in Fig. 2.2. Low x_F D^0 candidates are composed of low momentum tracks which can miss the spectrometer or suffer too much multiple Coulomb scattering to be reconstructed. High x_F D^0 candidates are composed of high momentum tracks which can be lost down the drift chamber hole. Also, the mass resolution at high x_F, especially for the $K\pi$ events, is poor due to the small opening angle between the tracks. Low p_T^2 D^0 events can be difficult to reconstruct because the tracks can be lost down the drift chamber hole or confused with the many other low p_T tracks common in the underlying event (beam and target fragmentation products). The z location of the decay vertex is also important because the further upstream the decay is, the more likely it is that some of the tracks will be outside of the acceptance of the silicon system. This z location depends solely on the lifetime of the D^0, the x_F of the D^0 and the position of the primary vertex. The primary vertex z position is easily modeled in the Monte Carlo because the target positions and materials are well known. Since the x_F distribution is already being examined, the remaining part of the z location

dependence comes from the D^0 lifetime. The Monte Carlo uses a large library of reconstructed data beam tracks to correctly distribute the transverse position of the primary vertex and relate the production z axis to the experiment z axis. Other variables which might affect reconstruction efficiency are variables which specifically relate to the underlying event. These include the number of tracks in the primary, the total number of tracks in the event, the average momentum or transverse momentum of these tracks, etc. Given the plethora of variables described here, it is not surprising that the Monte Carlo fails to reproduce all of them correctly. Fortunately all is not lost as event weighting comes to the rescue.

5.3.2 Weighting the Monte Carlo

In cases where the Monte Carlo does not generate the correct distribution, we can weight the generated events in such a way as to obtain the correct distribution. The simplest way to do this is by accepting events at different rates during the generation phase of the Monte Carlo. It is also possible to weight already generated and reconstructed Monte Carlo events. This is done by weighting the truth table values of the generated events and reconstructed events the same way. This type of *post hoc* weighting is used for this analysis. The only drawback to this approach is lack of statistics. If some region of the Monte Carlo is depleted by a large factor relative to the data then large weights will be applied to these Monte Carlo data and the statistical error will be increased by the same weight. For this reason, among others, it is desirable to have a Monte Carlo which closely resembles the data before weighting.

To obtain the weighting function for a particular variable, e.g. p_T^2, we simply divide the reconstructed data distribution by the reconstructed Monte Carlo distribution. A parameterization of the resulting distribution gives us the weighting function.

The nth weighting function is obtained in the same way using a Monte Carlo function that has already been weighted by all the previous weighting functions; i.e., weights from more than one weighting function are combined multiplicatively. The variables used in the weighting are D^0 lifetime, D^0 p_T^2, D^0 x_F and event PT715. PT715 is defined here as the scalar sum of the p_T of each of the category 7 & 15 tracks (tracks which go through both magnets) which are not decay products of the D candidate. This provides a measure of the underlying event.

The largest discrepancy between the E791 default Monte Carlo and data is in the p_T^2 distribution. The data has a much harder p_T^2 distribution than the Monte Carlo. This was partially remedied by adjusting some parameters in the PYTHIA/JETSET program (cf Sec. 6.2.3.1) and generating more Monte Carlo events. The default E791 Monte Carlo will be labeled MC1 while the modified, higher p_T, Monte Carlo will be labeled MC2. 7.5 million $D^0 \to K\pi$ and 10 million $D^0 \to K\pi\pi\pi$ decays were generated with MC1 while 5 million $D^0 \to K\pi$ and 10 million $D^0 \to K\pi\pi\pi$ decays were generated with MC2.

The effect of weighting is seen in the ratios of data to Monte Carlo versus x_F and p_T^2 shown in Fig. 5.1. It is clear that MC2 is in better agreement with the data than MC1 for both the x_F and p_T^2 distributions because the hollow diamonds show a flatter distribution on the right (MC2) side of the plot than than on the left (MC1) side. In all cases, however, the weighting procedure generates good agreement between the Monte Carlo and data as shown by the flatness of the filled stars.

The effect of weighting on the acceptance can be seen in Fig. 5.2. This shows the ratio of acceptance after weighting to acceptance before weighting versus x_F and p_T^2 for both $K\pi$ and $K\pi\pi\pi$ decays. The ratios are shown separately for MC1 and MC2. The p_T^2 acceptance shows little functional dependence on the weighting although the

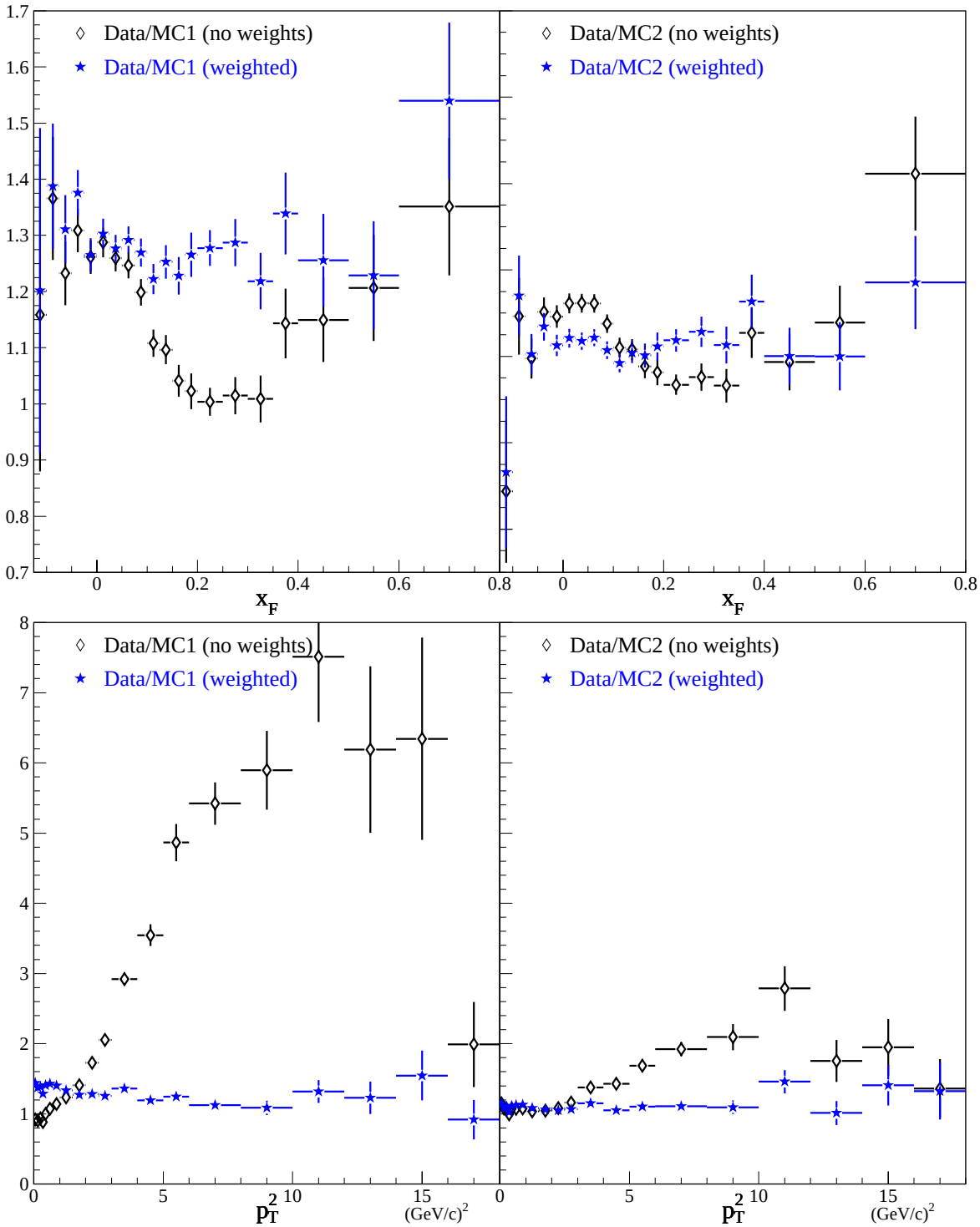

Fig. 5.1.— Ratio of $K\pi$ data to Monte Carlo with and without Monte Carlo weighting as a function of x_F (top) and p_T^2 (bottom) for the default E791 Monte Carlo, MC1 (left), and a higher p_T Monte Carlo, MC2 (right).

overall acceptance changes significantly. The x_F acceptance is modified significantly by the weighting, especially at low and high x_F. This is caused almost entirely by the p_T^2 weighting. The PYTHIA/JETSET physics generator correlates high p_T^2 and low (negative) x_F events. Therefore, weighting the high p_T events (for which we have good acceptance) results in an increase in the acceptance at negative x_F. This is much less prominent for MC2 where the p_T^2 weighting is less severe (because the original distribution was closer to the data). High p_T events are also correlated with high x_F events. This is not due to the physics generator, but rather the effect of the drift chamber hole, described in Section 2.3.3.2. We are much more likely to reconstruct high p_T high x_F events than low p_T high x_F events so weighting the high p_T events results in a better acceptance at high x_F.

While this weighting procedure is probably sufficient for the analysis, there is one further subtlety which might make the procedure not completely correct. If the physics correlations between the weighted variables are different between data and Monte Carlo then the distributions might be correct on average but be wrong in individual bins of some variable. For example, from Fig. 5.1 we see that when we integrate over x_F we get good agreement between the data and the weighted Monte Carlo for the p_T^2 distribution. However, it might be that at high x_F, the p_T^2 distributions will disagree. Then the acceptance for the high x_F events will be incorrect. This can be checked by comparing the Monte Carlo and data x_F distributions in bins of p_T^2 and the p_T^2 distributions in bins of x_F as shown in Fig. 5.3. Although the average is flat in all cases, it is clear there are significant variations for individual bins, especially high x_F and high p_T^2 bins. Since the high x_F and high p_T^2 regions do not contribute many events, it is to be expected that they are not flattened by weighting to the average. To fix this we apply more weighting functions in the regions of disagreement.

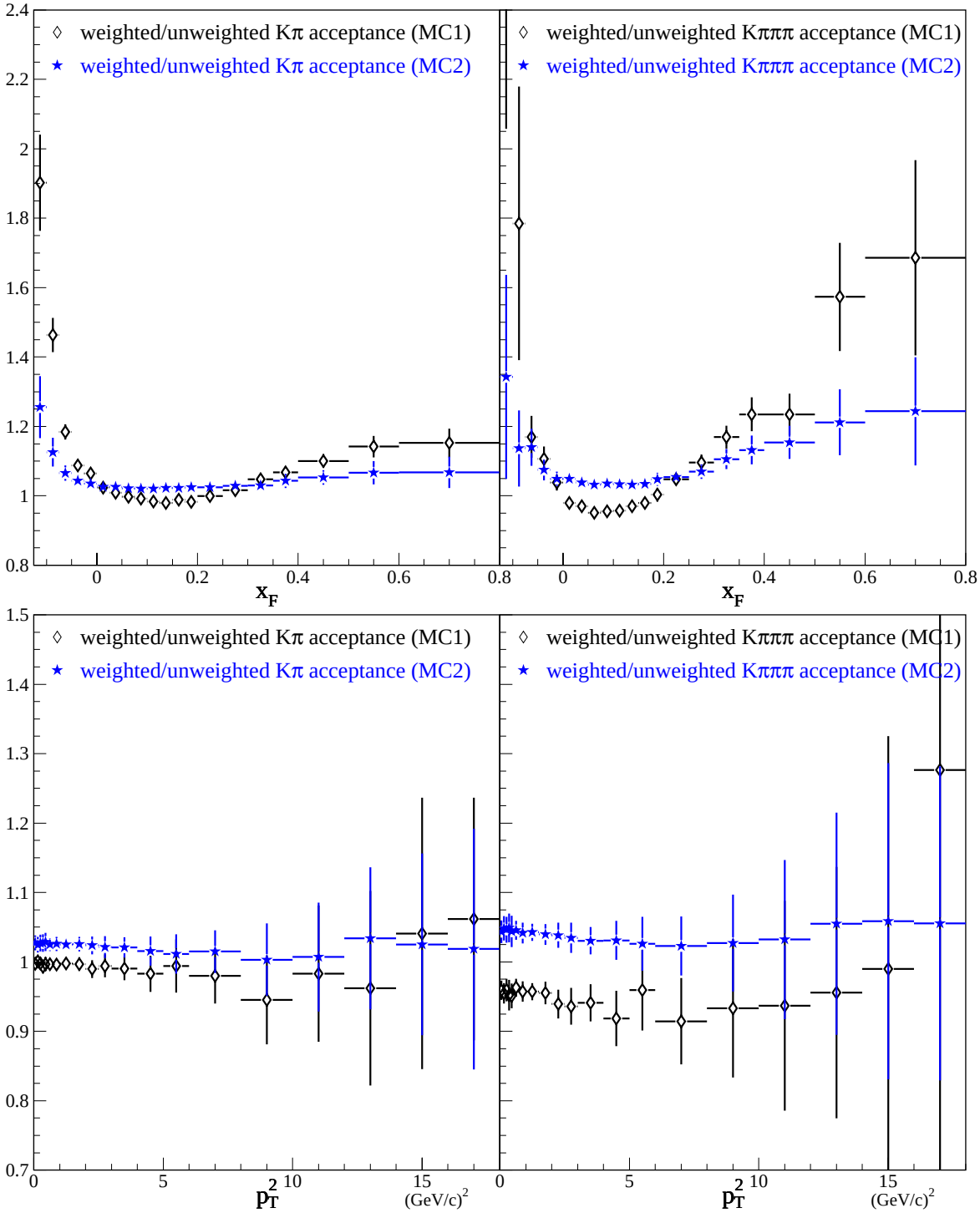

Fig. 5.2.— Ratio of weighted to unweighted acceptances as a function of x_F (top) and p_T^2 (bottom) for $K\pi$ (left) and $K\pi\pi\pi$ (right) and for both Monte Carlos (MC1 (stars) and MC2 (diamonds)). The errors shown are only a maximum since they do not account for the significant correlations between the weighted and unweighted samples.

The result is good agreement for all bins as shown in Fig. 5.4. Unfortunately, this procedure introduces slight fluctuations in the average case, primarily at $x_F<0$. This is due to the different bin sizes used in the two methods. Averaging over all x_F (p_T^2), as was done for the first iteration, allows smaller bins in p_T^2 (x_F) which gives better resolution of structure in the distribution. When the data is separated in bins of x_F (p_T^2), the bins of the p_T^2 (x_F) distribution must be larger to retain the necessary statistical significance. Since both of the weighting schemes must average over some quantities, they are both simply approximations to the unknown truth. Both results give essentially the same acceptances; we will use the second result, hereafter called correlations weighting, because it incorporates more information.

5.3.3 Factoring in Time Dependence

At the start of the Monte Carlo program, various files are read which provide information about the experiment. These files include geometry information, efficiencies, resolutions, noise rates, etc. Some of the files, like the geometry information and drift chamber resolutions are simply copies of files used during the original event reconstruction. Other files like the efficiencies and noise rates were created for the Monte Carlo. The files were copied or generated from runs recorded between 25% and 30% of the way through the data taking. While the experiment geometry remained very stable throughout the five-target running, the efficiencies and resolutions varied significantly. The most significant variation, described in Section 2.3.3.2, is the drift chamber central region inefficiency. One might expect the hole to be approximately Gaussian with dimensions roughly corresponding to the incident π^- beam. In reality, the x dimension of the hole looks more like a central Gaussian region on top of a band while the y dimension of the hole is approximately Gaussian. Part of the band effect in

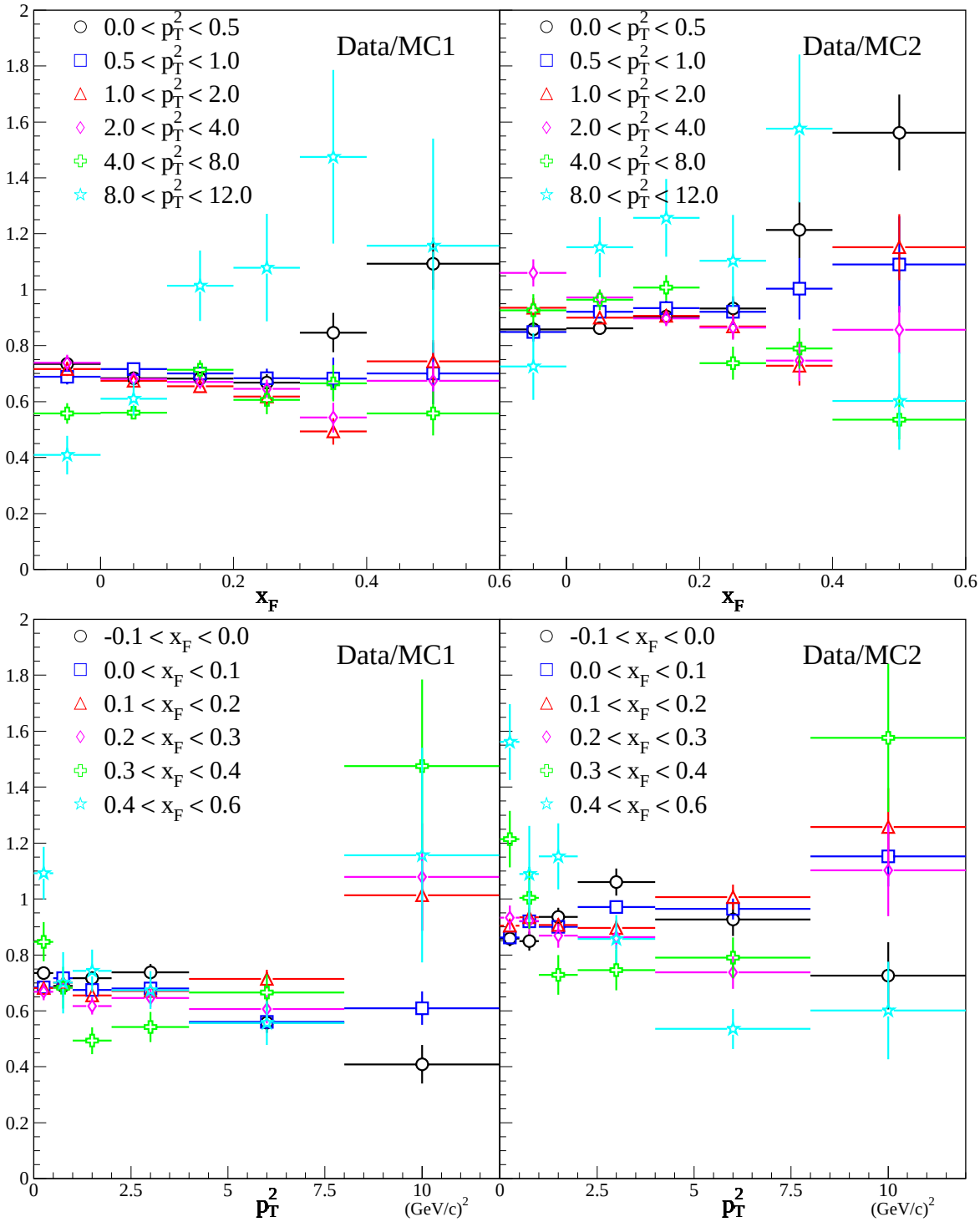

Fig. 5.3.— Ratio of $K\pi$ data to weighted Monte Carlo as a function of x_F in bins of p_T^2 (top) and as a function of p_T^2 in bins of x_F (bottom) for MC1 (left) and MC2 (right).

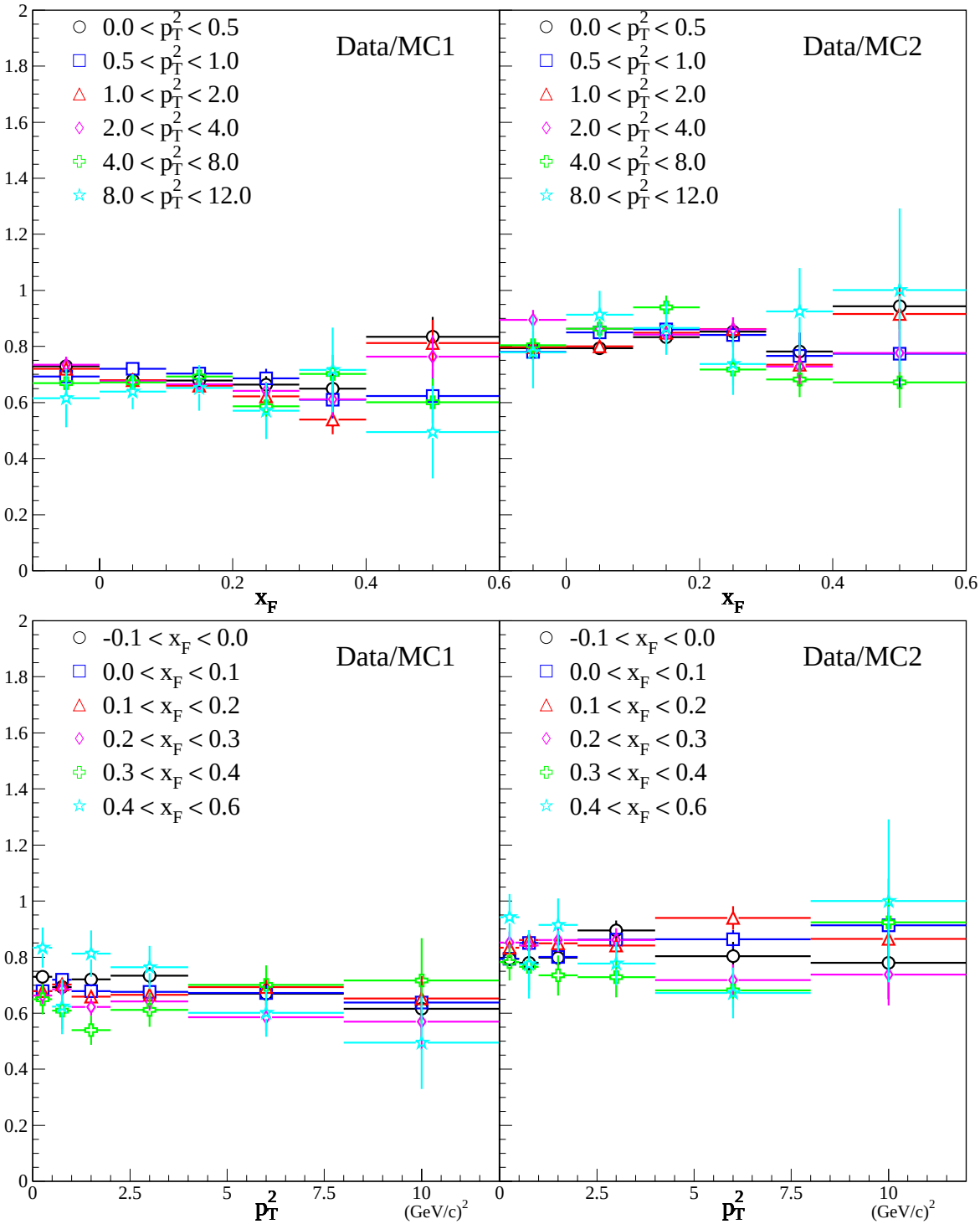

Fig. 5.4.— Ratio of $K\pi$ data to weighted Monte Carlo as a function of x_F in bins of p_T^2 (top) and as a function of p_T^2 in bins of x_F (bottom) for MC1 (left) and MC2 (right).

the x dimension comes from previous photoproduction experiments (E516 and E691). In these experiments, electron-positron pairs produced from the incident photon were spread more or less uniformly in x by the magnets. To model the inefficiency observed in E791, the central region of each drift chamber plane is divided into 10–20 slices in x, each slice encompassing approximately 3 mrad. Each slice has an associated Gaussian function describing the inefficiency for that slice which is used by the Monte Carlo during the event digitization to determine if the hit should be recorded.

To account for the time dependence, the Monte Carlo program was run for five different run periods, each representing approximately 20% of the data. For each of the five run periods, a different drift chamber hole parameterization file, based on data from a run in the middle of that run period, was used. The appropriate drift chamber resolution files were also used in both the generation and reconstruction phases. The drift chamber efficiencies outside of the hole region and the silicon and PWC efficiencies were fairly constant throughout the data taking. Near the end of the first run period, however, many changes were made to the spectrometer. The most important change was an increase in efficiency of the ninth vertex silicon plane from 57% to 90%. Other minor changes included fixing two drift chamber planes in D1 and three beam PWC planes. Therefore, different silicon, PWC and drift chamber efficiency files were used for the first run period. The reconstruction efficiency versus x_F and p_T^2 for the different run periods is shown for $K\pi$ and $K\pi\pi\pi$ in Fig. 5.5. At low x_F, the reconstruction efficiencies are approximately equal although the efficiency for the first period is slightly lower due to the inefficient silicon plane. At high x_F, the reconstruction efficiency is very dependent on the run period as expected from the drift chamber hole. The p_T^2 reconstruction efficiency is the same shape for all run periods with different normalizations due to the x_F integration.

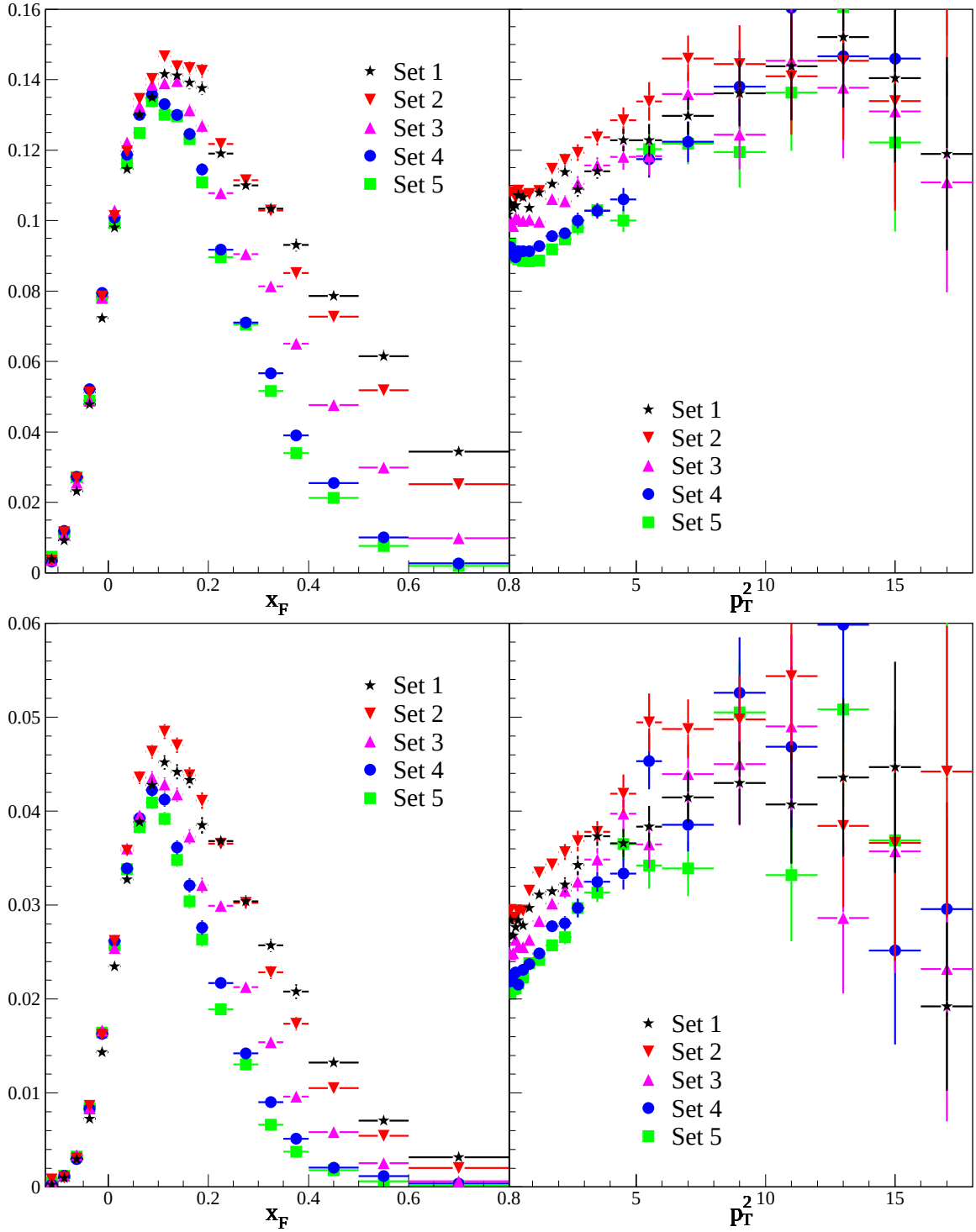

Fig. 5.5.— $K\pi$ (top) and $K\pi\pi\pi$ (bottom) reconstruction efficiency versus x_F (left) and p_T^2 (right) for the five run periods.

5.3.4 Applying the Reconstruction Efficiency

The reconstruction efficiency is calculated separately for all five run periods and two releases. These 10 efficiencies are calculated using the full weighting function described in Section 5.3.2. The data yields are calculated separately for the Release 5 and Release 7 data but integrated over the five run periods as shown in Figures 4.6– 4.13. To calculate the correct acceptances for each of the Release 5 and Release 7 data samples, we first determine what percentage of the data is in each run period (separately for the Release 5 and Release 7 data). These percentages are then used to weight the calculated efficiencies to obtain an overall efficiency (for each Release). The data fractions (weights) are given in Table 5.2. Thus, if the reconstruction efficiency for run period i is ϵ_i, then, using the numbers from Table 5.2, the reconstruction efficiency for Release 5 is $0.0609\epsilon_1 + 0.2230\epsilon_2 + 0.2647\epsilon_3 + 0.2013\epsilon_4 + 0.2501\epsilon_5$.

Run Period	Run Numbers	Release 5	Release 7
1	678-959	6.09%	45.22%
2	960-1123	22.30%	11.40%
3	1124-1288	26.47%	4.77%
4	1289-1482	20.13%	27.13%
5	1483-1606	25.01%	11.48%

Table 5.2: Percentage of data for each of the five run periods divided by release. These numbers are for the Sample B data which is used to obtain the cross sections. Sample B is composed of good, five-target, E_T triggered, filtered data with good scaler information.

Chapter 6

Results and Systematic Errors

The results are obtained by correcting the data from Section 4.3 with the acceptance found in Chapter 5. This is described in detail in Section 6.1. The systematic errors associated with the cross section calculation are found in Section 6.2. The final results, and comparisons to theory, are described in Section 6.3.

6.1 Cross Section Definition and Calculation

In classical mechanics, the differential scattering cross section, $\sigma(\Omega)$, is defined by[32]

$$\sigma(\Omega)\, d\Omega \;=\; \frac{\text{number of particles scattered into solid angle } d\Omega \text{ per unit time}}{\text{incident intensity}}. \quad (6.1)$$

The total scattering cross section is obtained by integrating over all solid angles. The concept of cross section can be extended from scattering to any kind of interaction such as charm production. Scattering or particle production from a combination of identical targets should scale as some power of the number of targets. For atomic nuclei, the number of targets is simply the atomic mass, A, so the total cross section

should be

$$\sigma_A \;=\; \sigma_0\, A^{\alpha} \tag{6.2}$$

where σ_0 is a constant. A spherical nucleus implies that processes which scatter off nuclei should have $\alpha = 2/3$ because the cross sectional area increases as r^2 while the volume increases as r^3. In fact, for the total inelastic nucleon-nucleus cross section, $\alpha \simeq 0.71$[14]. Since the distance scale and momentum transfer scale are inversely related and the total inelastic cross section comes mostly from low momentum transfer processes, it only probes the nucleus as a whole. Charm production, on the other hand, involves much higher momentum transfer and therefore the distance resolution is much smaller. At the momentum transfers typical of charm production, the distance scales are small enough to resolve individual nucleons and, ultimately, partons. Therefore, the "nuclear shadowing" which makes α less than one is greatly reduced and the cross section simply increases linearly as the number of targets (A) increases. The E769 collaboration has verified that $\alpha = 1$ for charm production[13] and this is assumed throughout the rest of this thesis. To normalize the cross section we use the per-nucleon cross section, σ, defined as

$$\sigma \;=\; \frac{\sigma_A}{A} \;=\; \sigma_0 A^{\alpha-1} \;\underset{\alpha\to 1}{=}\; \sigma_0 \tag{6.3}$$

The D^0 total production cross section from π^-–nucleon interactions can be written as

$$\sigma(\pi^- N \;\to\; D^0 X) \;=\; \frac{N_{prod}(D^0)}{T_N\, N_{\pi^-}} \tag{6.4}$$

where

$N_{prod}(D^0)$ = number of D^0 particles produced,

T_N = nucleons/area in the target, and

N_{π^-} = number of incident π^- particles while the experiment is live.

We obtain $N_{prod}(D^0)$ from two sources, $D^0 \to K\pi$ and $D^0 \to K\pi\pi\pi$, as follows

$$N_{prod}(D^0) \;=\; \frac{N_{rec}(D^0 \to Kn\pi)}{B(D^0 \to Kn\pi)\,\epsilon_{trig}\,\epsilon_{rec}(D^0 \to Kn\pi)} \tag{6.5}$$

where

$N_{rec}(D^0 \to Kn\pi)$ = number of reconstructed $D^0 \to Kn\pi$ decays from Section 4.3,

$B(D^0 \to Kn\pi)$ = branching ratio for the $D^0 \to Kn\pi$ decay from the PDG [31] ($B(D^0 \to K\pi) = (3.85 \pm 0.09)\%$ and $B(D^0 \to K\pi\pi\pi) = (7.6 \pm 0.4)\%$),

ϵ_{trig} = trigger efficiency from Section 5.2 = $68.3 \pm 4.4\%$, and

$\epsilon_{rec}(D^0 \to Kn\pi)$ = $D^0 \to Kn\pi$ reconstruction efficiency described in Section 5.3 and is approximately 10.5% (3%) for $K\pi$ ($K\pi\pi\pi$) decays of D^0 particles produced at x_F>0.

The number of incident π^- particles during the experiment livetime, N_{π^-}, is obtained directly from the scalers as described in Section 2.5 and 5.1. For reference, $N_{\pi^-} = 1.00 \times 10^{12}$, and the experiment livetime, although not used, was 50% with a run-by-run root-mean-square (RMS) variation of 5%. The number of nucleons/area in the target, T_N, can be calculated by

$$T_N \;=\; \sum_i \rho_i\, t_i\, N_A \;=\; \sum_i \frac{m_i\, 4}{\pi\, d_i^2\, t_i}\, t_i\, N_A \;=\; \frac{4\, N_A}{\pi} \sum_i \frac{m_i}{d_i^2}. \tag{6.6}$$

Using the target information from Table 2.1 and the known value of Avogadro's number, N_A, we find $T_N = 1.224 \pm 0.004 \times 10^{-6}$ nucleons/μb (μb = microbarn $\equiv 10^{-30}$ cm^2). Substituting Equation 6.5 into Equation 6.4 we obtain the total single inclusive cross section formula below.

$$\sigma(\pi^- N \;\to\; D^0 X) \;=\; \frac{N_{rec}(D^0 \to Kn\pi)}{N_{\pi^-}\; T_N\, B(D^0 \to Kn\pi)\,\epsilon_{trig}\,\epsilon_{rec}(D^0 \to Kn\pi)} \tag{6.7}$$

The calculation of the x_F (p_T^2) differential cross sections are identical to Equation 6.7 except that $\sigma(\pi^- N \to D^0 X)$, $N_{rec}(D^0 \to Kn\pi)$ and $\epsilon_{rec}(D^0 \to Kn\pi)$ become functions of x_F (p_T^2). This gives the differential forms,

$$\frac{d\sigma(\pi^- N \to D^0 X\ ;\ x_F)}{dx_F} = \frac{N_{rec}(D^0 \to Kn\pi\ ;\ x_F)}{N_{\pi^-}\ T_N\ B(D^0 \to Kn\pi)\,\epsilon_{trig}\,\epsilon_{rec}(D^0 \to Kn\pi\ ;\ x_F)} \tag{6.8}$$

and

$$\frac{d\sigma(\pi^- N \to D^0 X\ ;\ p_T^2)}{dp_T^2} = \frac{N_{rec}(D^0 \to Kn\pi\ ;\ p_T^2)}{N_{\pi^-}\ T_N\ B(D^0 \to Kn\pi)\,\epsilon_{trig}\,\epsilon_{rec}(D^0 \to Kn\pi\ ;\ p_T^2)} \tag{6.9}$$

6.2 Systematic Errors

Systematic errors must be determined for every entry Eqs. 6.7, 6.8, and 6.9. Since the quantities N_{π^-}, T_N, $B(D^0 \to Kn\pi)$, and ϵ_{trig} are independent of x_F and p_T^2 for E791, errors in these quantities cannot affect the shape of the differential distributions, only the overall normalization. The quantities $N_{rec}(D^0 \to Kn\pi)$ and ϵ_{rec} depend on x_F and p_T^2 and can therefore affect the shape of the differential distributions as well as the overall normalization. The causes and evaluation of the important systematic errors are described below.

6.2.1 Systematic Errors Affecting Only the Normalization

As mentioned above, the variables N_{π^-}, T_N, $B(D^0 \to Kn\pi)$, and ϵ_{trig} only affect the overall normalization. The errors on T_N, $B(D^0 \to Kn\pi)$, and ϵ_{trig} are all given in Section 6.1. Combining the two errors which are independent of mode (T_N and ϵ_{trig}) we obtain a relative error of

$$\sqrt{\left(\frac{0.004}{1.224}\right)^2 + \left(\frac{4.4}{68.3}\right)^2} = 6.45\% \tag{6.10}$$

The determination of N_{π^-}, the total number pions able to trigger the experiment during the experiment livetime, is described in Section 5.1. Since all the scaler quantities

used in this analysis count only during the experiment livetime, no deadtime correction is necessary. In addition, since the trigger counter used to count the pions is also a requirement in the trigger, any efficiency errors will cancel out. Also, problems counting multiple beam particles in one RF bucket are eliminated by vetoing those events (which moves the systematic errors to ϵ_{trig}). Therefore, the only error on N_{π^-} is the statistical error which is negligible.

6.2.2 Systematic Errors for $N_{rec}(D^0 \rightarrow Kn\pi)$

The method used to measure the amount of signal in each bin of x_F and p_T^2 is described in detail in Chapter 4. The determination of signal size comes from a fit to a normalized or invariant mass plot with a fixed-width, fixed-mean Gaussian function used to represent the signal. The fixed values of the mass and width are obtained as a function of x_F and p_T^2 by drawing a smooth curve through the measured masses and widths. The measured masses and widths are obtained from a slightly ($\sim$10%) larger data sample. This, combined with the smoothing procedure, helps to eliminate statistical fluctuations. To estimate the systematic error from the fitting procedure we refit after changing the width by $\pm \sim 1\ \sigma$.

6.2.3 Systematic Errors for ϵ_{rec}

The systematic errors associated with ϵ_{rec} come from a lack of agreement between the Monte Carlo simulation and the real data. These errors can come from inaccuracies in the charm particle production (Sections 6.2.3.1 and 6.2.3.2) and an incorrect simulation of the detector response (Section 6.2.3.3).

6.2.3.1 Monte Carlo Production

As mentioned in Section 5.3.2, two different sets of Monte Carlo events were generated for each of the decay modes labeled MC1 and MC2. After generating the MC1 events we found that the Monte Carlo gave a particularly poor p_T^2 distribution relative to the data. The Monte Carlo p_T^2 was much softer than the data. Although the Monte Carlo weighting technique (Section 5.3.2) allows us to correct for the discrepancy, the high p_T^2 statistics were poor. Therefore we attempted to generate another set of Monte Carlo events with higher p_T^2. This proceeded in several iterations as it was learned that other variables were affecting the D^0 acceptance. We found that even after weighting both sets of Monte Carlo events by D^0 x_F, D^0 p_T^2, and PT715, we still had a large ($\sim$10%) discrepancy in acceptance between them. An effort was made to look for the cause of this difference. A large number of variables were compared between data and Monte Carlo generated with different input values for the physics parameters. The problem appeared to be related to the p_T distribution of the non-D tracks in a way that was not accounted for by the PT715 weighting. Our "solution" to this problem was to generate Monte Carlo with measured variables approximately as wrong as the original Monte Carlo (compared to the data) but in the opposite direction. The result is MC2. The adjusted PYTHIA/JETSET parameters are shown in Table 6.1 and the average values for the various physics variables are shown in Table 6.2. The acceptance we take to be the average of the acceptances from MC1 and MC2 with a systematic error equal to half the difference.

6.2.3.2 Monte Carlo Weighting

The procedure used to weight the Monte Carlo events was described in Section 5.3.2. As mentioned in Section 5.3.2, there were two results for the weighting

PYTHIA/JETSET Parameter	MC1	MC2
parp(91) $\equiv$ primordial parton $\sqrt{<k_t^2>}$ (GeV/c)	0.44	1.00
parp(93) $\equiv$ limit of primordial parton k_t (GeV/c)	2.0	4.0
parj(21) $\equiv \sigma_{px,py}$ of quarks popped during fragmentation (GeV/c)	0.36	0.60
parp(82) $\equiv p_T$ lower limit on multiple interactions (GeV/c)	1.55	1.35
parj(42) $\equiv b$ parameter of Lund fragmentation function (Eq. 1.7)	0.36	0.30

Table 6.1: Comparison of PYTHIA/JETSET parameters for MC1 and MC2. Increasing the first three parameters increases p_T (and decreases multiplicity); decreasing the last two parameters increases multiplicity.

Physics Variable	Data	MC1	MC2
Number of category 0 tracks	5.75	6.17	6.13
Number of category 1 tracks	1.70	1.49	1.41
Number of category 3 tracks	3.21	3.14	3.08
Number of category 7 tracks	2.92	2.24	2.24
Number of category 15 tracks	6.53	6.26	6.62
Primary multiplicity	7.24	6.83	7.10
<PT715> (GeV/c)	.426	.399	.483
<p> of primary tracks (GeV/c)	19.3	17.8	20.5
$\sigma_{z_{pri}}$ (μm)	223	252	219
$\sigma_{z_{pri}}$ ($z_{pri} > -7.4$) (μm)	204	214	186
$\sigma_{z_{sec}}$ (μm)	292	314	312
$\sigma_{z_{sec}}$ ($z_{pri} > -7.4$) (μm)	269	277	276
$\sigma_{\Delta Z}$ (μm)	381	420	396
$\sigma_{\Delta Z}$ $z_{pri} > -7.4$ (μm)	350	366	347
Average D^0 x_F	.103	.116	.113
Average D^0 p_T^2 (GeV^2/c^2)	1.53	0.95	1.31

Table 6.2: Comparison of background-subtracted data to MC1 and MC2 for various variables. The track categories are defined on p. 46. σ_x is the calculated error on x. The cut $z_{pri} > -7.4$ eliminates primaries in the platinum target.

procedure. Since each result is only an approximation to the true result, we use the difference as one measure of the systematic error associated with the weighting. We also vary the lifetime weighting by $\tau = 0.413 \pm 0.003$ ps. This lifetime and error is obtained by combining the E687 result ($0.413 \pm 0.004 \pm 0.003$ ps)[33] with the preliminary E791 measurement ($0.413 \pm 0.003 \pm 0.003$ ps)[34].

6.2.3.3 Tracking and Vertexing Efficiency

One measure of our understanding of the efficiency of the tracking and vertexing systems and algorithms is given by the ratio of the $K\pi\pi\pi$ branching ratio to the $K\pi$ branching ratio. The reconstruction efficiency, ϵ_{rec} should depend on ϵ_{track}^n where ϵ_{track} is the tracking efficiency and n is the number of decay tracks. Therefore, the amount by which we miss the correct ratio of branching ratios gives us a handle on ϵ_{track}^2 which gives us a normalization error. We can also examine the ratio of branching ratios versus x_F and p_T^2 to determine the error on the shape. These are shown in Figures 6.1 and 6.2. The errors shown include both statistical and mode-independent systematic errors, described in Section 6.3.1. It is clear that the data are consistent with a flat line whose value falls within the range given by the PDG [31] value (1.96 ± 0.09). However, the x_F distribution is also consistent with a deviation from the PDG value above x_F of 0.25, probably due to our modeling of the drift chamber hole (described in Sections 2.3.3.2 and 5.3.3). Fitting the range below and above 0.25 separately, we obtain values of 2.02 and 1.70, respectively. Since the value below 0.25 is consistent with flat and the PDG value, we assign no systematic error for the shape, but we do include a normalization systematic error equal to the PDG value error because this is the best we can know the agreement on the normalization. For the region above 0.25 we assign an error of $(2.02 - 1.70)/(\frac{1}{2}(2.02 + 1.70)) = \pm 17.2\%$ to account for the

discrepancy between the low x_F and high x_F data. For the p_T^2 distribution there is a slight dependence on p_T^2 below 0.4 (GeV/c)^2. Half the full range of values below 0.4 (GeV/c)^2 (1.86–2.32) is used to obtain an additional systematic error of $\pm 11\%$ for the low p_T^2 region. Although this error may not come from tracking and vertexing, it does represent an uncertainty in our knowledge of the p_T^2 shape. Since no discernible dependence on p_T^2 is seen above 0.4 (GeV/c)^2, we assign no additional error on the shape. The normalization error on the p_T^2 distribution will include an error due to the discrepancy between the fitted value (2.08) and the PDG value (1.96). This error is $\pm(2.08 - 1.96)/(\frac{1}{2}(2.08 + 1.96)) = \pm 5.9\%$.

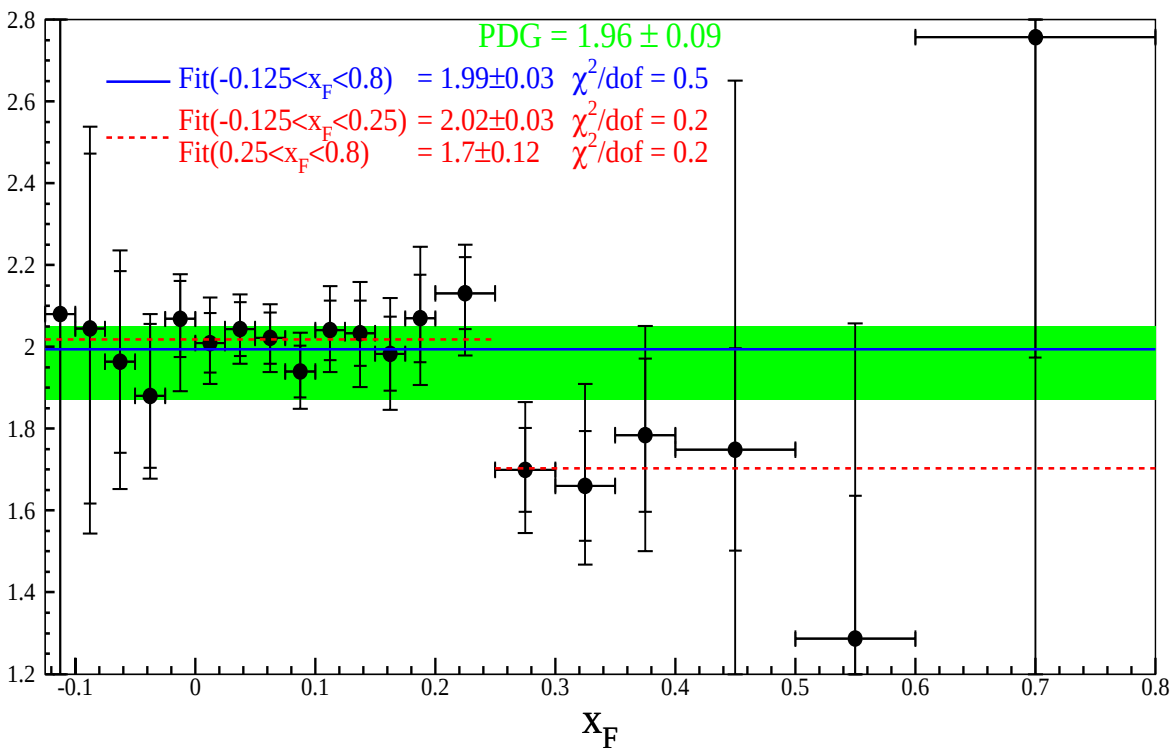

Fig. 6.1.— $K\pi\pi\pi$ to $K\pi$ measured branching ratio vs. x_F. The inner error bars are statistical only, the outer error bars are statistical and mode-independent systematic errors combined in quadrature. The shaded region is the PDG [31] value for the branching ratio. The solid line is a flat line fit to the entire x_F range. The dashed line is two flat line fits, one for the range -0.125<x_F<0.25 and the other for the range 0.25<x_F<0.8.

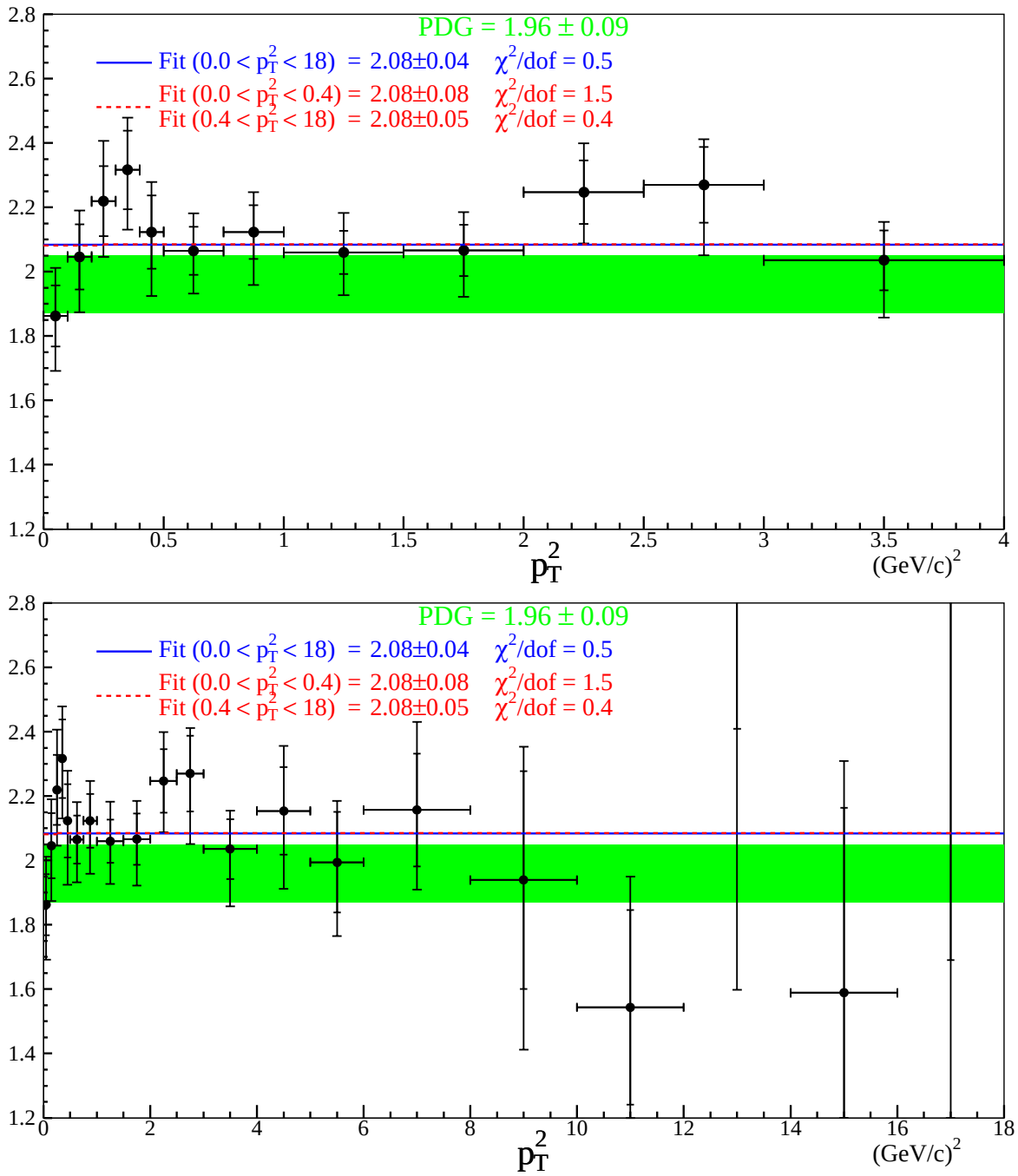

Fig. 6.2.— $K\pi\pi\pi$ to $K\pi$ measured branching ratio vs. p_T^2. The inner error bars are statistical only, the outer error bars are statistical and mode-independent systematic errors combined in quadrature. The shaded region is the PDG [31] value for the branching ratio. The solid line is a flat line fit to the entire p_T^2 range. The dashed line is two flat line fits, one for the range $0.0<p_T^2<0.4$ (GeV/c)^2 and the other for the range $0.4<p_T^2<18.0$ (GeV/c)^2.

The systematic error due to the drift chamber hole is also estimated by using data which are less affected by the DC hole. We do this by eliminating varying amounts of the data recorded late in the run for different regions of high x_F. Recalculating without these data gives another indication of the systematic error.

6.3 Results and Comparisons

The fully corrected p_T^2 and x_F differential cross sections are presented in Section 6.3.1 with the calculated systematic errors. To facilitate comparisons, fits to the differential distributions are made using functional forms with few free parameters. Then a comparison of the shape parameter(s) can easily be made without regard to bin sizes or normalizations. The shape parameters are compared to predictions from the next-to-leading order (NLO) QCD calculation by Mangano, Nason and Ridolfi (MNR) and PYTHIA/JETSET; both are described in Section 1.3. Comparisons are also made to previous π^-–nucleon charm production experiments. In addition, we make direct comparisons between data, MNR NLO, and PYTHIA/JETSET histograms.

6.3.1 Combining the Errors

The errors from Section 6.2.1 which affect only the normalization are easy to incorporate. These errors will be listed separately as normalization errors for the x_F and p_T^2 distributions and added in quadrature with other systematic errors to obtain the total cross section systematic error. The remaining systematic errors which can affect both the shape and the normalization are more difficult to incorporate. The basic idea of determining the systematic error will be to take all combinations of the x_F and p_T^2 distributions which are consistent with what we believe to be the truth and select the extremes from these distributions. However, for the differential cross

sections, we are primarily interested in the error on the shape; the normalization error will be noted separately. We now describe the method we use to accomplish this.

First a fully corrected base distribution is chosen which we believe to be the best representation to the true distribution. A distribution is defined by the data ($N_{rec}(D^0 \to Kn\pi)$) and the acceptance (ϵ_{rec}) for each of the two decay modes. All of the data are required to be from Sample B, that is, no four-target data, no interaction-trigger data, no data with missing or inaccurate scalers and no events with a primary vertex consistent with being in the platinum target. The base data are required to pass the standard cuts listed in Tables 3.2, 3.3, and 3.4. The $K\pi$ and $K\pi\pi\pi$ x_F base data set is data from the first 100% (60%) for x_F less than (greater than) 0.4. Fits are performed on the normalized (invariant) mass for x_F less than (greater than) 0.2 using a fixed mass and width Gaussian function to represent the signal. The $K\pi$ data are fit with quadratic, cubic, and exponential background functions for x_F in the range -0.125–0.2, 0.2–0.5, and 0.5–0.8. The $K\pi\pi\pi$ data background functions are linear for -0.125<x_F<-0.1 and quadratic for all other x_F bins. The p_T^2 base data are from 100% of the Sample B data with an x_F>0 requirement. The fits are made to the normalized mass with a fixed mass and width Gaussian signal function and a quadratic (linear) background function for p_T^2 less than (greater than) 12 (GeV/c)^2. The base acceptance is the average of the acceptances from MC1 and MC2, both fully weighted (including the correlations weighting and run weighting). The Monte Carlo data are fit with a fixed mass and width Gaussian signal and a linear (quadratic) background for the $K\pi$ ($K\pi\pi\pi$) data. The normalized mass and invariant mass are used in the same kinematic regions as for the real data. The base distributions are obtained by dividing the base data by the base acceptance. Other distributions are generated by varying the data and/or the acceptance. These non-

base distributions will be called systematic distributions. Variations of the data are obtained by using different background functions (linear for $K\pi$ and Gaussian for $K\pi\pi\pi$) and using a fixed mass and width but varying the width $\pm 1\sigma$. There is no correlation between the $K\pi$ and $K\pi\pi\pi$ modes due to these variations. Therefore, we apply these systematic errors to the individual $K\pi$ and $K\pi\pi\pi$ distributions and call them *uncorrelated* systematic errors. Another uncorrelated error also comes from the choice of fitting function, in this case, the background function for the Monte Carlo data. The $K\pi$ ($K\pi\pi\pi$) background function is varied from a linear (quadratic) function to a quadratic (Gaussian) function. Also included in the uncorrelated errors is a different set of cuts, which increases SDZ by $4\sigma_z$. The maximum and minimum values for each bin of x_F and p_T^2 from all of the systematic distributions are recorded. These are the upper and lower limits of the uncorrelated systematic errors. In Figures 6.3–6.6 the corrected x_F and p_T^2 distributions are shown for $K\pi$ and $K\pi\pi\pi$. The inner error bars are the statistical errors and the outer error bars are the quadratic sum of the statistical errors and the uncorrelated systematic errors. The variations used to obtain the systematic distributions includes all combinations of variations, not only individual variations from the base distribution. For example, a systematic distribution with the widths increased by 1σ *and* a different background function is included as well as systematic distributions with only the widths increased by 1σ and only a different background function.

At this point, the remaining systematic errors affect both the $K\pi$ and $K\pi\pi\pi$ data sets. Therefore, we combine the $K\pi$ and $K\pi\pi\pi$ data and look at the effect on the combined (D^0) sample. To combine the data samples we would like to weight the samples bin-by-bin by the inverse of their errors. As can be seen from Figures 6.3–6.6, the errors have become asymmetric, complicating this process. The bin-by-bin weight

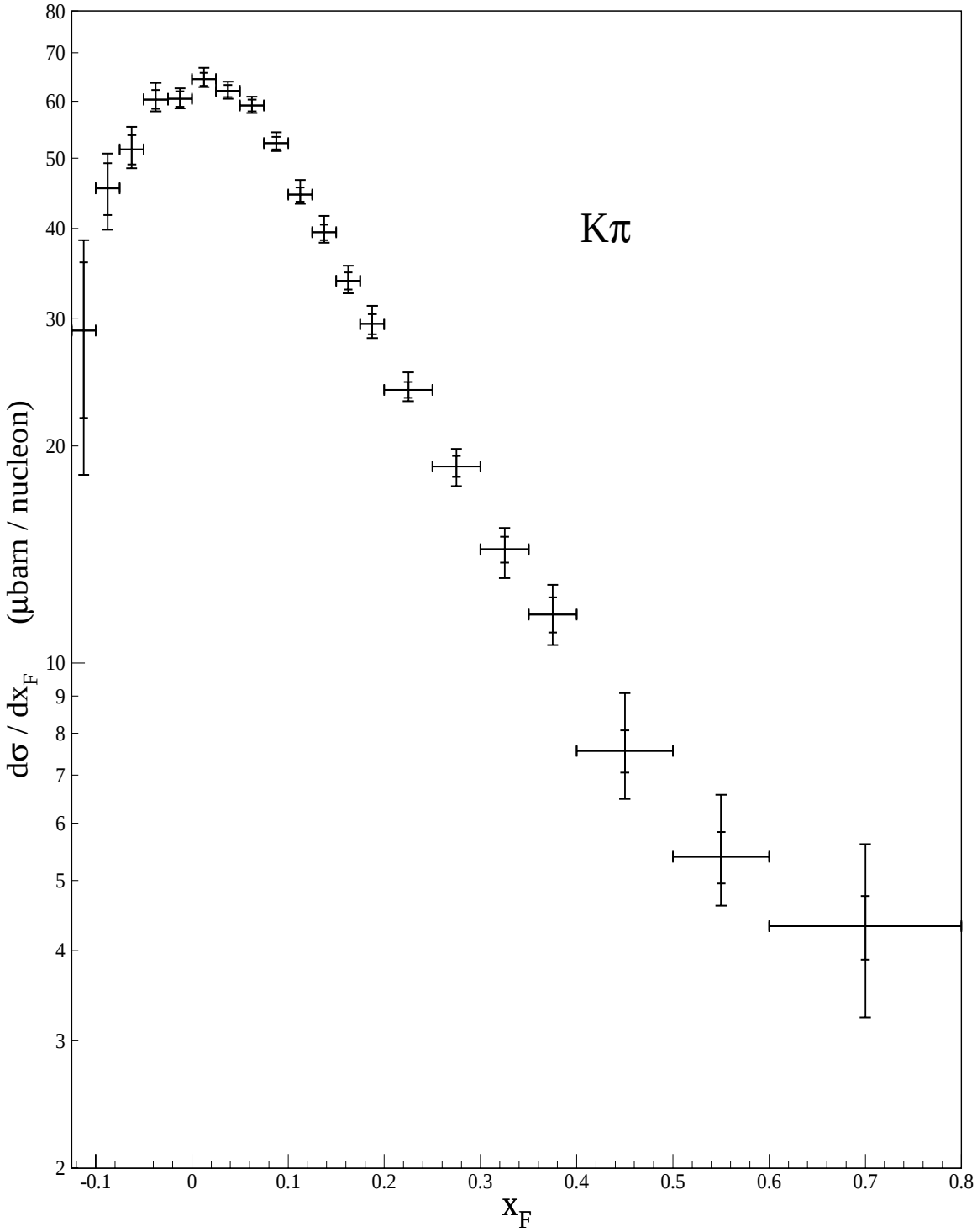

Fig. 6.3.— $K\pi$ fully corrected x_F differential cross section. The inner error bars show the statistical errors only. The outer error bars show the quadratic sum of the statistical errors and the $K\pi$-only systematic errors.

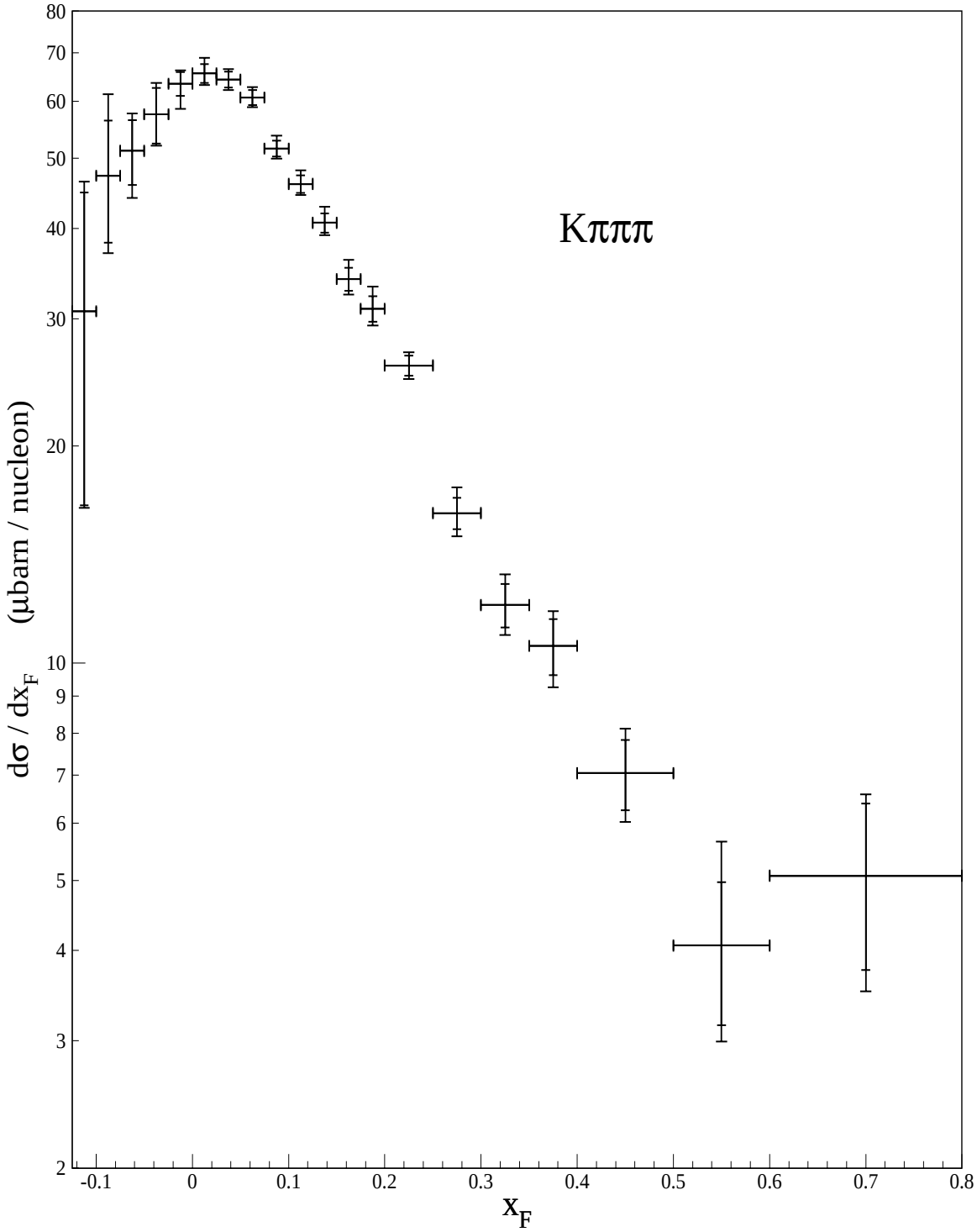

Fig. 6.4.— $K\pi\pi\pi$ fully corrected x_F differential cross section. The inner error bars show the statistical errors only. The outer error bars show the quadratic sum of the statistical errors and the $K\pi\pi\pi$-only systematic errors.

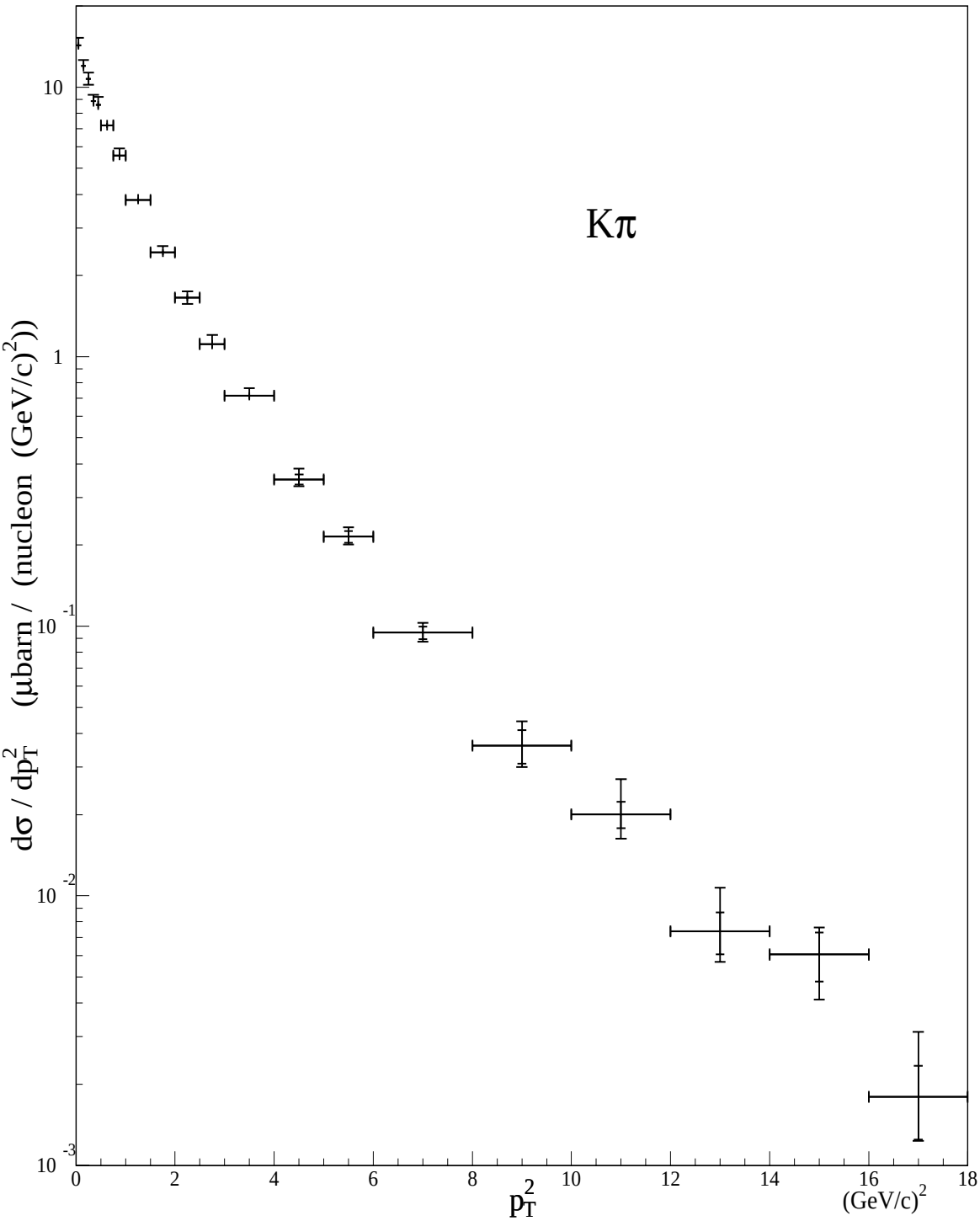

Fig. 6.5.— $K\pi$ fully corrected p_T^2 differential cross section. The inner error bars show the statistical errors only. The outer error bars show the quadratic sum of the statistical errors and the $K\pi$-only systematic errors.

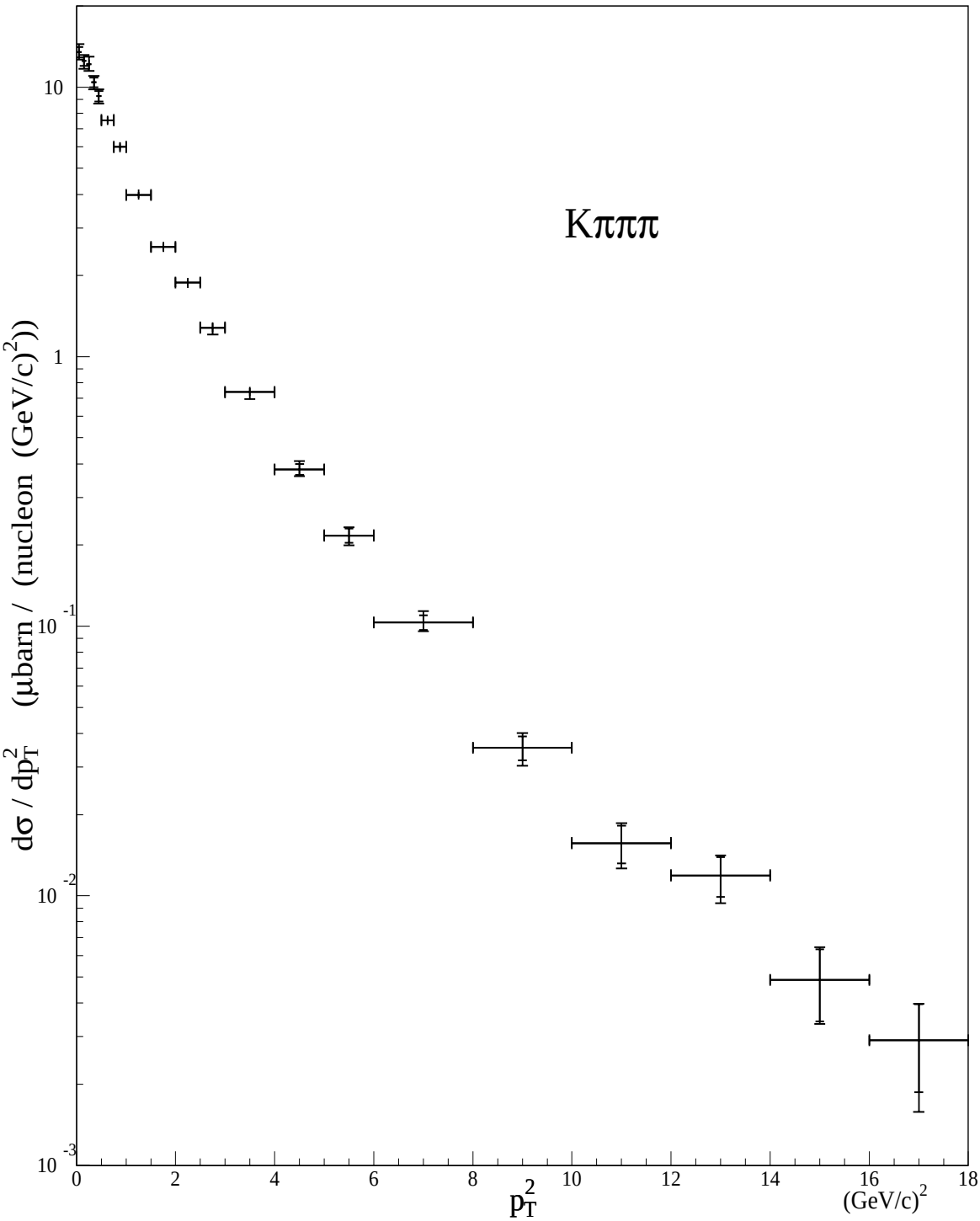

Fig. 6.6.— $K\pi\pi\pi$ fully corrected p_T^2 differential cross section. The inner error bars show the statistical errors only. The outer error bars show the quadratic sum of the statistical errors and the $K\pi\pi\pi$-only systematic errors.

used to combine the samples is the inverse of the average of the positive and negative errors for each bin. The positive (negative) error of the combined data is the quadratic sum of the positive (negative) errors of the individual samples, weighted the same way as the central value. That is, for each bin in x_F and p_T^2,

$$N_{D^0} = \frac{N_{K\pi}W_{K\pi} + N_{K\pi\pi\pi}W_{K\pi\pi\pi}}{W_{K\pi} + W_{K\pi\pi\pi}} \tag{6.11}$$

$$\sigma^+_{N_{D^0}} = \frac{\sqrt{\left[\sigma^+_{N_{K\pi}}W_{K\pi}\right]^2 + \left[\sigma^+_{N_{K\pi\pi\pi}}W_{K\pi\pi\pi}\right]^2}}{W_{K\pi} + W_{K\pi\pi\pi}} \tag{6.12}$$

$$\sigma^-_{N_{D^0}} = \frac{\sqrt{\left[\sigma^-_{N_{K\pi}}W_{K\pi}\right]^2 + \left[\sigma^-_{N_{K\pi\pi\pi}}W_{K\pi\pi\pi}\right]^2}}{W_{K\pi} + W_{K\pi\pi\pi}} \tag{6.13}$$

where

$$W_{Kn\pi} = 1 \Big/ \left[\frac{\sigma^+_{N_{Kn\pi}} + \sigma^-_{N_{Kn\pi}}}{2}\right]^2 \tag{6.14}$$

and $\sigma^{\pm}_N$ is the $\pm$ error on the signal, N. For each of the remaining systematic errors, we determine the $K\pi$ and $K\pi\pi\pi$ distributions and use the above prescription to obtain the D^0 distribution. The same procedure used to obtain the $K\pi$ and $K\pi\pi\pi$ systematic errors is used to obtain the D^0 systematic errors. Various factors involved in the reconstruction efficiency are changed and the maximum and minimum points of the resulting systematic distributions are found for each bin of x_F and p_T^2. In this case, however, the systematic distributions are normalized to the base distribution before finding the maximum and minimum values. This is because the systematic errors considered here can only affect the entire data sample, not just an individual bin of x_F or p_T^2. The varied factors are the run weighting, the kinematic weighting and the type of Monte Carlo used (MC1 or MC2). Again, all combinations of these variations are also included. The maximum and minimum points give the D^0 systematic

errors which are added in quadrature with the errors obtained from equations 6.12 and 6.13. The results are shown in Figures 6.7 and 6.8 where the inside error bars are the errors obtained from equations 6.12 and 6.13 and the outside error bars are these errors added in quadrature to the D^0 systematic errors. The normalization error on these measurements comes from two sources. The first comes from finding the maximum and minimum values used to normalize the systematic distributions to the base distribution. In addition to all of the variations mentioned above, the branching ratios to $K\pi$ and $K\pi\pi\pi$ are varied within their errors. The complete range of normalization values is $^{+6.4}_{-7.5}\%$ for the x_F distribution and $^{+5.8}_{-11.9}\%$ for the p_T^2 distribution. The second source of normalization error is the $\pm 6.5\%$ from Eq. 6.10. The last source of normalization error, discussed Section 6.2.3.3, is due to tracking and vertexing which is 4.6% for x_F and 5.9% for p_T^2. Adding the normalization errors in quadrature gives us an overall normalization error of $^{+10.2}_{-10.9}\%$ for the x_F distribution and $^{+10.5}_{-14.8}\%$ for the p_T^2 distribution.

6.3.2 D^0 x_F and p_T^2 Differential Cross Sections

The fully corrected x_F distributions from Figures 6.3, 6.4, and 6.7 are tabulated in Table 6.3. The fully corrected p_T^2 distributions from Figures 6.5, 6.6, and 6.8 are tabulated in Table 6.4

As discussed in Section 1.3 we would like to compare the data to theoretical predictions from PYTHIA/JETSET and Mangano, Nason and Ridolfi's next-to-leading-order (MNR NLO) calculation. Unfortunately, as mentioned in the Introduction, calculations in QCD are often quite difficult and fraught with many uncertainties. It is more accurate to think of these "theories" as models. Both of these models have many free parameters which can be adjusted. Therefore, it is more likely that the data

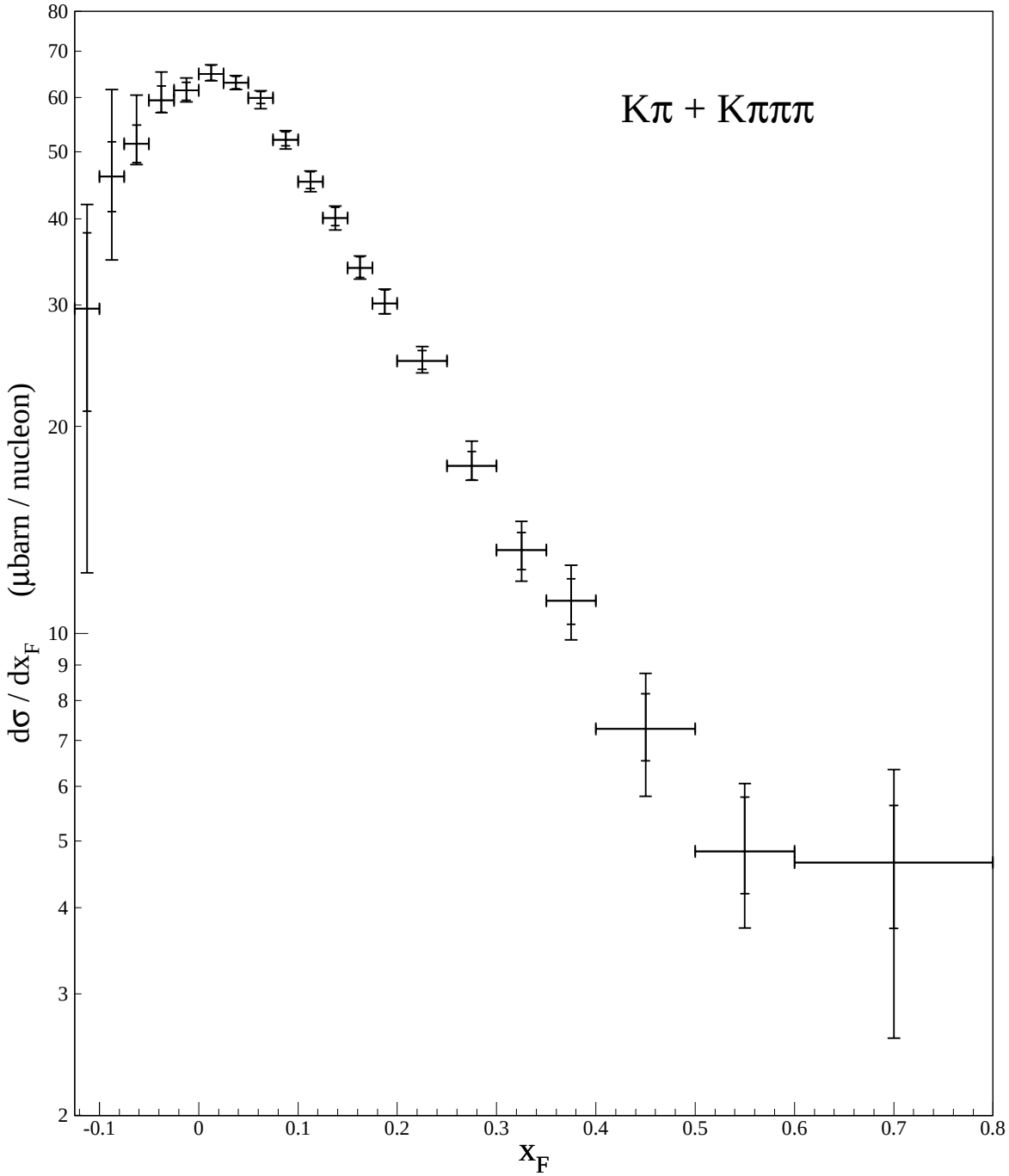

Fig. 6.7.— D^0 fully corrected x_F differential cross section obtained from adding the $K\pi$ and $K\pi\pi\pi$ modes weighting by the total errors shown in Figures 6.3 and 6.4. The inner error bars show the $K\pi$ and $K\pi\pi\pi$ statistical and systematic errors only. The outer error bars show the quadratic sum of the $K\pi$ and $K\pi\pi\pi$ statistical and systematic errors and the systematic errors which are common to the $K\pi$ and the $K\pi\pi\pi$ results. These errors do not include a normalization error of $^{+10.2}_{-10.9}\%$.

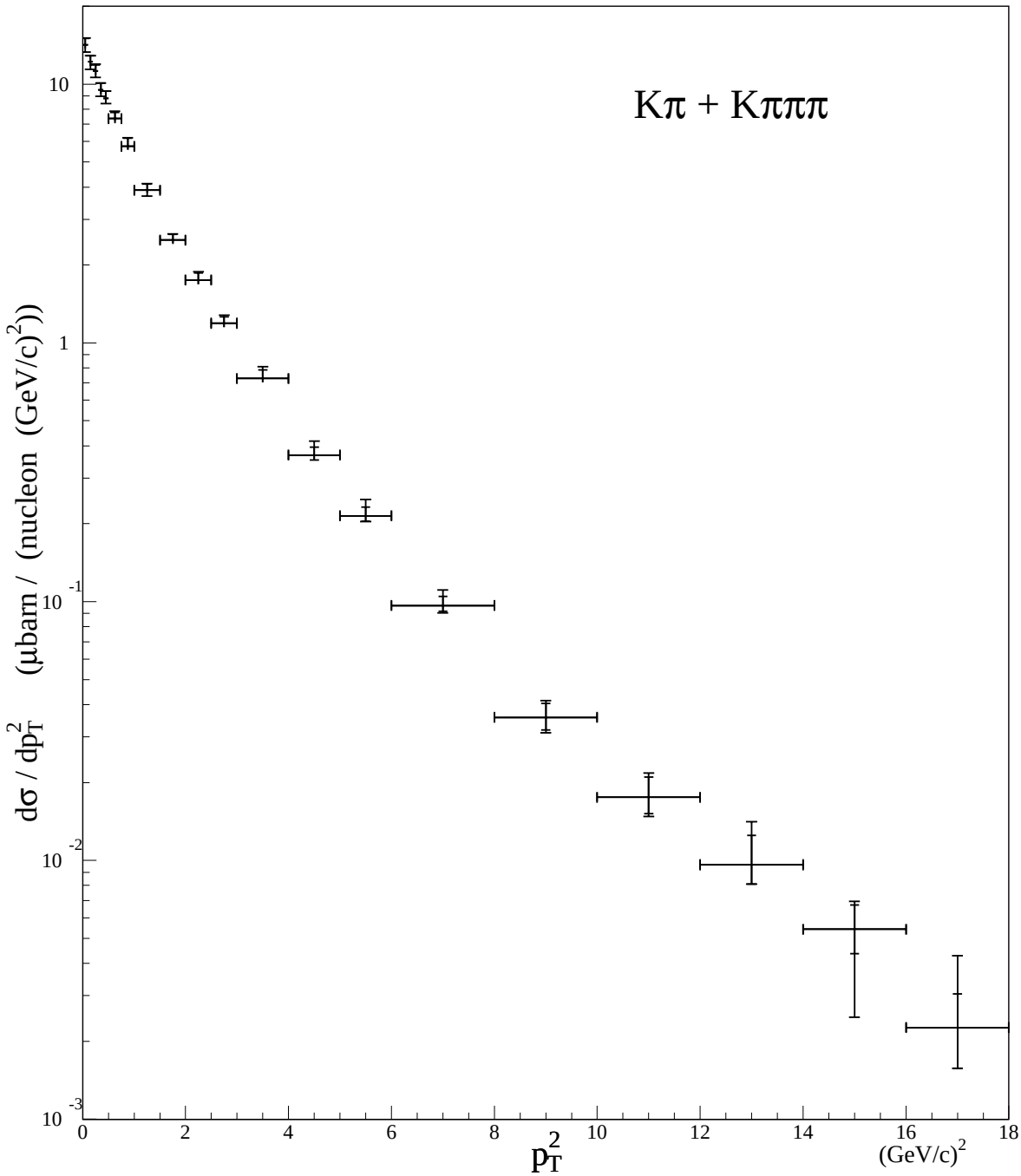

Fig. 6.8.— D^0 fully corrected p_T^2 differential cross section obtained from adding the $K\pi$ and $K\pi\pi\pi$ modes weighting by the total errors shown in Figures 6.5 and 6.6. The inner error bars show the $K\pi$ and $K\pi\pi\pi$ statistical and systematic errors only. The outer error bars show the quadratic sum of the $K\pi$ and $K\pi\pi\pi$ statistical and systematic errors and the systematic errors which are common to the $K\pi$ and the $K\pi\pi\pi$ results. These errors do not include a normalization error of $^{+10.5}_{-14.8}\%$.

x_F Range	Cross Section (μbarns / nucleon)		
	$K\pi$	$K\pi\pi\pi$	D^0
-0.125 < x_F < -0.100	$28.6 \pm 6.9^{+5.1}_{-7.9}$	$30.1 \pm 13.9^{+4.1}_{-1.7}$	$29.0^{+7.5}_{-8.5}{}^{+8.9}_{-10.9}$
-0.100 < x_F < -0.075	$45.1 \pm 3.7^{+3.7}_{-4.3}$	$46.7 \pm 9.0^{+3.5}_{-4.5}$	$45.4^{+4.6}_{-4.9}{}^{+4.9}_{-6.9}$
-0.075 < x_F < -0.050	$51.0 \pm 2.4^{+2.9}_{-1.7}$	$50.7 \pm 5.2^{+3.7}_{-4.8}$	$50.9^{+3.3}_{-2.7}{}^{+2.9}_{-2.6}$
-0.050 < x_F < -0.025	$59.8 \pm 1.8^{+2.5}_{-1.3}$	$56.9 \pm 5.0^{+2.6}_{-1.9}$	$59.2^{+2.7}_{-2.1}{}^{+3.2}_{-2.8}$
-0.025 < x_F < 0.000	$60.0 \pm 1.4^{+1.4}_{-1.0}$	$62.8 \pm 2.4^{+1.4}_{-4.3}$	$60.5^{+1.7}_{-1.7}{}^{+3.4}_{-2.9}$
0.000 < x_F < 0.025	$63.8 \pm 1.3^{+1.7}_{-0.9}$	$65.0 \pm 1.9^{+2.5}_{-1.4}$	$64.2^{+1.8}_{-1.3}{}^{+3.0}_{-3.0}$
0.025 < x_F < 0.050	$61.6 \pm 1.2^{+1.3}_{-0.9}$	$63.7 \pm 1.6^{+1.4}_{-1.0}$	$62.4^{+1.4}_{-1.2}{}^{+2.9}_{-2.9}$
0.050 < x_F < 0.075	$58.8 \pm 1.1^{+1.2}_{-0.8}$	$60.2 \pm 1.5^{+1.4}_{-1.0}$	$59.4^{+1.3}_{-1.1}{}^{+2.8}_{-2.9}$
0.075 < x_F < 0.100	$52.2 \pm 1.0^{+1.5}_{-0.8}$	$51.2 \pm 1.3^{+1.7}_{-1.0}$	$51.8^{+1.4}_{-1.0}{}^{+2.4}_{-2.5}$
0.100 < x_F < 0.125	$44.3 \pm 1.0^{+1.2}_{-0.8}$	$45.8 \pm 1.3^{+1.6}_{-1.0}$	$44.9^{+1.2}_{-1.0}{}^{+2.1}_{-2.2}$
0.125 < x_F < 0.150	$39.3 \pm 1.0^{+1.8}_{-0.8}$	$40.5 \pm 1.2^{+1.7}_{-1.0}$	$39.8^{+1.5}_{-1.0}{}^{+2.6}_{-1.9}$
0.150 < x_F < 0.175	$33.7 \pm 0.9^{+1.4}_{-0.9}$	$33.8 \pm 1.2^{+1.5}_{-1.1}$	$33.7^{+1.3}_{-1.0}{}^{+1.7}_{-1.6}$
0.175 < x_F < 0.200	$29.3 \pm 0.9^{+1.5}_{-0.9}$	$30.8 \pm 1.2^{+1.8}_{-1.0}$	$29.9^{+1.4}_{-1.0}{}^{+1.5}_{-1.4}$
0.200 < x_F < 0.250	$23.8 \pm 0.6^{+1.2}_{-0.6}$	$25.7 \pm 0.8^{+0.7}_{-0.7}$	$24.8^{+0.9}_{-0.7}{}^{+1.2}_{-1.4}$
0.250 < x_F < 0.300	$18.6 \pm 0.6^{+0.9}_{-1.0}$	$16.0 \pm 0.8^{+0.9}_{-0.8}$	$17.4^{+0.8}_{-0.8}{}^{+2.6}_{-2.5}$
0.300 < x_F < 0.350	$14.3 \pm 0.6^{+0.8}_{-1.1}$	$12.0 \pm 0.8^{+1.2}_{-0.7}$	$13.3^{+0.9}_{-0.9}{}^{+1.9}_{-2.2}$
0.350 < x_F < 0.400	$11.6 \pm 0.7^{+0.9}_{-0.9}$	$10.5 \pm 0.9^{+0.8}_{-0.9}$	$11.1^{+0.8}_{-0.8}{}^{+1.6}_{-1.9}$
0.400 < x_F < 0.500	$7.3 \pm 0.5^{+1.0}_{-3.6}$	$6.4 \pm 0.8^{+0.5}_{-3.0}$	$6.8^{+0.7}_{-2.3}{}^{+1.2}_{-1.3}$
0.500 < x_F < 0.600	$5.0 \pm 0.4^{+0.9}_{-2.4}$	$3.3 \pm 0.8^{+0.7}_{-1.6}$	$4.0^{+0.8}_{-1.5}{}^{+0.9}_{-0.7}$
0.600 < x_F < 0.800	$3.7 \pm 0.4^{+0.5}_{-1.8}$	$5.2 \pm 1.4^{+0.7}_{-2.5}$	$4.1^{+0.6}_{-1.6}{}^{+0.7}_{-1.3}$

Table 6.3: x_F differential cross section for D^0 mesons. The $K\pi$ and $K\pi\pi\pi$ errors are statistical plus uncorrelated systematic errors. The D^0 errors are combined $K\pi$ and $K\pi\pi\pi$ errors plus the remaining, correlated systematic errors. Normalization errors of $^{+10.2}_{-10.9}\%$ are *not* included.

p_T^2 Range	Cross Section (μbarns / (nucleon (GeV/c)^2))		
	$K\pi$	$K\pi\pi\pi$	D^0
$0.00 < p_T^2 < 0.10$	$14.29 \pm 0.37 ^{+0.89}_{-0.32}$	$13.49 \pm 0.59 ^{+0.75}_{-0.59}$	$13.97 ^{+0.70}_{-0.44} ^{+1.52}_{-1.68}$
$0.10 < p_T^2 < 0.20$	$12.00 \pm 0.33 ^{+0.53}_{-0.43}$	$12.51 \pm 0.52 ^{+0.43}_{-0.62}$	$12.20 ^{+0.46}_{-0.46} ^{+1.32}_{-1.49}$
$0.20 < p_T^2 < 0.30$	$10.75 \pm 0.31 ^{+0.49}_{-0.44}$	$12.16 \pm 0.48 ^{+0.66}_{-0.48}$	$11.25 ^{+0.47}_{-0.42} ^{+1.23}_{-1.31}$
$0.30 < p_T^2 < 0.40$	$8.89 \pm 0.28 ^{+0.39}_{-0.29}$	$10.43 \pm 0.44 ^{+0.35}_{-0.43}$	$9.44 ^{+0.37}_{-0.34} ^{+1.02}_{-1.09}$
$0.40 < p_T^2 < 0.50$	$8.61 \pm 0.27 ^{+0.54}_{-0.25}$	$9.26 \pm 0.40 ^{+0.38}_{-0.40}$	$8.89 ^{+0.42}_{-0.32} ^{+0.01}_{-0.34}$
$0.50 < p_T^2 < 0.75$	$7.20 \pm 0.15 ^{+0.32}_{-0.26}$	$7.54 \pm 0.22 ^{+0.18}_{-0.22}$	$7.39 ^{+0.22}_{-0.22} ^{+0.32}_{-0.24}$
$0.75 < p_T^2 < 1.00$	$5.57 \pm 0.13 ^{+0.33}_{-0.16}$	$6.00 \pm 0.19 ^{+0.18}_{-0.19}$	$5.80 ^{+0.22}_{-0.17} ^{+0.11}_{-0.11}$
$1.00 < p_T^2 < 1.50$	$3.81 \pm 0.08 ^{+0.18}_{-0.11}$	$3.98 \pm 0.10 ^{+0.17}_{-0.12}$	$3.89 ^{+0.14}_{-0.10} ^{+0.05}_{-0.20}$
$1.50 < p_T^2 < 2.00$	$2.44 \pm 0.06 ^{+0.12}_{-0.07}$	$2.55 \pm 0.08 ^{+0.08}_{-0.07}$	$2.50 ^{+0.09}_{-0.07} ^{+0.06}_{-0.05}$
$2.00 < p_T^2 < 2.50$	$1.66 \pm 0.05 ^{+0.07}_{-0.08}$	$1.88 \pm 0.06 ^{+0.04}_{-0.06}$	$1.78 ^{+0.06}_{-0.06} ^{+0.05}_{-0.01}$
$2.50 < p_T^2 < 3.00$	$1.11 \pm 0.04 ^{+0.08}_{-0.03}$	$1.28 \pm 0.05 ^{+0.03}_{-0.05}$	$1.20 ^{+0.05}_{-0.04} ^{+0.05}_{-0.01}$
$3.00 < p_T^2 < 4.00$	$.716 \pm .021 ^{+.042}_{-.019}$	$.739 \pm .026 ^{+.019}_{-.034}$	$.728 ^{+.028}_{-.026} ^{+.058}_{-.008}$
$4.00 < p_T^2 < 5.00$	$.350 \pm .015 ^{+.031}_{-.013}$	$.382 \pm .018 ^{+.022}_{-.012}$	$.367 ^{+.022}_{-.015} ^{+.040}_{-.007}$
$5.00 < p_T^2 < 6.00$	$.215 \pm .011 ^{+.014}_{-.008}$	$.217 \pm .013 ^{+.009}_{-.011}$	$.216 ^{+.012}_{-.011} ^{+.029}_{-.004}$
$6.00 < p_T^2 < 8.00$	$.0946 \pm .0050 ^{+.0066}_{-.0051}$	$.1034 \pm .0064 ^{+.0084}_{-.0042}$	$.0983 ^{+.0065}_{-.0052} ^{+.0099}_{-.0522}$
$8.00 < p_T^2 < 10.00$	$.0361 \pm .0051 ^{+.0066}_{-.0033}$	$.0354 \pm .0036 ^{+.0030}_{-.0035}$	$.0356 ^{+.0041}_{-.0040} ^{+.0034}_{-.0154}$
$10.00 < p_T^2 < 12.00$	$.0200 \pm .0023 ^{+.0067}_{-.0030}$	$.0157 \pm .0025 ^{+.0014}_{-.0017}$	$.0167 ^{+.0028}_{-.0025} ^{+.0030}_{-.0088}$
$12.00 < p_T^2 < 14.00$	$.0074 \pm .0013 ^{+.0031}_{-.0011}$	$.0119 \pm .0020 ^{+.0009}_{-.0015}$	$.0098 ^{+.0020}_{-.0016} ^{+.0035}_{-.0001}$
$14.00 < p_T^2 < 16.00$	$.0061 \pm .0012 ^{+.0010}_{-.0015}$	$.0049 \pm .0015 ^{+.0006}_{-.0005}$	$.0054 ^{+.0011}_{-.0012} ^{+.0006}_{-.0028}$
$16.00 < p_T^2 < 18.00$	$.0018 \pm .0005 ^{+.0012}_{-.0001}$	$.0029 \pm .0010 ^{+.0002}_{-.0008}$	$.0022 ^{+.0009}_{-.0006} ^{+.0016}_{-.0001}$

Table 6.4: p_T^2 differential cross section for D^0 mesons. The $K\pi$ and $K\pi\pi\pi$ errors are statistical plus uncorrelated systematic errors. The D^0 errors are combined $K\pi$ and $K\pi\pi\pi$ errors plus the remaining, correlated systematic errors. Normalization errors of $^{+10.5}_{-14.8}\%$ are *not* included.

can help us to determine the values of these parameters rather than to prove a theory to be right or wrong. To this end, we generate theoretical x_F and p_T^2 distributions for a variety of parameter sets. Most of the adjusted parameters involve the underlying c quark production. These are the parton distribution functions (PDF's) of the pion and nucleon, the intrinsic k_t of the partons, the mass of the charm quark, the factorization scale (μ_F), and the renormalization scale (μ_R).

As described in Section 1.2.1, the PDF's allow one to determine the type and momentum distribution of the constituents of the incoming hadrons (pions and nucleons in this case). Example PDF's are shown in Fig. 1.1. The PDF's are usually generated from global fits to various data including results from deep inelastic scattering (DIS) experiments and lepton and photon production experiments. As the amount of data increases, the fits become more constrained and thus become a better representation of the true distributions. Since the pion cannot be used as a target for DIS experiments, data is quite limited, especially for low x (x<0.2), where x is the fractional momentum carried by the parton. Because gluons do not interact with leptons, the gluon distribution functions are among the more poorly measured distribution functions; since most of the charm production in the E791 experiment involves gluons, this creates significant theoretical uncertainties. The uncertainties in the gluon distributions are evident in Fig. 6.9 which shows the gluon distributions for the proton and pion from various PDF's which are used in calculating the theoretical results. HMRSB [1] is a 1990 PDF set calculated in next-to-leading order and is the default proton PDF for the MNR NLO program. The SMRS2 [2] is also a PDF calculated in NLO by approximately the same group in 1992. This is the default pion PDF for the MNR NLO program. DO2 [35] and GRV [36] are leading order pion PDF's calculated in 1984 and 1992, respectively. DO2 is the default pion PDF for

PYTHIA/JETSET. The CTEQ collaboration PDF's used are the second (~1993) and fourth (1997) generation proton PDF's [37] which are calculated in both leading order (CTEQ2L - the default PYTHIA/JETSET proton PDF) and next-to-leading order (CTEQ2M and CTEQ4M) schemes. The order of calculation of the PDF must match the order of calculation of the charm quark production matrix elements. Therefore, only leading order calculations of PDF's can be used by PYTHIA/JETSET and only next-to-leading order calculations of PDF's can be used by MNR NLO.

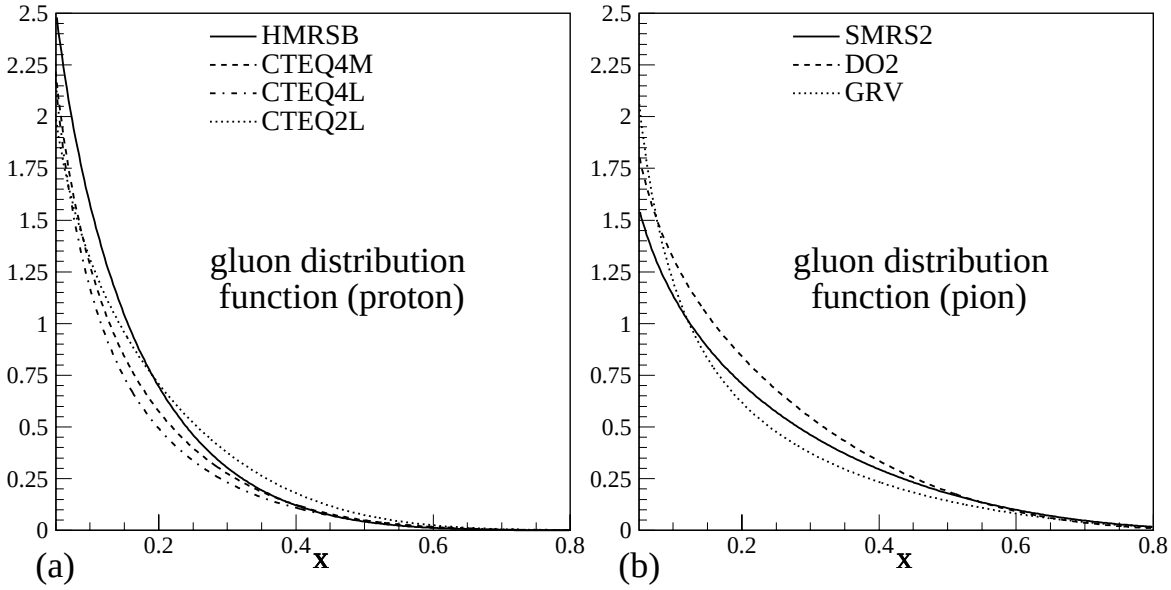

Fig. 6.9.— Plots of gluon distribution functions at Q^2=5 (GeV/c)^2 in the range $0.05<x<0.8$ for protons (a) and pions (b) from several PDF sets. The PDF data are obtained from the CERN program PDFLIB [3].

The PDF's are functions of the fractional momentum, x, and the scale of the interaction given by Q^2, the square of the momentum transfer. In charm production, however, Q^2 is not well-defined and therefore we adopt another parameter, the factorization scale μ_F. Another scale present in charm production theory is the renormalization scale μ_R which determines the scale at which α_s is evaluated. If one were able to calculate all contributions to the cross section, these terms would not enter

into the result. A finite order calculation introduces these unphysical quantities and varying these quantities within some reasonable range gives an indication of the significance of higher order terms. The most natural choice for the scale at which single inclusive charm production takes place is

$$\mu \equiv \sqrt{m_c^2 + p_T^2}. \tag{6.15}$$

Unfortunately, many PDF's are not accurate at a Q^2 less than $\sim$5 (GeV/c)^2 while for a charm quark mass of 1.5 GeV/c^2, the minimum value of μ^2 is 2.25 GeV^2. The MNR NLO solution is to set $\mu_F = 2\mu$ and $\mu_R = \mu$. In both programs, a call to a PDF at a scale less than the minimum defined scale (Q^2_{min}) is evaluated *at* Q^2_{min}.

In addition to energy scales and parton distribution functions, the mass of the charm quark and the intrinsic k_t of the incident partons can be varied within the framework of both theories. The default charm quark mass is 1.35 GeV/c^2 in PYTHIA/JETSET and 1.50 GeV/c^2 in MNR NLO. We generate theory distributions for charm quark masses of 1.35, 1.50 and 1.65 GeV/c^2. The default intrinsic $\sqrt{<k_t^2>}$ is 0.44 GeV/c in PYTHIA/JETSET and 0 in MNR NLO. For the PYTHIA/JETSET program we generate distributions with $\sqrt{<k_t^2>}$ of 0, 0.44 and 1 GeV/c while for the MNR NLO results we use $\sqrt{<k_t^2>}$ values of 0 and 1 GeV/c.

All of the parameters described above (PDF's, μ_F, μ_R, m_c, and $< k_t^2 >$) are significantly correlated. Increasing m_c or $< k_t^2 >$ increases the energy scale, μ, from which μ_F and μ_R are determined and which is therefore used in calculating the parton distributions. Obviously, this makes extracting exact values difficult and there are likely to be multiple solutions. To reduce the parameter space, we choose to fix the scale parameters μ_F and μ_R at their default values. By varying the rest of the parameters, we obtain many sets of theoretical predictions.

A direct comparison of the shapes of the data and the theoretical predictions can

be obtained by normalizing the theoretical predictions to the data. This is done by fitting the theoretical predictions to the data allowing only the normalization to float. The χ^2 minimization is performed using the CERN Library program, MINUIT[30]. The resulting χ^2/dof of the fit gives us information about how well the theoretical shape matches the shape found in the data. The χ^2/dof of each theoretical c-quark distribution fit to the x_F and p_T^2 data is shown in Tables 6.5 and 6.6 for the MNR NLO and PYTHIA/JETSET results, respectively. Both the MNR NLO and PYTHIA/JETSET results seem to favor higher masses and low intrinsic k_t. The default and best fit distributions from MNR NLO and PYTHIA/JETSET are shown with the x_F data in Fig. 6.10 and with the p_T^2 data in Fig 6.11.

PDF (π/N)	m_c (GeV/c^2)	$\sqrt{<k_t^2>}$ (GeV/c)	$(\chi^2/dof)_{x_F}$	$(\chi^2/dof)_{p_T^2}$	$<\chi^2/dof>$
SMRS2/HMRSB	1.35	0.00	3.7	4.9	4.3
SMRS2/HMRSB	1.35	1.00	1.3	19	10
SMRS2/HMRSB	**1.50**	**0.00**	1.6	1.1	1.4
SMRS2/HMRSB	1.50	1.00	0.7	31	16
SMRS2/HMRSB	1.65	0.00	0.8	5.4	3.1
SMRS2/HMRSB	1.65	1.00	0.8	43	22
SMRS2/CTEQ4M	1.35	0.00	1.8	6.4	4.1
SMRS2/CTEQ4M	1.35	1.00	0.9	18	9.3
SMRS2/CTEQ4M	*1.50*	*0.00*	1.0	1.4	1.2
SMRS2/CTEQ4M	1.50	1.00	0.9	29	15
SMRS2/CTEQ4M	1.65	0.00	0.9	5.6	3.2
SMRS2/CTEQ4M	1.65	1.00	1.4	44	23

Table 6.5: Results of fitting various MNR NLO c quark distributions to the data. The default (best fit) theory parameters are shown in bold (italics).

While it is interesting to compare the charm quark distributions to the data, we cannot know whether these comparisons make sense because of the hadronization process. If hadronization significantly affects the p_T^2 and/or x_F distributions then com-

PDF (π/N)	m_c (GeV/c^2)	$\sqrt{<k_t^2>}$ (GeV/c)	$(\chi^2/dof)_{x_F}$	$(\chi^2/dof)_{p_T^2}$	$<\chi^2/dof>$
DO2/CTEQ2L	1.35	0.00	2.2	5.7	4.0
DO2/CTEQ2L	**1.35**	**0.44**	1.9	8.4	5.1
DO2/CTEQ2L	1.35	1.00	1.3	34	18
DO2/CTEQ2L	1.50	0.00	0.8	17	8.7
DO2/CTEQ2L	1.50	0.44	0.8	19	9.9
DO2/CTEQ2L	1.50	1.00	0.6	50	26
DO2/CTEQ2L	1.65	0.00	0.6	27	14
DO2/CTEQ2L	1.65	0.44	0.6	32	16
DO2/CTEQ2L	1.65	1.00	0.8	68	34
GRV/CTEQ4L	1.35	0.00	4.4	2.8	3.6
GRV/CTEQ4L	*1.35*	*0.44*	3.9	1.4	2.7
GRV/CTEQ4L	1.35	1.00	2.4	16	9.1
GRV/CTEQ4L	1.50	0.00	1.7	4.4	3.1
GRV/CTEQ4L	1.50	0.44	1.5	6.6	4.0
GRV/CTEQ4L	1.50	1.00	0.9	30	15
GRV/CTEQ4L	1.65	0.00	0.6	13	7.0
GRV/CTEQ4L	1.65	0.44	0.6	17	9.0
GRV/CTEQ4L	1.65	1.00	0.5	47	24

Table 6.6: Results of fitting various PYTHIA/JETSET c quark distributions to the data. The default (best fit) theory parameters are shown in bold (italics).

paring c quark distributions with the data D meson distributions is of no use. In the MNR NLO program it is possible to simulate the hadronization with the Peterson fragmentation function which works well in e^+e^- annihilation experiments but is expected to fare poorly in hadroproduction experiments (cf Section 1.2.2). In PYTHIA/JETSET the Lund string model is used to perform the hadronization (cf Section 1.2.2). We show results for the default theory parameters for the hadronization and also for a hadronization where the average p_T imparted to quarks popped during the string fragmentation is increased from 0.36 GeV/c to 0.60 GeV/c. This is motivated by what was used in MC2 to harden the p_T^2 distribution (cf Section 6.2.3.1).

For each of the meson distributions we again perform a χ^2 minimization to obtain the normalization and χ^2/dof. The χ^2/dof of each theoretical D-meson distribution fit to the x_F and p_T^2 data is shown in Tables 6.7 and 6.8 for the MNR NLO and PYTHIA/JETSET results, respectively. As expected, the MNR NLO D meson predictions provide a poor match for the data unless a very high value for the intrinsic k_t is used. The PYTHIA/JETSET results seem to favor the more modern PDF's for the x_F distribution and the older PDF's for the p_T^2 distribution. However, with high values for $\sqrt{<k_t^2>}$ and fairly high masses, we get good agreement with the newer PDF's. The default and best fit distributions from MNR NLO and PYTHIA/JETSET are shown with the x_F data in Fig. 6.12 and with the p_T^2 data in Fig 6.13.

An alternative method of comparing data to theory and to other experiments is by fitting a function to the distribution and comparing parameters. This is most useful when the functions provide a good representation of the data and theory. If the function is not a particularly good fit, then differences in parameters might have little to do with the quantity one is trying to measure. In the past, x_F distributions have been fit with

$$\frac{d\sigma}{dx_F} = A(1-|x_F|)^n \tag{6.16}$$

This function was originally motivated by theoretical predictions for the high x_F region. This function does not provide a very good fit to the data. Although the χ^2/dof is small (0.3), the value of n is quite dependent on the range fitted and on the errors of the data points. Fitting the distribution of Fig. 6.7, which includes all of the non-normalization systematic errors, gives a values of $n = 4.61 \pm 0.19$ when fit in our standard range, $0.05 < x_F < 0.50$, as shown in Fig. 6.14. Increasing the lower bound to 0.075, 0.10, and 0.125 gives n values of 4.50±0.23, 4.39±0.27 and 4.34±0.32 while decreasing the upper bound to 0.40, 0.35, and 0.30 gives values of 4.63±0.19,

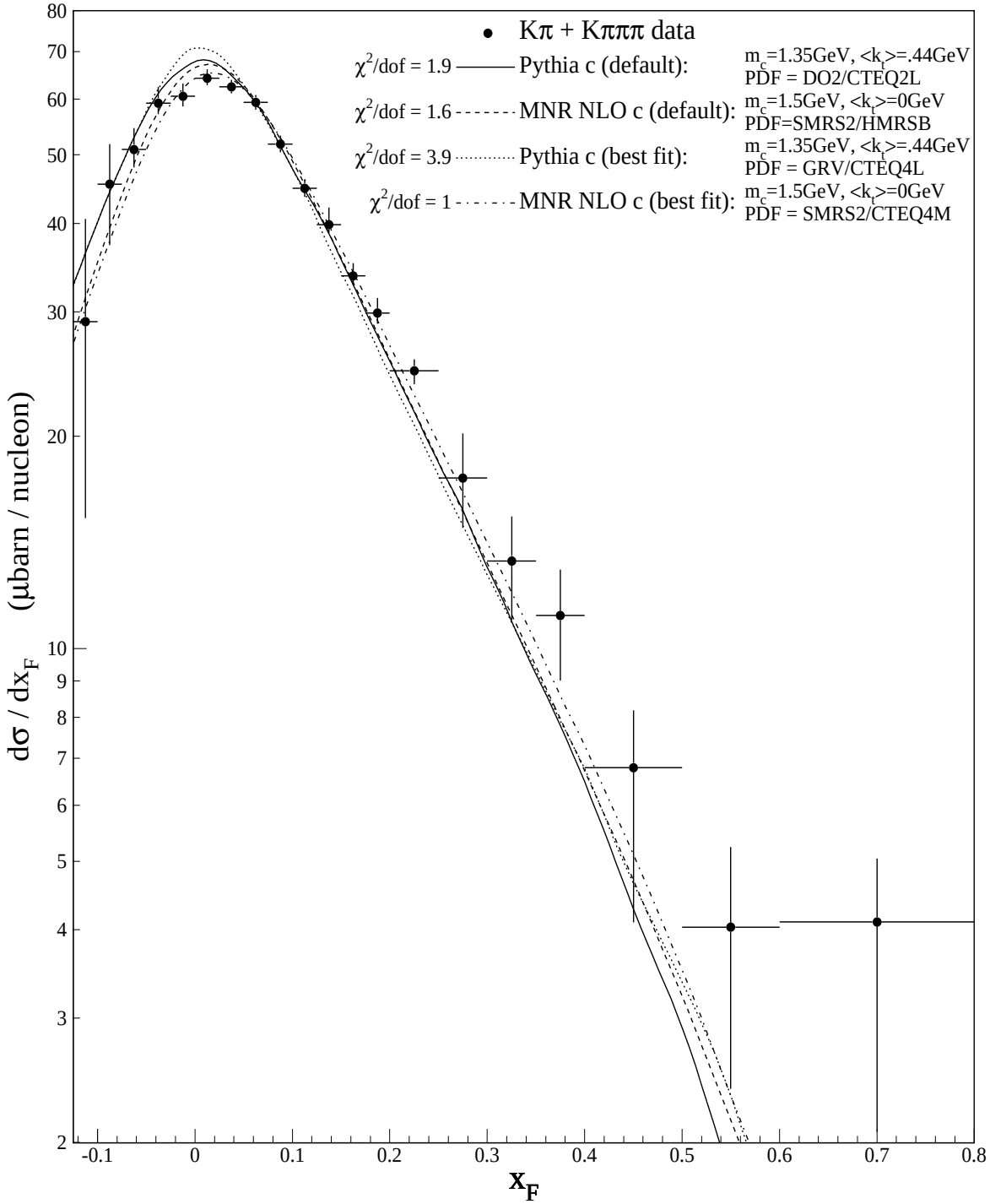

Fig. 6.10.— Comparison of the D^0 x_F distribution to theory predictions. The theory predictions are obtained for charm quarks using two different parameters, the default parameters and the set which best fits the x_F *and* p_T^2 data. The distributions are normalized to obtain the best fit to the data.

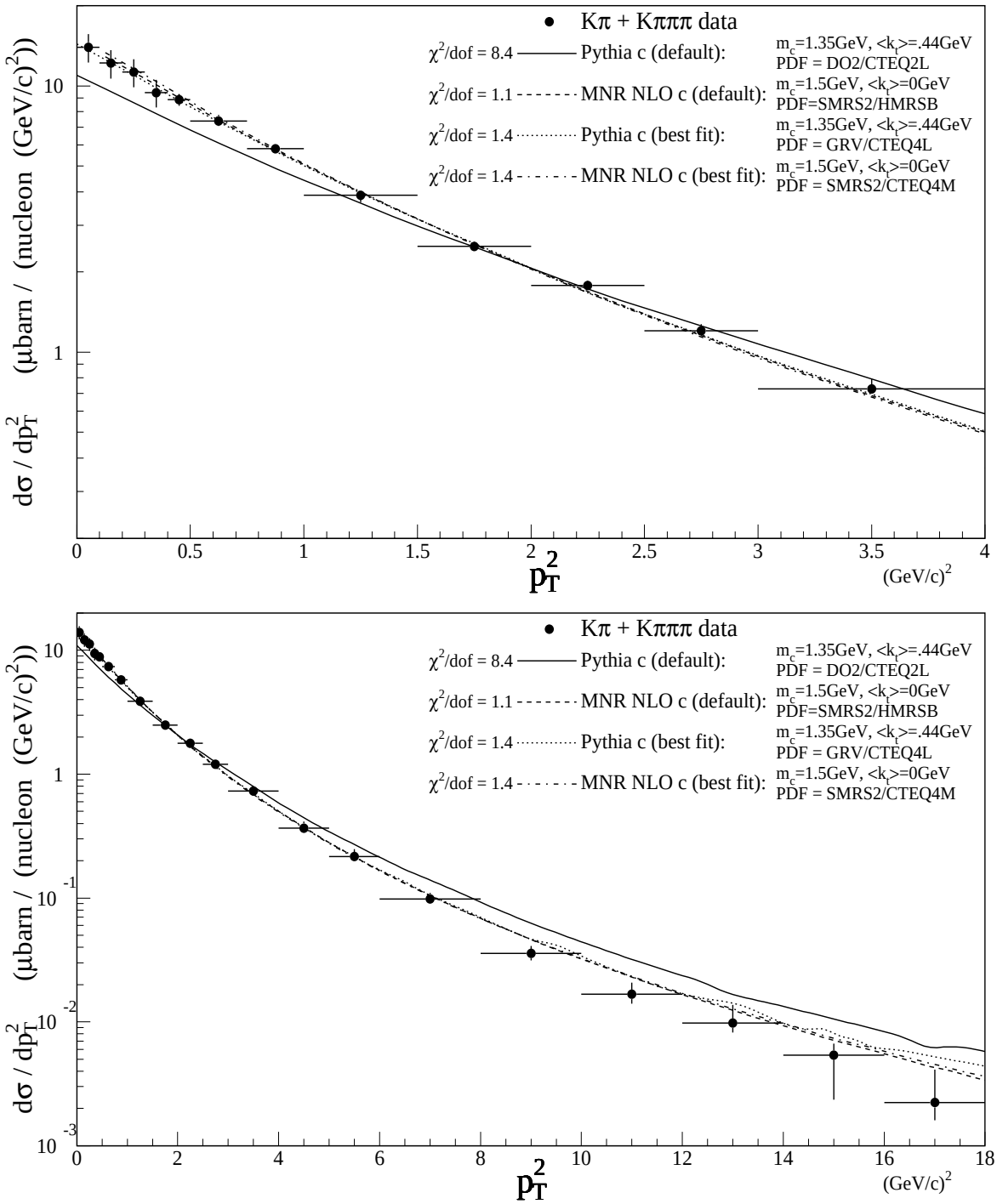

Fig. 6.11.— Comparison of the D^0 p_T^2 distribution to theory predictions. The theory predictions are obtained for charm quarks using two different parameters, the default parameters and the set which best fits the x_F *and* p_T^2 data. The distributions are normalized to obtain the best fit to the data.

PDF (π/N)	m_c (GeV/c^2)	$\sqrt{<k_t^2>}$ (GeV/c)	$(\chi^2/dof)_{x_F}$	$(\chi^2/dof)_{p_T^2}$	$<\chi^2/dof>$
SMRS2/HMRSB	1.35	0.00	14	130	73
SMRS2/HMRSB	1.35	1.00	10	28	19
SMRS2/HMRSB	1.35	2.00	7.6	0.8	4.2
SMRS2/HMRSB	**1.50**	**0.00**	8.7	84	46
SMRS2/HMRSB	1.50	1.00	6.3	11	8.9
SMRS2/HMRSB	1.50	2.00	4.6	1.5	3.1
SMRS2/HMRSB	1.65	0.00	5.2	47	26
SMRS2/HMRSB	1.65	1.00	3.7	2.5	3.1
SMRS2/HMRSB	1.65	2.00	2.8	5.2	4.0
SMRS2/CTEQ4M	1.35	0.00	8.3	140	73
SMRS2/CTEQ4M	1.35	1.00	5.5	31	18
SMRS2/CTEQ4M	1.35	2.00	3.9	1.0	2.4
SMRS2/CTEQ4M	1.50	0.00	5.2	86	46
SMRS2/CTEQ4M	1.50	1.00	3.7	13	8.1
SMRS2/CTEQ4M	*1.50*	*2.00*	2.7	1.3	2.0
SMRS2/CTEQ4M	1.65	0.00	3.4	48	25
SMRS2/CTEQ4M	1.65	1.00	2.6	2.7	2.6
SMRS2/CTEQ4M	1.65	2.00	2.1	4.5	3.3

Table 6.7: Results of fitting various MNR NLO D meson distributions to the data. The meson predictions are obtained using Peterson fragmentation. The default (best fit) theory parameters are shown in bold (italics).

PDF (π/N)	m_c (GeV/c^2)	$\sqrt{<k_t^2>}$ (GeV/c)	$(\chi^2/dof)_{x_F}$	$(\chi^2/dof)_{p_T^2}$	$<\chi^2/dof>$
DO2/CTEQ2L	1.35	0.00	3.7	8.7	6.2
DO2/CTEQ2L	**1.35**	**0.44**	3.5	6.7	5.1
DO2/CTEQ2L	1.35	1.00	2.2	0.4	1.3
DO2/CTEQ2L	1.50	0.00	3.6	2.4	3.0
DO2/CTEQ2L	1.50	0.44	3.3	1.9	2.6
DO2/CTEQ2L	1.50	1.00	2.2	0.9	1.5
DO2/CTEQ2L	1.65	0.00	3.4	0.7	2.1
DO2/CTEQ2L	1.50	0.44	2.7	0.5	1.6
DO2/CTEQ2L	1.65	1.00	1.8	2.7	2.3
GRV/CTEQ4L	1.35	0.00	1.5	31	16
GRV/CTEQ4L	1.35	0.44	1.6	26	14
GRV/CTEQ4L	1.35	1.00	1.1	5.5	3.3
GRV/CTEQ4L	1.50	0.00	1.6	15	8.2
GRV/CTEQ4L	1.50	0.44	1.4	11	6.4
GRV/CTEQ4L	1.50	1.00	1.0	1.2	1.1
GRV/CTEQ4L	1.65	0.00	1.5	5.7	3.6
GRV/CTEQ4L	1.65	0.44	1.3	4.0	2.7
GRV/CTEQ4L	*1.65*	*1.00*	1.0	0.5	0.7
GRV/CTEQ4L	1.35	0.00	1.7	11	6.2
GRV/CTEQ4L	1.35	0.44	1.7	7.3	4.5
GRV/CTEQ4L	1.35	1.00	1.3	0.6	1.0
GRV/CTEQ4L	1.50	0.00	1.6	3.1	2.3
GRV/CTEQ4L	1.50	0.44	1.8	1.8	1.8
GRV/CTEQ4L	1.50	1.00	1.0	1.2	1.1
GRV/CTEQ4L	1.65	0.00	1.4	0.6	1.0
GRV/CTEQ4L	1.65	0.44	1.4	0.5	0.9
GRV/CTEQ4L	1.65	1.00	0.9	3.8	2.4

Table 6.8: Results of fitting various PYTHIA/JETSET D^0 distributions to the data. Above the line are results obtained using the default fragmentation. The results below the line increase the average p_T of popped quarks from 0.36 to 0.60 GeV/c using PYTHIA parameter PARJ(21). The default (best fit) theory parameters are shown in bold (italics).

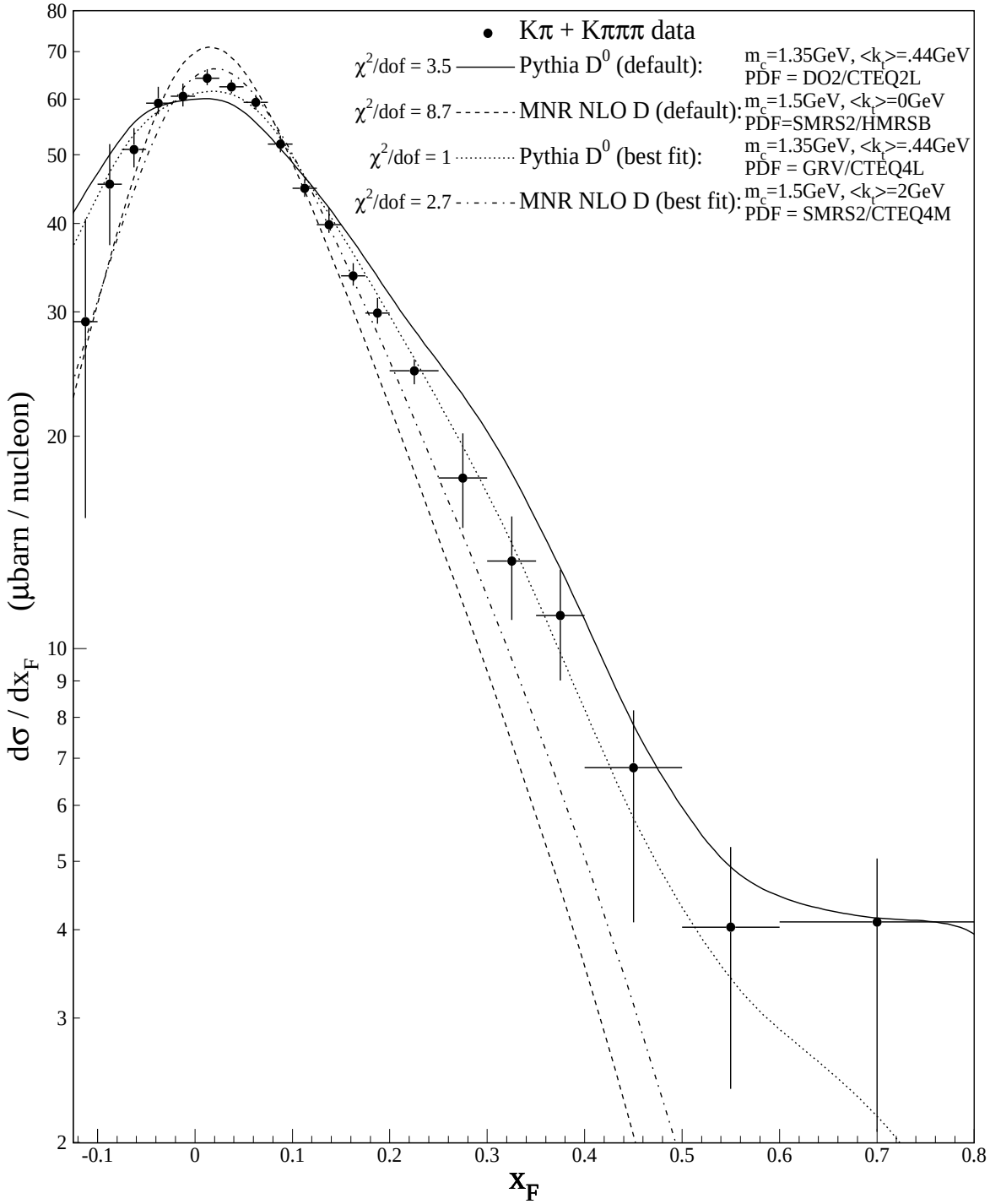

Fig. 6.12.— Comparison of the D^0 x_F distribution to theory predictions. The MNR NLO (PYTHIA/JETSET) predictions are obtained for D (D^0) mesons using two different parameters, the default parameters and the set which best fits the x_F *and* p_T^2 data. The distributions are normalized to obtain the best fit to the data.

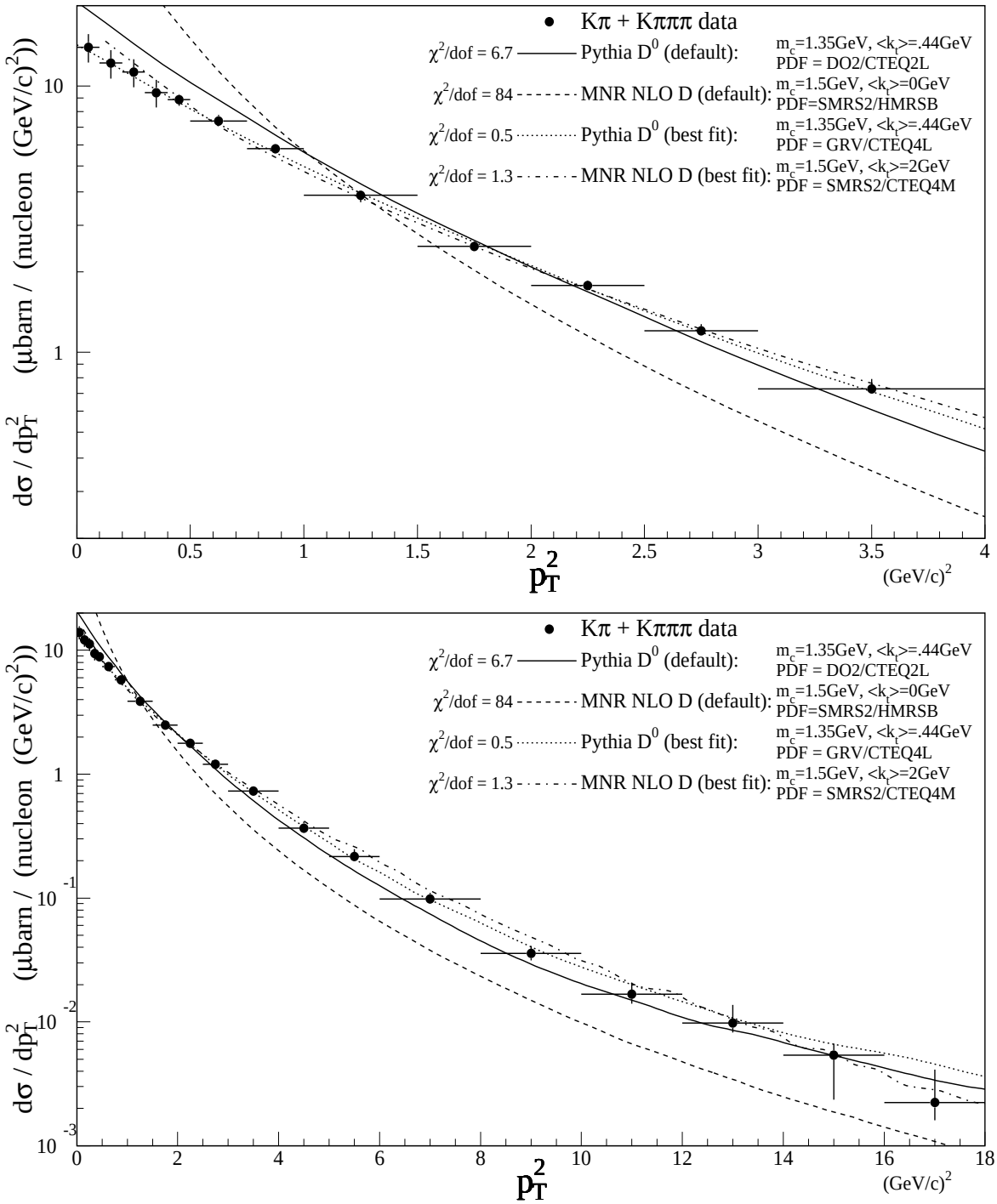

Fig. 6.13.— Comparison of the D^0 p_T^2 distribution to theory predictions. The MNR NLO (PYTHIA/JETSET) predictions are obtained for D (D^0) mesons using two different parameters, the default parameters and the set which best fits the x_F *and* p_T^2 data. The distributions are normalized to obtain the best fit to the data.

4.69±0.20, and 4.71±0.21. A fit performed over the standard range to the same distribution with only statistical errors, returns $n = 4.48 \pm 0.07$ with a χ^2/dof of 3.0. Another function which can be extended into the negative x_F region is an extension of Eq. 6.16 which uses the $(1-|x_F|)^n$ function in the tail region and a Gaussian in the central region, that is,

$$\frac{d\sigma}{dx_F} = \begin{cases} A(1-|x_F-x_c|)^{n'}, & |x_F-x_c| > x_b \\ A' \exp\left[-\frac{1}{2}(\frac{x_F-x_c}{\sigma})^2\right], & |x_F-x_c| < x_b \end{cases} \tag{6.17}$$

Continuous functions and derivatives are maintained at $|x_F - x_c| = x_b$ by requiring

$$\sigma = \sqrt{\frac{x_b(1-x_b)}{n'}} \tag{6.18}$$

$$\frac{A'}{A} = (1-x_b)^{n'} \exp\left[\frac{n'\,x_b}{2(1-x_b)}\right] \tag{6.19}$$

Therefore Eq. 6.17 can be written with one normalization parameter and three other parameters which determine the shape: n' gives the shape in the tail region, x_c is the turnover point, and x_b is the boundary between the Gaussian and power-law function. Fitting this function to our data in the range -0.125<x_F<0.50 gives $n' = 4.68 \pm 0.21$, $x_c = 0.0131 \pm 0.0038$, and $x_b = 0.062 \pm 0.013$ with a χ^2/dof=0.4 as shown in Fig. 6.14. First, we notice that the start of the tail region, 0.062, is quite close to the start of our standard range for Eq. 6.16 or 0.05. We also see that x_c is significantly greater than zero. This is consistent with the parton distribution functions shown in Figures 1.1 and 6.9 which show significantly harder parton distributions for the pion than for the proton. Therefore, the parton center of mass will generally be moving in the direction of the pion (positive x_F) in the hadron center of mass frame (in which x_F is calculated). To test the stability of the values returned by a fit to this function we make the same checks as were made for fitting Eq. 6.16. Fitting the same distribution with only

statistical errors returns $n' = 4.54 \pm 0.08$, $x_c = 0.0137 \pm 0.0025$, and $x_b = 0.055 \pm 0.008$ with χ^2/dof=2.3. The n' value again shows a large (2/3 σ) change, the same as in the fit to Eq. 6.16. The other parameters are more stable. Since the cross-over point from Gaussian to power-law is a parameter of the fit, the variations due to fitting different ranges are much smaller. This is seen in the results from changing the upper and lower limits, shown in Table 6.9.

x_F Range of fit	n'	x_c	x_b
-0.125 $< x_F <$ 0.500	4.68 ± 0.21	0.0131 ± 0.0038	0.062 ± 0.013
-0.100 $< x_F <$ 0.500	4.67 ± 0.21	0.0126 ± 0.0039	0.062 ± 0.013
-0.075 $< x_F <$ 0.500	4.67 ± 0.21	0.0126 ± 0.0040	0.062 ± 0.013
-0.050 $< x_F <$ 0.500	4.67 ± 0.21	0.0120 ± 0.0052	0.064 ± 0.015
-0.125 $< x_F <$ 0.400	4.71 ± 0.22	0.0131 ± 0.0038	0.062 ± 0.013
-0.125 $< x_F <$ 0.350	4.78 ± 0.23	0.0134 ± 0.0038	0.064 ± 0.013
-0.125 $< x_F <$ 0.300	4.80 ± 0.24	0.0134 ± 0.0038	0.065 ± 0.013

Table 6.9: Effect of changing x_F lower and upper limits on the parameters n', x_c, and x_b of Eq. 6.17.

Although the usefulness of these fits is quite limited, we nevertheless fit the same theoretical predictions as were used in checking the distributions directly. The results of the fits to the c quark distributions, along with the χ^2/dof of each fit, are shown in Tables 6.10 and 6.11 for the MNR NLO results and the PYTHIA/JETSET results, respectively. The results for the D meson distributions are shown in Tables 6.10 and 6.11 for MNR NLO and PYTHIA/JETSET, respectively. The large χ^2/dof is partly due to the very small errors associated with the theoretical distributions. From these results we see that the MNR NLO tend to peak at higher x_F with x_c around 0.025 compared to the data value of 0.013 while the PYTHIA/JETSET seems to be closer with x_c between 0.010 and 0.015 for the quarks and reduced by about 0.005 for the D^0 mesons. The n and n' values vary quite a bit for the different input parameters.

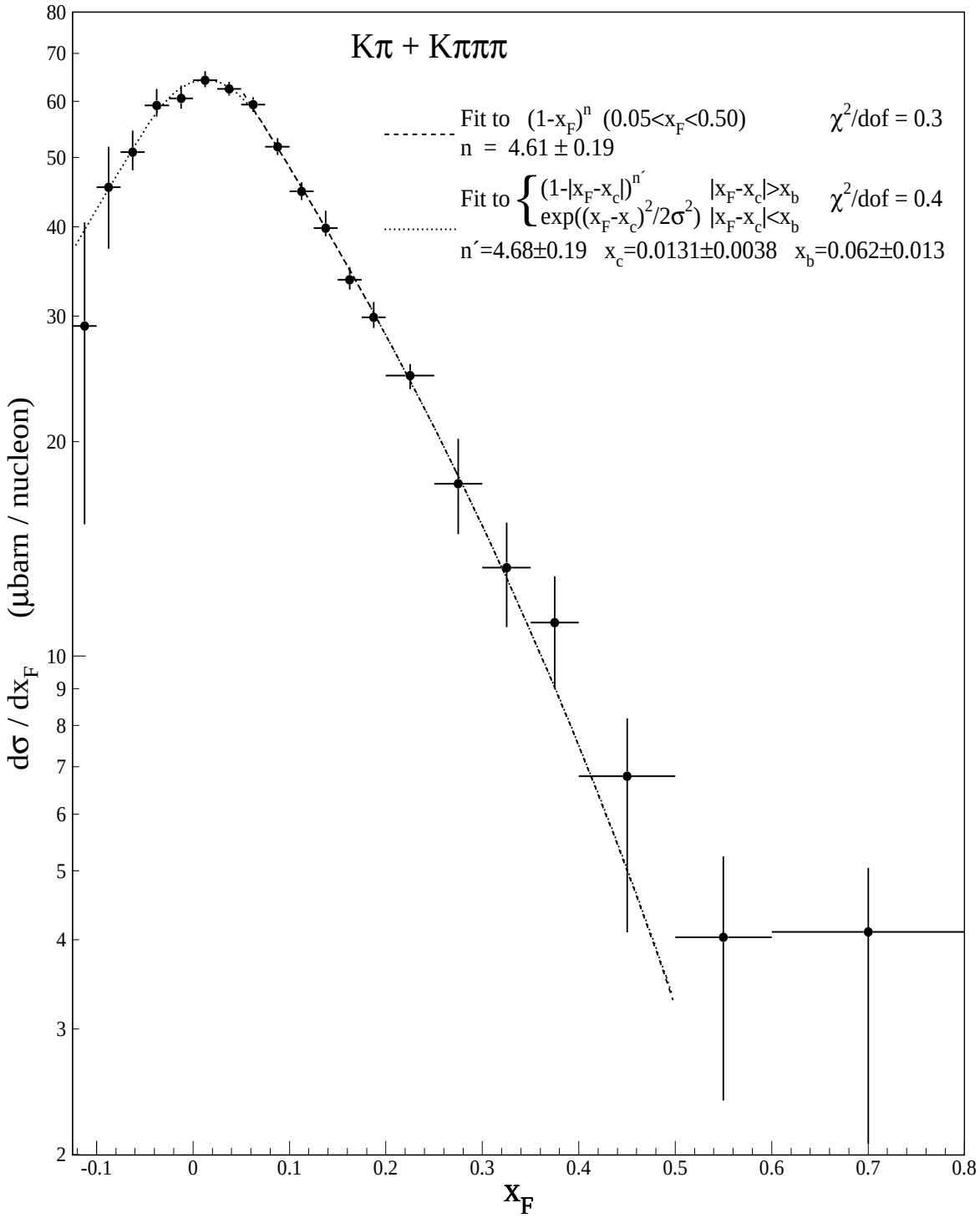

Fig. 6.14.— Fits to the D^0 fully corrected x_F differential cross section with the functions given in Eqs. 6.16 (dashed) and 6.17 (dotted). The error bars include all errors except a $^{+10.2}_{-10.9}\%$ normalization error.

PDF (π/N)	m_c (GeV/c^2)	$\sqrt{<k_t^2>}$ (GeV/c)	n	χ^2/dof	n'	x_c	x_b	χ^2/dof
SMRS2/HMRSB	1.35	0.00	5.22	1000	5.54	0.0192	0.031	2700
SMRS2/HMRSB	1.35	1.00	4.84	96	5.25	0.0214	0.039	430
SMRS2/HMRSB	**1.50**	**0.00**	5.01	620	5.28	0.0211	0.039	1800
SMRS2/HMRSB	1.50	1.00	4.67	72	5.03	0.0229	0.046	370
SMRS2/HMRSB	1.65	0.00	4.81	370	5.07	0.0232	0.048	1300
SMRS2/HMRSB	1.65	1.00	4.51	40	4.82	0.0242	0.054	270
SMRS2/CTEQ4M	1.35	0.00	4.94	740	5.32	0.0258	0.032	2900
SMRS2/CTEQ4M	1.35	1.00	4.54	62	4.97	0.0270	0.041	430
SMRS2/CTEQ4M	1.50	0.00	4.78	450	5.10	0.0261	0.041	1900
SMRS2/CTEQ4M	1.50	1.00	4.45	56	4.85	0.0287	0.045	360
SMRS2/CTEQ4M	1.65	0.00	4.63	290	4.91	0.0269	0.050	1200
SMRS2/CTEQ4M	1.65	1.00	4.36	250	4.70	0.0297	0.053	250

Table 6.10: Shape parameter results from fits to various MNR NLO c quark x_F distributions. Parameter(s) n (n', x_c, and x_b) come from fitting the x_F distribution with Eq. 6.16 (6.17) in the range $0.05<x_F<0.50$ ($-0.125<x_F<0.50$). The default theory parameters are shown in bold.

Both the MNR NLO and PYTHIA/JETSET charm quark models predict n values of 4.5-5.0, in good agreement with the data, 4.6. The hadronization for both theories provides worse agreement which gets better only when large charm quark masses are used and large amounts of intrinsic k_t are added. Although the solution is the same for both theories, the problems are clearly different because the effect of increasing the charm quark mass and adding intrinsic k_t is opposite in the two models. In the MNR NLO model, the addition of k_t and the increase in the quark mass results in the charm quark having more energy. Therefore, after it has lost energy due to the Peterson fragmentation, it is approximately back to the original level. In the PYTHIA/JETSET model, the addition of mass or intrinsic k_t reduces the amount of coalescence taking place. Recall that coalescence occurs when the invariant mass of a string is too small to pop $q\overline{q}$ pairs and collapses to a single meson. If one end of this string is tied to

PDF (π/N)	m_c (GeV/c^2)	$\sqrt{<k_t^2>}$ (GeV/c)	n	χ^2/dof	n'	x_c	x_b	χ^2/dof
DO2/CTEQ2L	1.35	0.00	5.02	15	5.12	0.0105	0.041	23
DO2/CTEQ2L	**1.35**	**0.44**	5.01	17	5.12	0.0115	0.045	27
DO2/CTEQ2L	1.35	1.00	4.88	15	4.99	0.0115	0.047	21
DO2/CTEQ2L	1.50	0.00	4.85	5.9	4.97	0.0141	0.053	14
DO2/CTEQ2L	1.50	0.44	4.84	8.2	4.96	0.0146	0.055	14
DO2/CTEQ2L	1.50	1.00	4.74	6.6	4.86	0.0154	0.056	11
DO2/CTEQ2L	1.65	0.00	4.71	5.9	4.86	0.0160	0.066	7.6
DO2/CTEQ2L	1.65	0.44	4.69	6.5	4.83	0.0165	0.065	9.9
DO2/CTEQ2L	1.65	1.00	4.60	7.0	4.76	0.0175	0.070	7.6
GRV/CTEQ4L	1.35	0.00	4.99	73	5.14	0.0089	0.025	80
GRV/CTEQ4L	1.35	0.44	4.95	65	5.09	0.0092	0.024	68
GRV/CTEQ4L	1.35	1.00	4.76	57	4.89	0.0092	0.030	63
GRV/CTEQ4L	1.50	0.00	4.82	42	4.95	0.0119	0.038	48
GRV/CTEQ4L	1.50	0.44	4.78	36	4.89	0.0114	0.037	44
GRV/CTEQ4L	1.50	1.00	4.63	41	4.74	0.0123	0.040	41
GRV/CTEQ4L	1.65	0.00	4.67	26	4.79	0.0143	0.048	32
GRV/CTEQ4L	1.65	0.44	4.61	20	4.73	0.0145	0.050	26
GRV/CTEQ4L	1.65	1.00	4.50	22	4.62	0.0155	0.051	30

Table 6.11: Shape parameter results from fits to various PYTHIA/JETSET c quark x_F distributions. Parameter(s) n (n', x_c, and x_b) come from fitting the x_F distribution with Eq. 6.16 (6.17) in the range $0.05<x_F<0.50$ ($-0.125<x_F<0.50$). The default theory parameters are shown in bold.

PDF (π/N)	m_c (GeV/c^2)	$\sqrt{<k_t^2>}$ (GeV/c)	n	χ^2/dof	n'	x_c	x_b	χ^2/dof
SMRS2/HMRSB	1.35	0.00	6.81	200	7.35	0.0221	0.042	3300
SMRS2/HMRSB	1.35	1.00	6.42	45	7.12	0.0230	0.048	1100
SMRS2/HMRSB	1.35	2.00	6.14	30	6.82	0.0236	0.044	580
SMRS2/HMRSB	**1.50**	**0.00**	6.49	130	6.97	0.0241	0.050	2300
SMRS2/HMRSB	1.50	1.00	6.18	42	6.79	0.0250	0.053	940
SMRS2/HMRSB	1.50	2.00	5.92	24	6.50	0.0253	0.055	490
SMRS2/HMRSB	1.65	0.00	6.19	200	6.66	0.0263	0.058	1700
SMRS2/HMRSB	1.65	1.00	5.93	75	6.45	0.0272	0.060	720
SMRS2/HMRSB	1.65	2.00	5.72	50	6.25	0.0271	0.061	420
SMRS2/CTEQ4M	1.35	0.00	6.39	90	6.97	0.0281	0.045	3100
SMRS2/CTEQ4M	1.35	1.00	6.03	28	6.75	0.0286	0.051	1000
SMRS2/CTEQ4M	1.35	2.00	5.73	14	6.34	0.0279	0.051	430
SMRS2/CTEQ4M	1.50	0.00	6.15	150	6.65	0.0288	0.053	2100
SMRS2/CTEQ4M	1.50	1.00	5.84	57	6.48	0.0294	0.056	820
SMRS2/CTEQ4M	1.50	2.00	5.60	32	6.30	0.0305	0.059	500
SMRS2/CTEQ4M	1.65	0.00	5.92	340	6.39	0.0294	0.062	1400
SMRS2/CTEQ4M	1.65	1.00	5.64	130	6.16	0.0313	0.065	450
SMRS2/CTEQ4M	1.65	2.00	5.42	79	5.98	0.0308	0.064	360

Table 6.12: Shape parameter results from fits to various MNR NLO D meson x_F distributions. Parameter(s) n (n', x_c, and x_b) come from fitting the x_F distribution with Eq. 6.16 (6.17) in the range $0.05<x_F<0.50$ ($-0.125<x_F<0.50$). The default theory parameters are shown in bold.

PDF (π/N)	m_c (GeV/c^2)	$\sqrt{<k_t^2>}$ (GeV/c)	n	χ^2/dof	n'	x_c	x_b	χ^2/dof
DO2/CTEQ2L	1.35	0.00	3.52	7.5	3.54	0.0025	0.071	6.5
DO2/CTEQ2L	**1.35**	**0.44**	3.62	4.7	3.66	0.0041	0.088	4.4
DO2/CTEQ2L	1.35	1.00	3.88	2.5	3.95	0.0074	0.088	2.6
DO2/CTEQ2L	1.50	0.00	3.69	8.5	3.75	0.0059	0.092	6.3
DO2/CTEQ2L	1.50	0.44	3.81	5.3	3.89	0.0072	0.100	3.7
DO2/CTEQ2L	1.50	1.00	4.08	5.9	4.19	0.0106	0.097	3.9
DO2/CTEQ2L	1.65	0.00	3.91	16	4.04	0.0085	0.111	8.8
DO2/CTEQ2L	1.65	0.44	4.06	9.8	4.19	0.0104	0.108	6.1
DO2/CTEQ2L	1.65	1.00	4.33	11	4.50	0.0128	0.105	5.3
GRV/CTEQ4L	1.35	0.00	3.65	5.0	3.68	0.0024	0.047	5.5
GRV/CTEQ4L	1.35	0.44	3.76	4.9	3.79	0.0042	0.068	5.0
GRV/CTEQ4L	1.35	1.00	3.91	7.2	3.96	0.0061	0.072	7.3
GRV/CTEQ4L	1.50	0.00	3.86	3.5	3.91	0.0069	0.074	3.9
GRV/CTEQ4L	1.50	0.44	3.95	3.1	4.01	0.0074	0.081	4.6
GRV/CTEQ4L	1.50	1.00	4.12	4.3	4.20	0.0096	0.079	5.1
GRV/CTEQ4L	1.65	0.00	4.08	2.6	4.17	0.0101	0.086	3.5
GRV/CTEQ4L	1.65	0.44	4.15	2.7	4.25	0.0110	0.089	3.9
GRV/CTEQ4L	1.65	1.00	4.35	3.5	4.46	0.0127	0.086	3.4
GRV/CTEQ4L	1.35	0.00	3.61	8.7	3.64	0.0029	0.056	8.3
GRV/CTEQ4L	1.35	0.44	3.68	12	3.71	0.0040	0.069	12
GRV/CTEQ4L	1.35	1.00	3.83	14	3.87	0.0061	0.070	13
GRV/CTEQ4L	1.50	0.00	3.81	7.8	3.86	0.0065	0.074	8.0
GRV/CTEQ4L	1.50	0.44	3.87	7.5	3.93	0.0079	0.0080	9.2
GRV/CTEQ4L	1.50	1.00	4.00	9.5	4.07	0.0094	0.073	9.2
GRV/CTEQ4L	1.65	0.00	4.02	4.4	4.10	0.0103	0.082	5.8
GRV/CTEQ4L	1.65	0.44	4.07	3.9	4.16	0.0107	0.083	5.4
GRV/CTEQ4L	1.65	1.00	4.22	5.3	4.32	0.0125	0.078	5.5

Table 6.13: Shape parameters from fits to various PYTHIA/JETSET D^0 x_F distributions. Above the line are results obtained using the default fragmentation. The results below the line increase the average p_T of popped quarks from 0.36 to 0.60 GeV/c using PYTHIA parameter PARJ(21). Parameter(s) n (n', x_c, and x_b) come from fitting the x_F distributions with Eq. 6.16 (6.17) in the range $0.05<x_F<0.50$ ($-0.125<x_F<0.50$). The default theory parameters are shown in bold.

a remnant quark from the pion, the meson will be boosted forward. Increasing k_t or the charm quark mass increases the invariant mass of the strings, reducing this effect, and again bringing the meson predictions closer to the quark predictions.

The functions which have been used in the past to fit the p_T^2 distribution are:

$$\frac{d\sigma}{dp_T^2} = Ae^{-bp_T^2} \tag{6.20}$$

at low p_T^2 ($p_T^2 < 4.0$ (GeV/c)^2 for this analysis),

$$\frac{d\sigma}{dp_T^2} = Ae^{-b'p_T} \tag{6.21}$$

at high p_T^2 ($p_T^2 > 1.0$ (GeV/c)^2 for this analysis), and

$$\frac{d\sigma}{dp_T^2} = \left[\frac{A}{\alpha\, m_c^2 + p_T^2}\right]^{\beta} \tag{6.22}$$

over all p_T^2 with m_c set to 1.5 GeV/c^2. The results of fitting these equations to the data are shown in Fig. 6.15. For the ranges given above, the results are:

- $b = 0.83 \pm 0.02$ with χ^2/dof =2.8
- $b' = 2.41 \pm 0.03$ with χ^2/dof =1.7
- $\alpha = 2.92 \pm 0.55$ (GeV/c^2)$^{-2}$ and $\beta = 6.68 \pm 0.77$ with $\chi^2/dof = 1.3$

Equation 6.20 does not provide a good fit even over the very limited range for which it is applied. While the χ^2/dof of the fit to Eq. 6.21 is not good (1.7), it appears to be a reasonable fit to the data. Equations 6.22 provides a very good fit to the data over the entire range of p_T^2. Unfortunately, there are some problems with this function as well. Using two free parameters (in addition to the normalization) makes it more difficult to compare with other experiments or theory since it is not clear what the variables are measuring. Also, the variables in this fit are highly correlated and compensating. This is reflected in the large (12-19%) errors compared to the error on b' (1%).

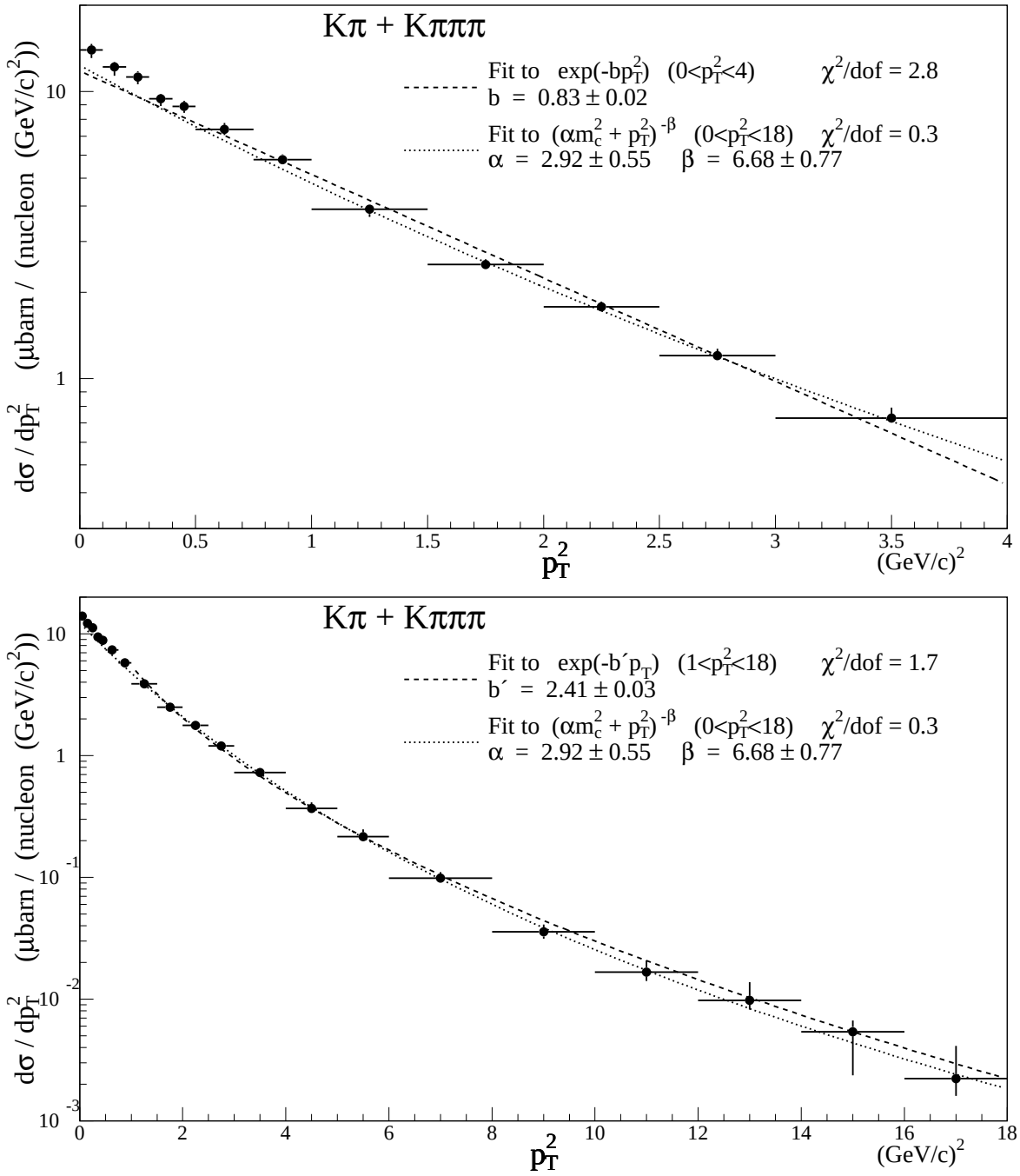

Fig. 6.15.— Fits to the D^0 fully corrected p_T^2 differential cross section with the functions given in Eqs. 6.20 (dashed, top), 6.21 (dashed, bottom), and 6.22 (dotted, top and bottom). The top plot shows the range $0<p_T^2<4$ (GeV/c)^2 while the bottom plot shows the full range, $0<p_T^2<18$ (GeV/c)^2. The error bars include all errors except a $^{+10.5}_{-14.8}\%$ normalization error.

The results of fitting these functions to the c quark theoretical distributions are shown in Tables 6.14 and 6.15 for the MNR NLO and PYTHIA/JETSET results, respectively. The same results for D quark distributions are shown in Tables 6.16 and 6.17. Since Eq. 6.20 is such a poor fit to the data and theory alike, we ignore these

PDF (π/N)	m_c (GeV/c^2)	$\sqrt{<k_t^2>}$ (GeV/c)	b	χ^2/dof	b'	χ^2/dof	α	β	χ^2/dof
SMRS2/HMRSB	1.35	0.00	1.05	∞	2.51	410	1.47	4.80	2.9
SMRS2/HMRSB	1.35	1.00	0.61	18	2.04	95	6.19	9.27	2.1
SMRS2/HMRSB	**1.50**	**0.00**	0.92	∞	2.33	400	1.78	4.92	2.0
SMRS2/HMRSB	1.50	1.00	0.56	38	1.88	150	6.19	8.67	1.7
SMRS2/HMRSB	1.65	0.00	0.81	7500	2.18	630	2.14	5.05	3.5
SMRS2/HMRSB	1.65	1.00	0.53	36	1.75	190	6.49	8.41	1.2
SMRS2/CTEQ4M	1.35	0.00	1.08	∞	2.52	540	1.35	4.62	3.4
SMRS2/CTEQ4M	1.35	1.00	0.62	48	2.00	140	5.53	8.61	2.2
SMRS2/CTEQ4M	1.50	0.00	0.94	∞	2.34	410	1.65	4.73	2.0
SMRS2/CTEQ4M	1.50	1.00	0.57	41	1.88	140	5.74	8.26	1.4
SMRS2/CTEQ4M	1.65	0.00	0.82	9000	2.17	530	1.99	4.85	3.6
SMRS2/CTEQ4M	1.65	1.00	0.54	35	1.77	150	6.00	7.96	1.1

Table 6.14: Shape parameter results from fits to various MNR NLO c quark p_T^2 distributions. The parameters b, b', and α & β come from fitting the p_T^2 distribution with Eqs. 6.20, 6.21, and 6.22, in the ranges 0 (GeV/c)^2<p_T^2<4 (GeV/c)^2, 1 (GeV/c)^2<p_T^2<18 (GeV/c)^2, and 0 (GeV/c)^2<p_T^2<18 (GeV/c)^2, respectively. The default theory parameters are shown in bold.

results. The results of the MNR NLO c quark distributions show fair agreement with the data and seem to favor a charm quark mass of 1.5 GeV/c^2 with no intrinsic k_t. Increasing k_t or the charm quark mass clearly hardens the p_T^2 spectrum (b' decreases). The PYTHIA/JETSET c quark results show a similar trend but seem to prefer lower values of the charm quark mass. None of the c quark results comes close to matching the α and β parameters of Eq. 6.22, even with the large errors on the data. The MNR NLO D meson predictions, just as in the x_F case, requires a large intrinsic k_t

PDF (π/N)	m_c (GeV/c^2)	$\sqrt{<k_t^2>}$ (GeV/c)	b	χ^2/dof	b'	χ^2/dof	α	β	χ^2/dof
DO2/CTEQ2L	1.35	0.00	0.84	480	2.14	15	1.76	4.51	4.5
DO2/CTEQ2L	**1.35**	**0.44**	0.77	240	2.09	33	2.32	5.14	2.0
DO2/CTEQ2L	1.35	1.00	0.58	63	1.84	140	4.56	6.87	3.3
DO2/CTEQ2L	1.50	0.00	0.73	250	1.99	26	2.18	4.69	2.3
DO2/CTEQ2L	1.50	0.44	0.69	140	1.96	47	2.76	5.32	2.1
DO2/CTEQ2L	1.50	1.00	0.52	40	1.74	170	5.52	7.39	2.5
DO2/CTEQ2L	1.65	0.00	0.67	150	1.89	40	2.66	5.01	1.6
DO2/CTEQ2L	1.65	0.44	0.62	77	1.85	69	3.35	5.64	2.2
DO2/CTEQ2L	1.65	1.00	0.48	27	1.65	180	6.18	7.55	2.4
GRV/CTEQ4L	1.35	0.00	1.00	670	2.37	11	1.33	4.29	1.9
GRV/CTEQ4L	1.35	0.44	0.90	340	2.31	16	1.82	4.94	2.6
GRV/CTEQ4L	1.35	1.00	0.65	78	2.00	110	3.87	6.74	2.5
GRV/CTEQ4L	1.50	0.00	0.87	420	2.19	12	1.67	4.47	1.7
GRV/CTEQ4L	1.50	0.44	0.80	220	2.14	22	2.14	4.98	1.8
GRV/CTEQ4L	1.50	1.00	0.59	57	1.87	120	4.38	6.82	1.9
GRV/CTEQ4L	1.65	0.00	0.77	270	2.04	18	2.00	4.57	1.5
GRV/CTEQ4L	1.65	0.44	0.71	130	1.98	35	2.53	5.09	2.5
GRV/CTEQ4L	1.65	1.00	0.54	45	1.76	140	4.88	6.84	2.2

Table 6.15: Shape parameter results from fits to various PYTHIA/JETSET c quark p_T^2 distributions. The parameters b, b', and α & β come from fitting the p_T^2 distribution with Eqs. 6.20, 6.21, and 6.22, in the ranges 0 (GeV/c)^2<p_T^2<4 (GeV/c)^2, 1 (GeV/c)^2<p_T^2<18 (GeV/c)^2, and 0 (GeV/c)^2<p_T^2<18 (GeV/c)^2, respectively. The default theory parameters are shown in bold.

PDF (π/N)	m_c (GeV/c^2)	$\sqrt{<k_t^2>}$ (GeV/c)	b	χ^2/dof	b'	χ^2/dof	α	β	χ^2/dof
SMRS2/HMRSB	1.35	0.00	2.36	∞	3.28	1100	0.42	3.79	2300
SMRS2/HMRSB	1.35	1.00	1.57	3700	2.87	6.6	0.86	4.34	190
SMRS2/HMRSB	1.35	2.00	1.15	1500	2.36	19	1.09	4.01	93
SMRS2/HMRSB	**1.50**	**0.00**	1.94	∞	3.05	840	0.52	3.79	2400
SMRS2/HMRSB	1.50	1.00	1.38	3200	2.65	16	1.02	4.38	130
SMRS2/HMRSB	1.50	2.00	1.05	2100	2.23	25	1.16	3.90	120
SMRS2/HMRSB	1.65	0.00	1.63	∞	2.85	590	0.63	3.82	2400
SMRS2/HMRSB	1.65	1.00	1.38	4000	2.47	20	0.95	3.93	200
SMRS2/HMRSB	1.65	2.00	0.99	1900	2.12	25	1.20	3.74	130
SMRS2/CTEQ4M	1.35	0.00	2.44	∞	3.28	1300	0.39	3.70	2400
SMRS2/CTEQ4M	1.35	1.00	1.76	4700	2.85	10	0.77	4.11	210
SMRS2/CTEQ4M	1.35	2.00	1.30	2800	2.37	19	0.93	3.77	170
SMRS2/CTEQ4M	1.50	0.00	1.98	∞	3.05	1000	0.49	3.70	2400
SMRS2/CTEQ4M	1.50	1.00	1.46	5400	2.65	15	0.88	4.06	250
SMRS2/CTEQ4M	1.50	2.00	1.22	3000	2.24	24	0.96	3.60	180
SMRS2/CTEQ4M	1.65	0.00	1.65	∞	2.84	740	0.59	3.71	2400
SMRS2/CTEQ4M	1.65	1.00	1.35	4500	2.48	16	0.94	3.92	230
SMRS2/CTEQ4M	1.65	2.00	1.10	2500	2.12	28	1.07	3.59	170

Table 6.16: Shape parameters from fits to various MNR NLO D meson p_T^2 distributions. The results are obtained using Peterson fragmentation. The parameters b, b', and α & β come from fitting the p_T^2 distribution with Eqs. 6.20, 6.21, and 6.22, in the ranges 0 (GeV/c)^2<p_T^2<4 (GeV/c)^2, 1 (GeV/c)^2<p_T^2<18 (GeV/c)^2, and 0 (GeV/c)^2<p_T^2<18 (GeV/c)^2, respectively. The default theory parameters are shown in bold.

PDF (π/N)	m_c (GeV/c^2)	$\sqrt{<k_t^2>}$ (GeV/c)	b	χ^2/dof	b'	χ^2/dof	α	β	χ^2/dof
DO2/CTEQ2L	1.35	0.00	1.10	560	2.61	11	1.36	4.78	4.3
DO2/CTEQ2L	**1.35**	**0.44**	1.06	410	2.58	12	1.55	5.07	2.8
DO2/CTEQ2L	1.35	1.00	0.90	230	2.39	25	2.20	5.72	2.5
DO2/CTEQ2L	1.50	0.00	1.00	410	2.46	11	1.54	4.82	3.1
DO2/CTEQ2L	1.50	0.44	0.98	320	2.46	14	1.74	5.15	2.1
DO2/CTEQ2L	1.50	1.00	0.84	170	2.30	28	2.42	5.81	1.7
DO2/CTEQ2L	1.65	0.00	0.94	340	2.37	13	1.74	4.96	2.5
DO2/CTEQ2L	1.50	0.44	0.91	280	2.35	17	1.90	5.17	2.5
DO2/CTEQ2L	1.65	1.00	0.80	140	2.22	31	2.60	5.85	1.4
GRV/CTEQ4L	1.35	0.00	1.29	630	2.87	12	1.13	4.74	3.7
GRV/CTEQ4L	1.35	0.44	1.22	480	2.83	12	1.33	5.10	4.1
GRV/CTEQ4L	1.35	1.00	1.01	260	2.58	17	1.92	5.71	2.4
GRV/CTEQ4L	1.50	0.00	1.16	520	2.69	10	1.30	4.79	2.7
GRV/CTEQ4L	1.50	0.44	1.11	430	2.65	11	1.44	4.99	2.6
GRV/CTEQ4L	1.50	1.00	0.94	240	2.45	19	2.05	5.62	2.2
GRV/CTEQ4L	1.65	0.00	1.07	460	2.55	10	1.42	4.77	2.5
GRV/CTEQ4L	1.65	0.44	1.02	370	2.52	12	1.60	5.02	2.1
GRV/CTEQ4L	1.65	1.00	0.88	220	2.34	23	2.13	5.50	2.1
GRV/CTEQ4L	1.35	0.00	1.05	240	2.67	17	1.86	5.78	4.8
GRV/CTEQ4L	1.35	0.44	1.00	210	2.61	22	2.12	6.14	4.3
GRV/CTEQ4L	1.35	1.00	0.86	110	2.41	39	2.84	6.76	3.7
GRV/CTEQ4L	1.50	0.00	0.97	210	2.52	18	2.02	5.72	3.0
GRV/CTEQ4L	1.50	0.44	0.93	160	2.48	26	2.25	6.01	3.9
GRV/CTEQ4L	1.50	1.00	0.81	91	2.30	41	2.98	6.63	2.2
GRV/CTEQ4L	1.65	0.00	0.90	180	2.39	20	2.14	5.61	2.3
GRV/CTEQ4L	1.65	0.44	0.87	150	2.35	25	2.35	5.85	2.0
GRV/CTEQ4L	1.65	1.00	0.76	95	2.19	45	3.06	6.41	1.5

Table 6.17: Shape parameters from fits to various PYTHIA/JETSET D^0 p_T^2 distributions. Above the line are results obtained using the default fragmentation. The results below the line increase the average p_T of popped quarks from 0.36 to 0.60 GeV/c using PYTHIA parameter PARJ(21). The parameters b, b', and α & β come from fitting the p_T^2 distribution with Eqs. 6.20, 6.21, and 6.22, in the ranges 0 (GeV/c)^2<p_T^2<4 (GeV/c)^2, 1 (GeV/c)^2<p_T^2<18 (GeV/c)^2, and 0 (GeV/c)^2<p_T^2<18 (GeV/c)^2, respectively. The default theory parameters are shown in bold.

and/or charm quark mass to bring the b' value close to the data and even so, the α and β parameters are even worse. Many of the parameter sets used to obtain the PYTHIA/JETSET D^0 predictions give good agreement with the data for both b' and α and β. It is clear that there are several combinations of charm quark mass and intrinsic k_t which agree with the data. Also, the second hadronization scheme which increases the p_T of the quarks popped during string fragmentation can also take the place of adding k_t or increasing the charm quark mass.

Although the fitting functions do not provide a very good fit to the data, they are sometimes the only way to compare one's results with previous experiments. A comparison of n and b parameters obtained from E791 to other charm production experiments from π-N interactions is shown in Table 6.18. Extrapolating to other experiments is not trivial, however, since the other experiments include D^+ mesons as well. Also, the x_F range and p_T^2 range fitted by each experiment is different. Beam energy dependencies also cloud the result; NLO predicts an increase of $\sim$10% in n from 250 to 500 GeV and a decrease of $\sim$15% in b over the same range. In addition to the parameters listed in Table 6.18, E769 [38] also reported values for b' and α & β from Eq. 6.21 and 6.22, respectively. Those values were: $b' = 2.74 \pm 0.09$ (GeV/c)$^{-1}$, $\alpha = 1.4 \pm 0.3$ (GeV/c^2)$^{-2}$, and $\beta = 5.0 \pm 0.6$ compared to the results presented here which are: $b' = 2.41 \pm 0.03$ (GeV/c)$^{-1}$, $\alpha = 2.92 \pm 0.55$ (GeV/c^2)$^{-2}$, and $\beta = 6.68 \pm 0.77$.

A direct comparison to the results from the recent WA92 experiment is shown in Figures 6.16 and 6.17 for the x_F and p_T^2 distributions, respectively. The WA92 data comes from 350 GeV π^--N interactions beam and was obtained from Ref. [41] and [46]. The WA92 data was normalized to the E791 data by minimizing the χ^2/dof. Although the results are similar, the WA92 data shows a steeper x_F distribution and

Experiment	Energy (GeV)	x_F Range	n	p_T^2 Range $(\mathrm{GeV/c})^2$	b $(\mathrm{GeV/c})^{-2}$
E791	500	0.05–0.5	4.61±0.19	0–4	0.83±0.02
E653[39]	600	0.0–0.8	4.25±0.24±0.23	0–9	0.76±0.03±0.03
NA27[40]	360	0.0–0.9	3.8±0.6	0–4.5	$1.18^{+0.18}_{-0.16}$
WA92[41]	350	0.0–0.8	4.27±0.11	0–7	0.89±0.02
WA75[42]	350	-0.5–0.5	3.5±0.5	0–10	0.77±0.04
E769[43]	250	0.0–0.8	4.03±0.18	0–4	1.08±0.05
NA32[44]	230	0.0–0.8	3.74±0.23±0.37	0–10	0.83±0.03±0.02
NA32[45]	200	0.0–0.8	$2.5^{+0.4}_{-0.3}$	0–5	$1.06^{+0.12}_{-0.11}$

Table 6.18: Comparison of x_F and p_T^2 shape parameters to previous pion-beam charm production experiments. The E791 results are for D^0 mesons only, the E769 result comes from a combined sample of D^0, D^+, and D_s mesons while the rest of the results are obtained by combining D^0 and D^+ mesons.

some discrepancies in the p_T^2 data.

6.3.3 D^0 Total Cross Section

Throughout this section, the *total cross section* is used as shorthand for the total cross section for $D^0/\overline{D}^0$ with $x_F>0$. Although the total cross section is conceptually the simplest measurement, it is in fact the most difficult. The number of acceptance corrected events is one prerequisite for obtaining the total cross section. One way to obtain the number of acceptance corrected events is to measure one acceptance for all events with $x_F>0$ and determine the yield from one fit to all data events with $x_F>0$. This poses two problems. First, since we will be integrating over all x_F, some signal (in the Monte Carlo and data) will be lost due to the varying widths. Secondly, we will have errors due to the residual differences between the Monte Carlo and data x_F distributions. Since the acceptance depends strongly on x_F, correctly integrating over x_F requires very good agreement between Monte Carlo and data x_F distributions even at x_F beyond where we have signal. Therefore, we take a slightly different approach

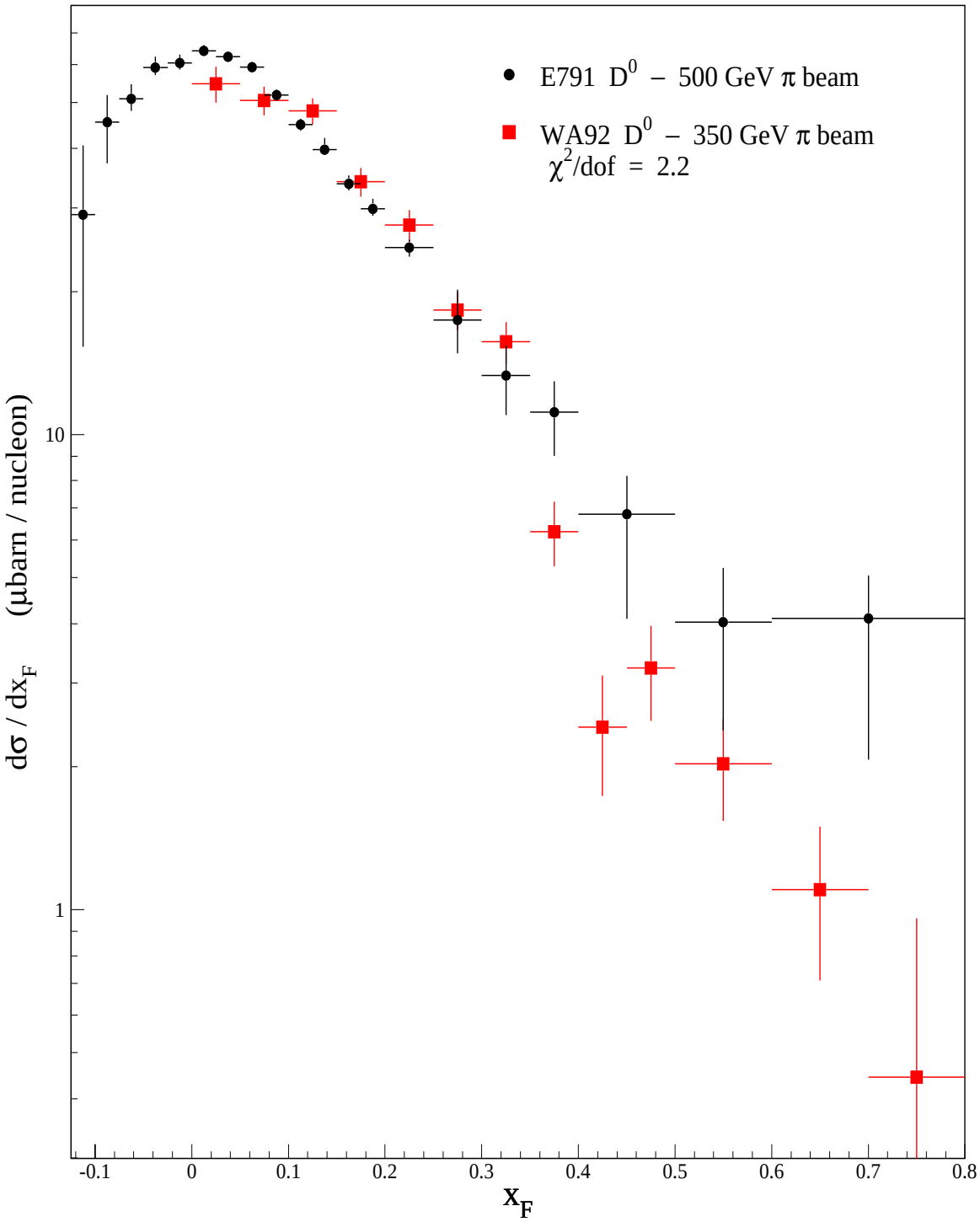

Fig. 6.16.— D^0 fully corrected x_F differential cross sections from E791 and WA92. The WA92 data is obtained from Ref. [41] and normalized to the E791 data. The E791 error bars include all errors except a $^{+10.2}_{-10.9}\%$ normalization error.

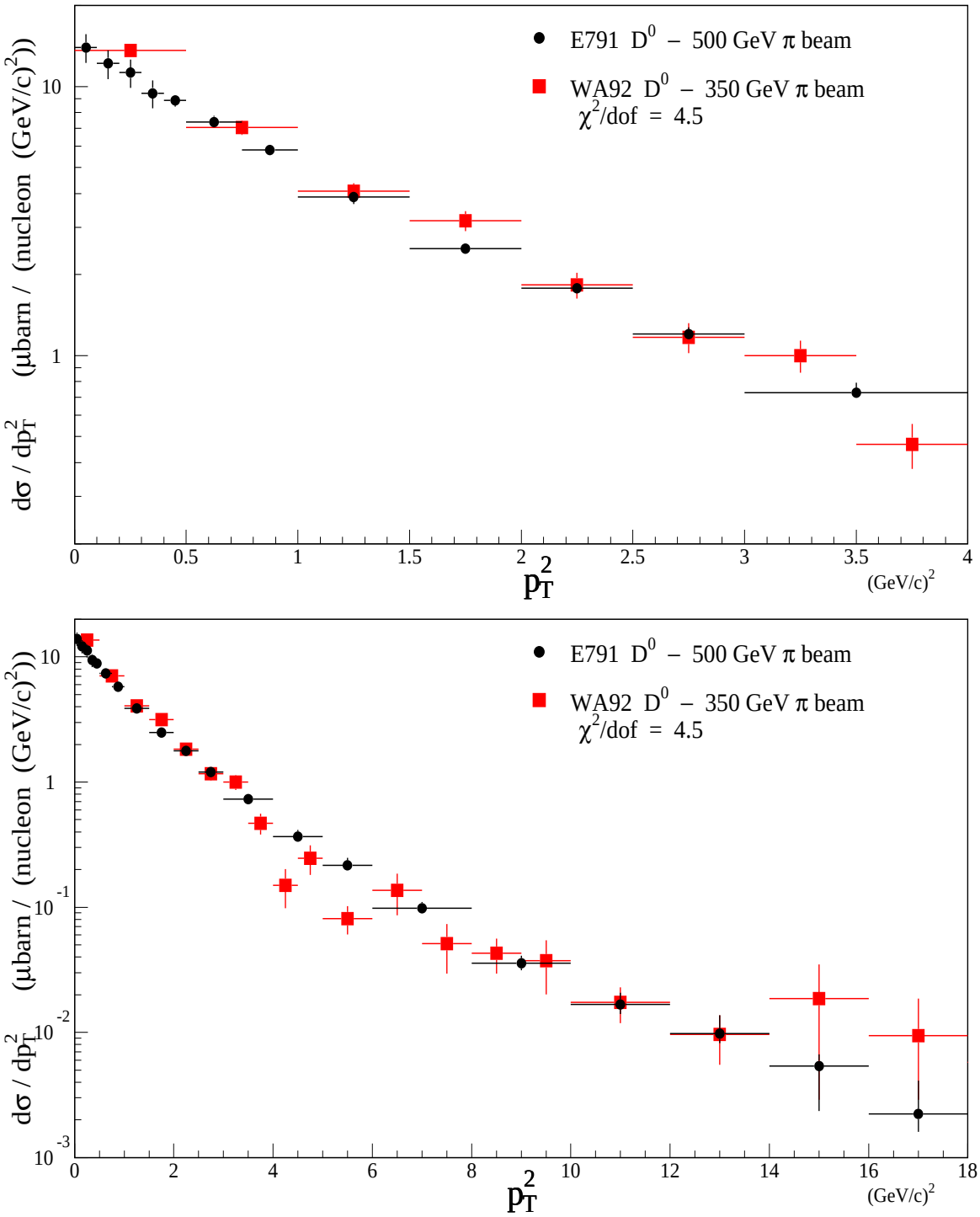

Fig. 6.17.— D^0 fully corrected p_T^2 differential cross sections from E791 and WA92. The WA92 data is obtained from Ref. [41] and normalized to the E791 data. The E791 error bars include all errors except a $^{+10.5}_{-14.8}\%$ normalization error.

in determining the cross section. We obtain the total cross section by summing up the contributions from the x_F bins between 0.0 and 0.8. Since we have no information about x_F>0.8, we assume the bin from 0.8 to 1.0 contains half the signal with the same error as the bin from 0.6 to 0.8. Determining systematic errors and combining the $K\pi$ and $K\pi\pi\pi$ data sets is similar but not exactly the same to what was done for the differential distributions, described in Section 6.3.1. First, the $K\pi$ and $K\pi\pi\pi$ total cross sections are calculated for the base distributions. Then, the total cross sections are calculated for all of the variations to the base distributions to determine the systematic errors for each of the $K\pi$ and $K\pi\pi\pi$ cross sections measurements. Weighting the $K\pi$ and $K\pi\pi\pi$ cross section measurements by the inverse of the sum of the squares of the statistical and systematic errors (including the error on the branching ratio from the PDG[31]), the D^0 total cross section is obtained. This gives us the central value for the total cross section (15.4 μb/nucleon) and the combination of statistical (1%) and uncorrelated systematic errors. The correlated systematic error on the D^0 total cross section is obtained by combining the $K\pi$ and $K\pi\pi\pi$ cross sections for each of the correlated errors and using the maximum deviation as the error. This gives a range of 13.5–16.7 μb/nucleon. The normalization error of $\pm 6.45\%$ from Eq. 6.10 is also added in quadrature with all of the above errors. Finally, we can only determine our tracking and vertexing efficiency as well as the ratio of $K\pi\pi\pi$ to $K\pi$ branching ratio is measured. This introduces an error of $\pm 0.09/1.96 = \pm 4.6\%$ which is added in quadrature. All of the errors entering into the total cross section calculation are summarized and summed in Table 6.19. Using these values, our measurement of the $D^0/\overline{D}^0$ x_F>0 total cross section is $\sigma(D^0/\overline{D}^0\,; x_F > 0) = 15.4\,^{+1.8}_{-2.3}$ μbarns/nucleon.

We can obtain x_F>0 cross sections from the MNR NLO results in a similar fashion, that is, by simply adding up the positive bins in the x_F histogram. The cross

Error type	Relative Error (%)		
	$K\pi$	$K\pi\pi\pi$	D^0
$K\pi$ & $K\pi\pi\pi$ statistical & independent systematic errors	$^{+4.1}_{-8.7}$	$^{+5.0}_{-9.6}$	$^{+4.2}_{-7.1}$
Statistics	±1.0	±2.8	
SDZ cut efficiency modeling	$^{+0.1}_{-0.0}$	$^{+1.2}_{-0.0}$	
MC background function	$^{+0.0}_{-5.5}$	$^{+0.0}_{-6.0}$	
D^0 signal width in fits	$^{+4.0}_{-4.1}$	$^{+3.9}_{-4.4}$	
Correlated systematic errors			$^{+7.0}_{-10.2}$
Lifetime weighting	$^{+0.6}_{-0.5}$		
MC weighting	$^{+0.0}_{-2.3}$		
MC production model (MC1 vs MC2)	$^{+5.9}_{-5.1}$		
Run weighting	$^{+1.0}_{-2.0}$		
Tracking and vertexing (from $K\pi\pi\pi$ / $K\pi$ branching ratio)			±4.6
Trigger efficiency			±6.4
Target material (T_N measurement)			±0.3
Total			$^{+11.4}_{-14.7}$

Table 6.19: Sources and values of the errors associated with the total forward D^0 cross section measurement.

section obtained from the MNR NLO program is a $c\overline{c}$ cross section. To obtain the single inclusive cross section we multiply by 2 to account for the fact that we are counting both D^0 and $\overline{D}^0$. We also need to account for the charm states which we did not reconstruct. This includes the $D^{\pm}$, D_s, and Λ_c. All of these together amount to approximately 110% of the D^0 production. Combining these two numbers gives a total factor of 0.95. The statistical errors on the theory predictions are negligible. Also, the effect of hadronization and intrinsic k_t is very small, 2% and 0.5%, respectively. The important sources of systematic error for the theoretical predictions are variations in the parton distribution functions, the factorization scale, the renormalization scale and the charm quark mass. As noted earlier, all of these parameters are quite correlated. The results for various parameter sets are shown in Table 6.20. Clearly, given the

large errors, we are in agreement with the theoretical predictions of MNR NLO. Also, the data favor a low charm quark mass and/or low renormalization scale. Combining all the variations shown in Table 6.20 results in a total cross section range of 1.9–16.0 μbarns/nucleon.

PDF (π/N)	m_c (GeV/c^2)	μ_R	μ_F	$\sigma(D^0/\overline{D}^0\,;x_F>0)$ (μbarns/nucleon)	Difference
SMRS2/HMRSB	1.35	μ	2μ	8.4	+64%
SMRS2/HMRSB	**1.50**	$\boldsymbol{\mu}$	$\boldsymbol{2\mu}$	5.1	—
SMRS2/HMRSB	1.65	μ	2μ	3.2	-37%
SMRS2/HMRSB	1.50	$\frac{1}{2}\mu$	2μ	9.3	+83%
SMRS2/HMRSB	1.50	2μ	2μ	3.3	-35%
SMRS2/HMRSB	1.65	μ	μ	5.2	+2%
SMRS2/CTEQ4M	1.50	μ	2μ	4.6	-11%
SMRS1/HMRSB	1.50	μ	2μ	5.5	+7%
SMRS3/HMRSB	1.50	μ	2μ	4.7	-8%

Table 6.20: Results for the MNR NLO $D^0/\overline{D}^0$ total forward cross section. Results are shown for several parameter sets including the default set in bold.

We can also try to compare this result with other experiments and with the next-to-leading order predictions as a function of energy. To be consistent with previous comparisons, we plot the total charm cross section, $\sigma(c\overline{c})$. This is obtained directly from the MNR NLO prediction. In order to make accurate comparisons with previous data, we take all measured $D^0/\overline{D}^0$ x_F>0 cross sections and multiply them by 1.7. This factor of 1.7 accounts for the relative production of D^0 mesons compared to charm quarks (2.1), the conversion from x_F>0 to all x_F (1.6) and the conversion from single charm cross section to double charm cross section (0.5). The experimental and theoretical results are shown in Fig. 6.18.

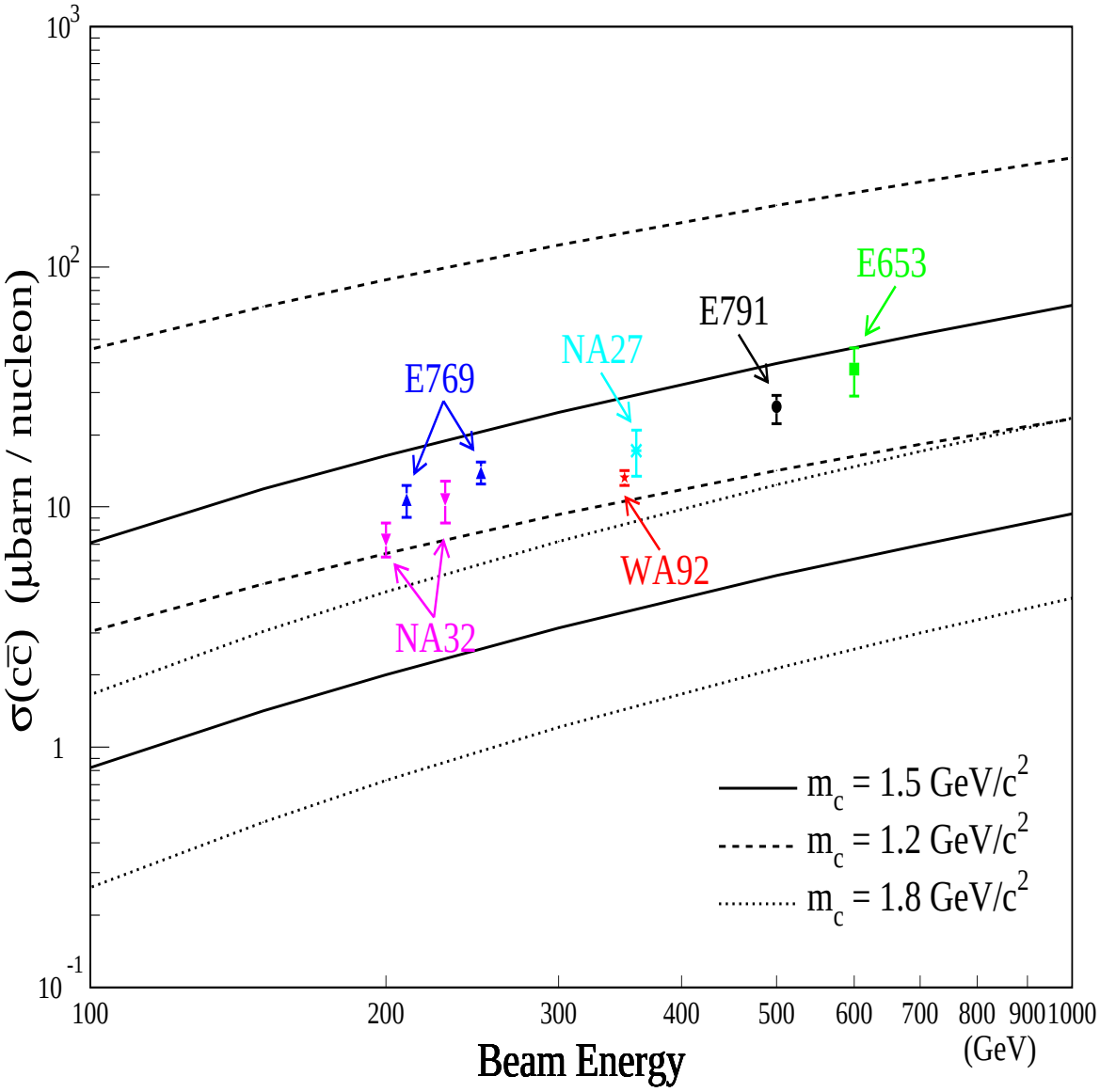

Fig. 6.18.— Theoretical and experimental results for the $c\overline{c}$ cross section versus energy. The theoretical curves are obtained from MNR NLO predictions [47]. The three bands (solid, dashed, and dotted) correspond to three different charm quark masses (1.5 GeV/c^2, 1.2 GeV/c^2, and 1.8 GeV/c^2). The variation within the bands comes from varying μ_R from 0.5μ to 2.0μ. The parameter μ_F is fixed at 2μ. The experimental data points are all obtained from the single inclusive $D^0/\overline{D}^0$ $x_F>0$ cross section multiplied by 1.7. The E653, NA27, WA92, NA32-200 GeV, NA32-230 GeV, and E769 data were obtained from references [39], [40], [41], [45], [44], and [43], respectively. The 200 GeV NA32 results were increased by 30% to account for newer branching ratios and an error in the analysis as suggested in Ref. [44].

Chapter 7

Conclusions

In this thesis we have presented the total forward cross section and differential cross sections versus x_F and p_T^2 for D^0 mesons from Fermilab experiment E791 data. This analysis represents the first measurement of the D^0 cross section for a 500 GeV pion beam. The high statistics allow one to clearly see a turnover point greater than zero in the x_F distribution (Fig. 6.14), as expected from the parton distribution functions. The high statistics also point out the many shortcomings of the functions commonly used to fit the x_F and p_T^2 distributions.

We have compared our differential cross section results to predictions from the next-to-leading order calculation by Mangano, Nason, and Ridolfi [4] and to the Monte Carlo event generator PYTHIA/JETSET by Sjöstrand [7]. We have found that the many adjustable parameters in the theories allow one to obtain distributions which provide a good match for our data. Unfortunately with these data alone, a unique set of parameters is not possible. In conjunction with data from other experiments with different beam energies and types and with data from different measurements such as asymmetries and charm-pair results, it may be possible to pin down a unique set of parameters. We have also found that the hadronization scheme implemented in

PYTHIA/JETSET can be adjusted to fit the data but that the c quark predictions from the MNR NLO theory give equally good results.

Although the fitting functions do not provide a very good fit to the data, we provide results in order to compare with previous experiments. This comparison to other charm production experiments from π-N interactions was shown in Table 6.18. In addition, direct comparisons were made to a recent high-statistics charm production experiment, WA92, in Figures 6.16 and 6.17.

The total x_F>0 $D^0/\overline{D}^0$cross section measured by E791 is $\sigma(D^0/\overline{D}^0\ ; x_F > 0) = 15.4\ ^{+1.8}_{-2.3}\ \mu$barns/nucleon. This is consistent with the MNR NLO predictions and favors a low renormalization scale or low charm quark mass as do most of the recent charm cross section measurements from π^--N production as was shown in Fig. 6.18.

Bibliography

[1] P.N. Harriman, A.D. Martin, R.G. Roberts, and W.J. Stirling. Parton Distributions Extracted from Data On Deep Inelastic Lepton Scattering, Prompt Photon Production and the Drell-Yan Process. *Physical Review D*, 42:798, 1990.

[2] P.J. Sutton, A.D. Martin, R.G. Roberts, and W.J. Stirling. Parton distributions for the pion extracted from Drell-Yan and prompt photon experiments. *Physical Review D*, 45:2349, 1992.

[3] H. Plothow-Besch. *PDFLIB: Nucleon, Pion and Photon Parton Density Functions and α_s Calculations - User's Manual,* Version 7.09. CERN, 1997. CERN Program Library W5051.

[4] M.L. Mangano, P. Nason, and G. Ridolfi. Heavy-quark correlations in hadron collisions at next-to-leading order. *Nuclear Physics B*, 373:295, 1992.

[5] C. Peterson, D. Schlatter, I. Schmitt, and P.M. Zerwas. Scaling violations in inclusive e^+e^- annihilation spectra. *Physical Review D*, 27:105, 1983.

[6] E791 Collaboration, E.M. Aitala, et al. Asymmetries between the production of D^+ and D^- mesons from 500 GeV/c π^- nucleus interactions as a function of x_F and p_t^2. *Physics Letters*, B371:157, 1996.

[7] H.-U. Bengtsson and T. Sjöstrand. High-energy-physics event generation with PYTHIA 5.7 and JETSET 7.4. *Computer Physics Communications*, 82:74, 1994.

[8] M.L. Mangano, P. Nason, and G. Ridolfi. Fixed-target hadroproduction of heavy quarks. *Nuclear Physics B*, 405:507, 1993.

[9] E516 Collaboration, K. Sliwa, et al. Study of D^* production in high-energy γp interactions. *Physical Review D*, 32:1053, 1985.

[10] E691 Collaboration, J.R. Raab, et al. Measurement of the D^0, D^+, and D_s^+ lifetimes. *Physical Review D*, 37:2391, 1988.

[11] E769 Collaboration, G.A. Alves, et al. Feynman-x and Transverse Momentum Dependence of $D^{\pm}$ and $D^0/\overline{D}^0$ Production in 250 GeV π^--Nucleon Interactions. *Physical Review Letters*, 69:3147, 1992.

[12] H. Fenker. A Standard Beam PWC for Fermilab. Technical Report TM-1179, Fermilab, 1983.

[13] E769 Collaboration, G.A. Alves, et al. Atomic Mass Dependence of $D^{\pm}$ and $D^0\bar{D}^0$ Production in 250 GeV $\pi^{\pm}$ Nucleon Interactions. *Physical Review Letters*, 70:1, 1993.

[14] Carroll et al. Absorption cross sections of $\pi^{\pm}$, $K^{\pm}$, p and $\overline{p}$ on nuclei between 60 and 280 GeV/c. *Physics Letters*, B80:319, 1979.

[15] P.E. Karchin et al. Test Beam Studies of a Silicon Microstrip Vertex Detector. *IEEE Transactions on Nuclear Science*, NS-32:612, 1985.

[16] B.R. Kumar for the Tagged Photon Spectrometer Collaboration. Charm Photoproduction Using a Silicon Vertex Detector. In F. Villa, editor, *Vertex Detectors*, volume 34 of *Ettore Majorana international science series, physical sciences*, page 167. Plenum Press, 1988. Proceedings of a workshop for the INFN Eloisatron Project, held September 21-26, 1986, in Erice, Sicily, Italy.

[17] D. Bartlett et al. Performance of the Cherenkov Counters in the Fermilab Tagged Photon Spectrometer Facility. *Nuclear Instruments and Methods*, A260:55, 1987.

[18] V.K. Bharadwaj et al. A Large Area Liquid Scintillation Multiphoton Detector. *Nuclear Instruments and Methods*, 228:283, 1985.

[19] D.J. Summers. Reconstruction of a Strip Geometry Calorimeter Using Stepwise Regression. *Nuclear Instruments and Methods*, 228:290, 1985.

[20] J.A. Appel, P.M. Mantsch, M.M. Streetman, and R.M. Robertson. Hadron Calorimetry at the Fermilab Tagged Photon Spectrometer Facility. *Nuclear Instruments and Methods*, A243:361, 1986.

[21] E791 Collaboration, E.M. Aitala, et al. Search for the Flavor-Changing Neutral Current Decays $D^+ \to \pi^+\mu^+\mu^-$ and $D^+ \to \pi^+e^+e^-$. *Physical Review Letters*, 76:364, 1996.

[22] E791 Collaboration, E.M. Aitala, et al. Search for D^0–$\overline{D}^0$ Mixing in Semileptonic Decays. *Physical Review Letters*, 77:2384, 1996.

[23] E791 Collaboration, E.M. Aitala, et al. Measurement of the Branching Ratio $B(D^+ \to \rho^0\ell^+\nu_\ell)\ /B(D^+ \to \overline{K}^{*0}\ell^+\nu_\ell)$. *Physics Letters*, B397:325, 1997.

[24] S. Amato et al. The E791 Parallel Architecture Data Acquisition System. *Nuclear Instruments and Methods*, A324:535, 1992.

[25] S. Bracker, K. Gounder, K. Hendrix, and D. Summers. A Simple Multiprocessor Management System for Event-Parallel Computing. *IEEE Transactions on Nuclear Science*, NS-43:2457, 1996.

[26] C. Stoughton and D.J. Summers. Using Multiple RISC CPUs in Parallel to Study Charm Quarks. *Computers in Physics*, 6:371, 1992.

[27] F. Rinaldo and S. Wolbers. Loosely Coupled Parallel Processing at Fermilab. *Computers in Physics*, 7:184, 1993.

[28] I. Gaines et al. The ACP Multiprocessor System at Fermilab. In *Proceedings of the International Conference on Computing in High Energy Physics, Asilomar, February 2-6, 1987*, volume 45 of *Computer Physics Communications*, page 323, 1987.

[29] J. Biel et al. Software for the ACP Mulitprocessor System. In *Proceedings of the International Conference on Computing in High Energy Physics, Asilomar, February 2-6, 1987*, volume 45 of *Computer Physics Communications*, page 331, 1987.

[30] F. James and CN/ASD Group. MINUIT - *Function Minimization and Error Analysis – Reference Manual,* Version 94.1. CERN, 1994. CERN Program Library D506.

[31] Particle Data Group, Caso, et al. Review of Particle Physics. *The European Physical Journal C*, 3, 1998.

[32] H. Goldstein. *Classical Mechanics.* Addison-Wesley, 2nd edition, 1980.

[33] E687 Collaboration, Frabetti, et al. Precise Measurements of the D^0 and D^+ Meson Lifetimes. *Physics Letters*, B323:459, 1994.

[34] S. Kwan. E791 offline_doc_397.ps, October 1998.

[35] D.W. Duke and J.F. Owens. Q^2-dependent parametrizations of parton distribution functions. *Physical Review D*, 30:49, 1984.

[36] M. Glück, E. Reya, and A. Vogt. Pionic parton distributions. *Zeitschrift für Physik C*, 53:651, 1992.

[37] CTEQ Collaboration, H.L. Lai, et al. Improved Parton Distributions from Global Analysis of Recent Deep Inelastic Scattering and Inclusive Jet Data. *Physical Review D*, 55:1280, 1997.

[38] E769 Collaboration, G.A. Alves, et al. Feynman-x and Transverse Momentum Dependence of D Meson Production in 250 GeV π, K, and p Interactions with Nuclei. *Physical Review Letters*, 77:2392, 1996.

[39] E653 Collaboration, K. Kodama, et al. Charm Meson Production in 600 GeV/c π^- Emulsion Interactions. *Physics Letters*, B284:461, 1992.

[40] LEBC-EHS (NA27) Collaboration, M. Aguilar-Benitez, et al. Inclusive Properties of D-Mesons Produced in 360 GeV π^-p Interactions. *Physics Letters*, B161:400, 1985.

[41] Beatrice (WA92) Collaboration, M. Adamovich, et al. Measurements of Charmed-Meson Production in Interactions Between 350 GeV/c π^- Particles with Nuclei. *Nuclear Physics B*, 495:3, 1997.

[42] WA75 Collaboration, S. Aoki, et al. Hadroproduction of $D\overline{D}$ Pairs in the Interaction of 350 GeV/c π^- Mesons with Nuclei. *Progress in Theoretical Physics*, 87:1315, 1992.

[43] E769 Collaboration, G.A. Alves, et al. Forward Cross Sections for Production of D^+, D^0, D_s, D^{*+}, and Λ_c in 250 GeV $\pi^\pm$, $K^\pm$, and p Interactions with Nuclei. *Physical Review Letters*, 77:2388, 1996.

[44] ACCMOR (NA32) Collaboration, S. Barlag, et al. Production of D, D^* and D_s mesons in 200 GeV/c π^-, K^- and p-Si interactions. *Zeitschrift für Physik C*, 39:451, 1988.

[45] ACCMOR (NA32) Collaboration, S. Barlag, et al. Production properties of D^0, D^+, D^{*+} and D_s^+ in 230 GeV/c π^- and K^- –Cu interactions. *Zeitschrift für Physik C*, 39:451, 1988.

[46] Durham Database Group. HEPDATA: REACTION DATA Database. http://durpdg.dur.ac.uk/scripts/hepreac/3489906.

[47] S. Frixione, M.L. Mangano, P. Nason, and G. Ridolfi. Heavy-Quark Production. In A.J. Buras and M. Lindner, editors, *Heavy Flavours II*, Advanced Series on Directions in High Energy Physics, Singapore, 1997. World Scientific Publishing Co. hep-ph/9702287.